8-22-2024 2:00 PM

Functional Near-Infrared Spectroscopy as a Bedside Neuroimaging Tool for Neonatal Brain Monitoring and Injury Characterization

Lingkai Tang, *Western University*

Supervisor: Duerden, Emma G., *The University of Western Ontario*
Co-Supervisor: St. Lawrence, Keith, *The University of Western Ontario*
A thesis submitted in partial fulfillment of the requirements for the Doctor of Philosophy degree in Biomedical Engineering

Abstract

Early brain injury in neonates is a common neurological complication associated with high mortality rates and long-term morbidities. Two common types of injury are intraventricular hemorrhage (IVH) and hypoxic ischemic encephalopathy (HIE). Currently used clinical neuroimaging tools for diagnosing or monitoring the injury have limitations, e.g., cranial ultrasound is not for continuous monitoring of the evolution of injury so it could miss the optimal timing for intervention, and magnetic resonance imaging (MRI) is not very accessible for infants in neonatal intensive care unit. Functional near-infrared spectroscopy (fNIRS) can be an alternative imaging technique as it can be used at the bedside for continuous monitoring. Previous research using functional MRI (fMRI) indicated that neonates with brain injury were reported to have altered resting-state functional connectivity (RSFC), which can be a potential biomarker for diagnosis. The current thesis examined and expanded upon the potential of fNIRS as a neuromonitoring tool for newborns with brain injury. Specifically, the goal was to determine if fNIRS can yield RSFC indices comparable to fMRI and whether differences in RSFC can be detected between neonates with and without brain injury. Also, predictive models based on machine learning were developed to address the cortical penetration depth of fNIRS, which is a major drawback limiting wider applications of the technology.

Neonates diagnosed with IVH or HIE, and healthy newborns were recruited and scanned with fNIRS and fMRI. RSFC was calculated from both modalities and compared. Then RSFC patterns were compared between neonates with and without injury. fNIRS and fMRI yielded comparable RSFC indices, and fNIRS also identified altered RSFC patterns in both IVH and HIE groups compared to healthy newborns. Then, graph convolutional networks (a subtype of artificial neural networks) were applied to predict subcortical connectivity from cortical connectivity, using either neonatal or adult fNIRS data, and gave good performance. In general, this thesis indicates that fNIRS has the potential to be a new tool for assessing brain injury and monitoring cerebral hemodynamics in neonates.

Keywords: Neonatal brain injury, Intraventricular hemorrhage, Hypoxic ischemic encephalopathy, Functional near-infrared spectroscopy, Functional magnetic resonance imaging, Functional connectivity, Machine learning.

Summary for Lay Audience

Early brain injury occurs in both term and preterm born babies and seriously affects their health. Current tools for diagnosing and monitoring brain injury are limited. Namely ultrasound needs to be done at specific times after the injury and can delay treatments. Further, magnetic resonance imaging (MRI) cannot always be accessible for babies who are critically ill as time away from the intensive care unit can pose risks. Functional near-infrared spectroscopy (fNIRS) is a promising new tool that can monitor the impact of injury on blood flow to the brain as well as how brain regions are functionally connected, meaning how different brain regions communicate with one another. This thesis tested whether fNIRS can give us meaningful functional connectivity information and demonstrate differences between babies with and without brain injury. Also, fNIRS has a major limitation in that one cannot record from regions deep within the brain, which can be impacted by injury. To address this gap, computational methods were developed to infer brain connectivity in deep regions of the brain based on the connectivity in the outer regions of the brain (cortex).

Newborns with early brain injury and healthy babies were recruited and scanned with fNIRS. Functional connectivity was calculated and compared between babies with and without injury. fNIRS identified altered brain connectivity patterns in the injury groups compared to healthy babies. Then, a computational method based on machine learning was applied to predict activity in the deep regions of the brain, and tested on newborn and adult fNIRS data, and showed good performance.

In general, this study shows that fNIRS has the potential as a new tool for monitoring brain injury in newborns born critically ill.

Co-Authorship Statement

All chapters except for chapters 1 and 5 are adapted from previously published (or submitted) manuscripts. As the first author on all manuscripts listed below, I contributed to all aspects of the work including study design, data collection, data analysis, and manuscript drafting and submission. As the supervisor and principal investigator, Dr. Emma G. Duerden supervised each study from conception to completion, while providing mentorship and guidance. She also offered help on data collection, comments and advice on data analysis, reviewing and editing manuscripts, and approval for publication. As co-supervisor, Dr. Keith St. Lawrence also provided feedback on the data analysis and editing manuscripts. For the rest of this section, each manuscript included a list of co-authors who significantly contributed to the work. All co-authors approved the final version of the manuscript for publication, and their individual contributions are listed below.

Chapter 2 is adapted from the publication titled "Altered functional connectivity in preterm neonates with intraventricular hemorrhage using functional near-infrared spectroscopy" submitted to Heliyon in 2024 by Lilian M. N. Kebaya, Lingkai Tang (co-first author), Talal Altamimi, Alexandra Kowalczyk, Melab Musabi, Sriya Roychaudhuri, Homa Vahidi, Paige Meyerink, Sandrine de Ribaupierre, Soume Bhattacharya, Leandro Tristao Abi Ramia de Moraes, Keith St. Lawrence, and Emma G. Duerden and is currently under review. Lilian M. N. Kebaya, Talal Altamimi, Alexandra Kowalczyk, Melab Musabi, Sriya Roychaudhuri, Homa Vahidi, Paige Meyerink, Sandrine de Ribaupierre, Soume Bhattacharya, Keith St. Lawrence, and Emma G. Duerden were involved in the study design, data acquisition design and execution of data analytic strategy, revision of the final version of this manuscript. Emma G. Duerden analyzed the data. Leandro Tristao Abi Ramia de Moraes characterized brain injuries on MRI images. Lilian M. N. Kebaya and Emma G. Duerden wrote the initial draft of the manuscript and contributed to the execution of the data analytic strategy.

Chapter 3 is adapted from the publication titled "Altered resting state functional connectivity in newborns with hypoxic ischemic encephalopathy assessed using high-density functional near-infrared spectroscopy" published in Scientific Reports in 2024 by Lingkai Tang, Lilian M. N. Kebaya, Talal Altamimi, Alexandra Kowalczyk, Melab Musabi, Sriya Roychaudhuri, Homa Vahidi, Paige Meyerink, Sandrine de Ribaupierre, Soume Bhattacharya, Leandro

Tristao Abi Ramia de Moraes, Keith St. Lawrence, and Emma G. Duerden. Lilian M. N. Kebaya, Talal Altamimi, Alexandra Kowalczyk, Melab Musabi, Sriya Roychaudhuri, Homa Vahidi, Paige Meyerink, Sandrine de Ribaupierre, Soume Bhattacharya, Keith St. Lawrence, and Emma G. Duerden were involved in the study design, data acquisition, design and revision of the final version of this manuscript. Leandro Tristao Abi Ramia de Moraes characterized brain injuries on MRI images. Lilian M. N. Kebaya and Emma G. Duerden wrote the first draft of the manuscript.

Chapter 4 is adapted from the publication titled “Predicting cortical-thalamic functional connectivity using functional near-infrared spectroscopy and graph convolutional networks” submitted to Scientific Reports in 2024 by Lingkai Tang, Lilian M. N. Kebaya, Homa Vahidi, Paige Meyerink, Sandrine de Ribaupierre, Soume Bhattacharya, Keith St. Lawrence, and Emma G. Duerden and is currently under review. Lilian M. N. Kebaya, Homa Vahidi, Paige Meyerink, Sandrine de Ribaupierre, Soume Bhattacharya, Keith St. Lawrence, and Emma G. Duerden were involved in the study design, data acquisition and revision of the final version of this manuscript.

Dedication

I would like to dedicate this thesis first to my parents for their everlasting love and support, and for providing me the opportunity to pursue my education and potentially, an opportunity for a better life. Ever since I left home for college over 10 years ago, from undergraduate to PhD, from 1000 miles from you two to 10,000 miles, I feel I have been away from home for too long. But your encouragement and support always make me feel you are never far away and thank you for tolerating me for not being around for so long.

I would also like to dedicate this work to my girlfriend Ting. It is never easy to maintain a relationship of long distance, especially during the pandemic of COVID-19. Thank you for your trust and for allowing me to be away from you. Thank you for all the long Facetime calls and as much company as possible. Thank you for your continuous support, patience and always being there through the most difficult times during the whole process of PhD.

Finally, to all my friends and family, thank you so much for all your love and support. I dedicate this work to you all.

Acknowledgments

I will be forever grateful to my supervisor and mentor, Dr. Emma G. Duerden, for all her support and help during all these years. Your enthusiasm for research and unyielding diligence will be always a beacon for me in the rest of my life. You provided knowledge, resources and everything can be possibly expected for a smooth process of a PhD program. When I first started, I knew basically nothing about fNIRS and had only shallow knowledge on brain imaging in general. It was your guidance and dedication of countless hours that led me into this fascinating field and to achieve this much. None of my research projects would be feasible without your coordination and devotion. I will always remember the times we scanned all the participants together at St. Joseph's Hospital, and all the help from you carrying the chunky fNIRS machine back and forth, as well as setting up scanning protocols, recruiting and preparing all the participants. And no need to mention that you kept the NICU projects rolling during the most difficult time of the pandemics. I could not imagine the obstacles you encountered and your effort to overcome them. You are probably the most patient person I have ever known. I will always look up to you as a scientist and a human being.

To my co-supervisor, Dr. Keith St. Lawrence, thank you for always being there when I need guidance and advice. You read everything I wrote, long or short, good or bad, and gave the most constructive comments and feedback one could expect. And thank you for providing all necessary resources to make all projects possible. To my advisory committee members, Dr. Ali Khan and Dr. Yalda Mohsenzadeh, thank you both for being involved in the process of my PhD, and offering your wisdom, knowledge and experience at crucial time points and making sure I was on the right track.

I cannot be more thankful to our team from NICU and MBCU of LHSC, including Dr. Lilian M. N. Kebaya, Dr. Talal Altamimi, Dr. Alexandra Kowalczyk, Dr. Melab Musabi, Dr. Sriya Roychaudhuri, future Dr. Homa Vahidi, research nurses Paige Meyerink and Paula Camila Mayorga. You did all the hard work recruiting and scanning the babies in the hospital so that I could simply sit in front of a computer and analyze the data. You all are the true heroes and none of this study would be possible without you. A special thank to Lilian who co-authored all my publications and always gave her solid and pinpointing perspectives on clinical terms which I was potentially weak on. Also, thank you Dr. Sandrine de Ribaupierre and Dr. Soume

Bhattacharya for providing all necessary resources from the hospital side. I am sure there will be more collaborations in the future. I would also like to thank Dr. Leandro Tristao for characterizing the brain injuries of our neonatal participants. I would sincerely thank our pediatric neuroradiologist, the late Dr. Michael T. Jurkiewicz, for also characterizing the brain injuries, and still reviewing my manuscript when in palliative care. He was an exemplar of scientists whom I regret not getting acquainted with earlier in time.

I would like to thank all my neonatal participants and their families for letting their precious newborn babies wear some strange equipment, as well as the adult participants who came to the hospital during the pandemics voluntarily. Please be sure that your data were put into good use for a better understanding of certain medical complications and potential developments of new clinical applications of imaging technologies. Also, it is more than great to have all the members of the Developing Brain Lab. Thank you all for the numerous discussions at lab meetings and all the beer and laughter shared at the Grad Club.

Finally, I would like to thank the School of Biomedical Engineering for all the academic support, and Western Institute for Neuroscience for being an inclusive community. I will be always grateful to the funding agencies supporting my studies during past years: Natural Sciences and Engineering Council, the Canadian Institutes of Health Research, the Whaley and Harding Postdoctoral fellowship and the Children's Health Foundation.

Table of Contents

List of Tables

List of Figures

List of Abbreviations

ANN	Artificial neural network
AUC	Area under receiver operating characteristic curve
ALFF	Amplitude of low frequency fluctuation
ADHD	Attention deficit hyperactivity disorder
AFNI	Analysis of Functional NeuroImages
BOLD	Blood-oxygen-level-dependent
cUS	Cranial ultrasound
CV	Coefficient of variance
CI	Confidence interval
DFC	Dynamic functional connectivity
DWI	Diffusion-weighted imaging
DTI	Diffusion tensor imaging
DMN	Default mode network
EEG	Electroencephalograph
EPI	Echo planar imaging
fNIRS	Functional near-infrared spectroscopy
fMRI	Functional magnetic resonance imaging
FSL	FMRIB Software Library
FC	Functional connectivity

FP	False positive
FN	False negative
GA	Gestational age
GMH-IVH	Germinal matrix hemorrhage – intraventricular hemorrhage
GLM	General linear model
GCN	Graph convolutional network
HIE	Hypoxic ischemic encephalopathy
HbO	Oxygenated hemoglobin
Hb/HHb/Hbr	Deoxygenated hemoglobin
Hbt	Total hemoglobin
HI	Hypoxia-ischemia
IVH	Intraventricular hemorrhage
IQ	Intelligence quotient
ICA	Independent component analysis
IUGR	Intrauterine growth restriction
LHSC	London Health Science Centre
LOOV	Leave-one-out validation
MRI	Magnetic resonance imaging
MRS	Magnetic resonance spectroscopy
MBLL	Modified Beer-Lambert law

MBCU	Mother baby care unit
NICU	Neonatal intensive care unit
PHVD	Posthemorrhagic ventricular dilatation
PVHI	Periventricular hemorrhagic infarction
PVL	Periventricular leukomalacia
PCA	Principle component analysis
PCC	Pearson correlation coefficient
PMA	Postmenstrual age
RSFC	Resting-state functional connectivity
ROC	Receiver operating characteristic
ReLU	Rectified linear unit
SWI	Susceptibility-weighted imaging
STD/SD	Standard deviation
SDC	Short-distance channel
SVM	Support vector machine
SVR	Support vector regression
SGA	Small for gestational age
TH	Therapeutic hypothermia
TEA	Term equivalent age
T1w	T1-weighted

T2w	T2-weighted
TR	Repetition time
TE	Echo time
TCV	Total cerebral volume
TP	True positive
TN	True negative
WMI	White matter injury

Chapter 1

1 Introduction

This chapter provides a brief overview concerning neonatal brain injury and using functional near-infrared spectroscopy (fNIRS) as a clinical tool for monitoring and diagnosing early brain injury, which are key themes of the thesis. In this section, the rationale and objectives of this thesis will be presented and to demonstrate the potential utility of fNIRS to study the impact of neonatal brain injuries on functional connectivity. The goal of this dissertation is to develop novel methods to use fNIRS as a bedside brain monitoring technology to monitor brain injury in critically ill newborns. The use of fNIRS-based biomarkers may be key indicators of brain health in newborn populations. These biomarkers may be used in future trials to assess the efficacy of interventions and improve counselling for families.

1.1 Clinical rationale

Neonatal brain injury is a serious health issue associated with adverse outcomes. Yet currently available clinical neuroimaging technologies such as cranial ultrasound or magnetic resonance imaging (MRI) for assessing or diagnosing brain injuries are currently limited, and have several shortcomings. FNIRS has several advantages that make it very advantageous for use in clinical settings.

1.1.1 Neonatal brain injury

Neonatal brain injury is a main contributor to mortality and later development of neurodevelopmental disorders, or motor or cognitive impairments [1]. Brain injuries can occur in both term and preterm born neonates and have short and long term effects in surviving neonates, and can also have several negative consequences on families in terms of losses of productivity. The prevalence of the injury varies depending on the exact type of injury [2], [3], [4], [5], [6], [7] and the outcome can be modulated by many factors including severity and therapies. [8], [9], [10], [11], [12], [13], [14]. Neonatal brain injuries may be resulted from various etiologies, from reperfusion events after ischemia to defected

metabolic pathways expressed after birth [15], [16]. Injury patterns revealed by neuroimaging technologies also largely depend on the types of injuries, severity, the age of the infant when the injury occurs as well as developmental outcomes [17], [18], [19]. Since there are many types of neonatal brain injury and as just mentioned they show inconsistencies in many terms, in this study, two types of injury that are rather common to newborns were focused on. One is intraventricular hemorrhage (IVH) and the other one is hypoxic ischemic encephalopathy (HIE).

1.1.1.1 Intraventricular hemorrhage

IVH is a common type of neonatal brain injury that occurs in preterm born infants, born before 37 weeks' gestational age (GA). IVH, in simple words, is bleeding inside or around the ventricles [20]. In many cases, the term germinal matrix hemorrhage – IVH (GMH-IVH) is used, as the IVH injury mostly initiates from the periventricular germinal matrix, which is highly vascular and therefore is specifically vulnerable to hemorrhage [20]. Disturbances in cerebral blood flow is another factor contributing to the development of IVH. Such disturbances can be a result of respiratory distress syndrome, low Apgar scores, hypoxia, or seizures [20]. IVH injury initiates and is detectable within a few hours after birth [21]. The severity of IVH injury is commonly categorized into 4 grades based on how perfused the hemorrhage is within or even outside of the ventricle, where the mildest grade I means the bleeding is only within germinal matrix, while the severest grade IV indicates that the hemorrhage permeates mostly the ventricles and into brain parenchymal (intraparenchymal hemorrhage) [22]. IVH occurs more in extremely preterm neonates, which means infants born at ≤28 weeks and has a prevalence of about 2-5‰ [23]. A recent meta-analysis shows that, among infants born at ≤ 28 weeks of GA, the prevalence of IVH, though various around the world, is 5-52% for grade III and IV, and 5-19% for grade II [5]. The early maturational trajectories of the brain can be seriously impacted by IVH. The germinal matrix contains precursor cells of neurons and glia. In severe cases (grade III or grade IV), IVH is strongly associated with other conditions, such as posthemorrhagic ventricular dilatation (PHVD), periventricular hemorrhagic infarction (PVHI) and periventricular leukomalacia (PVL), which further damage the white matter and disturb the maturation of neuronal fibers [24], [25], [26], [27]. In terms of long-term outcomes, infants

who survived IVH may suffer from various neurodevelopmental disabilities. It is reported that 5-10% of living newborns with IVH develop major motor deficiencies [26] and over 50% develop cognitive, visual or language issues [28], [29], [30].

1.1.1.2 Hypoxic ischemic encephalopathy

HIE is another major neonatal brain injury that occurs in term-born neonates. As the name suggests, it is due to insufficient or disrupted cerebral oxygen or blood supply during the prenatal, intrapartum, or postnatal periods [16]. Risk factors of HIE include maternal thyroid disease, receipt of antenatal care, infection, aspects of the management of labour and delivery (e.g., placental abruption or uterine rupture) [3]. HIE injuries can show various spatial patterns depending on how acute the decrease of blood flow is. When the decrease is moderate, the cerebral arteries will modulate the blood flow to secure sufficient amounts for the brainstem, cerebellum and basal ganglia, so that the injury will appear more in the cortex and watershed areas (border regions between cerebral areas supported by different arteries). When the decrease is sudden, the injury will be more focused around the thalamus and basal ganglia [31]. Based on the Sarnat staging system [32], by which neonates are evaluated for consciousness, neuromuscular control, autonomic function, seizures, HIE newborns are categorized into stages 1-3, corresponding to mild, moderate and severe stages, respectively. The hypoxic-ischemic events usually occur within 6 hours after birth followed by development of injuries in only a few hours [16]. The prevalence of HIE is recently estimated to be 0.093% in the United States among term-born infants [33], yet the number can reach over 0.2% in developing countries [3]. HIE can lead to death and neurodevelopmental disabilities, including cerebral palsy, impairments of various cognitive functions. A recent trial [14] showed that 85% of infants with severe HIE and 48% of those with moderate HIE either died or had intelligence quotients (IQ) below 70. Among surviving infants, only 41% had no observable disabilities. A standard treatment of HIE is therapeutic hypothermia (TH), during which either only head or full body of the infant will be cooled to 33-34°C for up to 72 hours followed by 6 to 12 hours of rewarming [34]. TH in general initiates within 6-24 hours after birth. Though not all infants with HIE can be eligible for TH [35], the treatment has shown benefits on lowering rates of mortality and severe disabilities [14].

1.1.2 Neuroimaging and monitoring of neonatal brain injury

As neonatal brain injury has a high prevalence and is associated with high mortality along with profound neurodevelopmental sequalae, plus it can happen acutely within a few hours after birth and babies can deteriorate quickly in hours or days. Therefore, early diagnosis and monitoring are of vital importance.

The two most common neuroimaging technologies for characterizing injury are cranial ultrasound (cUS) and magnetic resonance imaging (MRI). cUS is non-invasive, radiation-free imaging tool, which can be used at the bedside. For preterm infants, cUS is recommended to be done at multiple time points after birth to capture the full process of evolution of the injury [36]. Protocols for serial cUS, typically include 3 scans at 0-14 days of life, 25-35 days of life and at term equivalent age (TEA), and have been adopted by many neonatal intensive care units (NICU) [37], [38]. Using serial cUS clinicians can detect and grade GMH-IVH. In more extreme cases, GMH-IVH can develop into PHVD, which typically occurs after 1-2 weeks of IVH. Using cUS PHVD can be monitored and followed along with the general growth of brain until TEA [36]. cUS can also identify cystic PVL, but this is less commonly seen in neonates due to advances in mechanical ventilation patterns. A key limitation of cranial ultrasound (cUS) is that it may not detect abnormalities in certain tissue types in neonates. This is because it typically uses the anterior fontanelle as an acoustic window, which can limit the field of view [39]. Also, cUS cannot be used for long-term continuous monitoring.

For term-born infants with HIE, cUS is also used to identify intracranial hemorrhage, which is an exclusion criterion for TH. Major injuries of thalamus or basal ganglia are also detectable using cUS, but it can take 48-72 hours for injuries to develop, which may surpass the optimal timing for diagnosing HIE and subsequently initiating TH [40].

MRI is another common technique for characterizing neonatal brain injury. It is recommended that neonatal MRI should include a T1-weighted (T1w) sequence, a T2-weighted (T2w) sequence, diffusion-weighted imaging (DWI) and susceptibility-weighted imaging (SWI). More details on scanning sequences can be found in section 1.3. For preterm born infants, MRI at TEA has become a clinical routine for very preterm ones.

Compared to cUS, SWI shows better sensitivity to low-grade IVH [41] and visualization of cerebellar hemorrhage [42], and DWI can indicate diffusive PVL patterns as abnormal diffuse signals [43]. For HIE infants, DWI can detect movement of water within cytotoxic cellular edema that occurs in various patterns of injury [44].

Other MRI sequences used for characterization of neonatal brain injuries include diffusion tensor imaging (DTI), magnetic resonance spectroscopy (MRS), and functional MRI (fMRI). Using DTI, alterations in diffusion parameters have been identified in premature infants with IVH, or who have mild white matter abnormalities [45]. DTI tractography, which maps the connectivity of neuronal fibers, is also a promising tool for studying white matter injury in the preterm brain [46]. MRS can identify cerebral metabolic changes that can occur after hypoxia-ischemia, which can aid in the better understanding of impaired cerebral energy metabolism in neonates with HIE [47].

fMRI measures the blood-oxygen-level-dependent (BOLD) signal as an indication of level of neuronal activities. fMRI is widely used to explore the functional organization and connectome of brain, including newborns with brain injury. In general, preterm birth can lead to altered functional networks compared to healthy term born neonates [48]. Disrupted resting-state networks were seen in very preterm neonates with white matter injury compared to those without [49]. Alterations in functional connectivity have also been reported in other studies in preterm neonates who had various types of brain injuries [50]. Notably, fMRI is considered to be comparable to fNIRS in terms of measuring cerebral hemodynamics [51], which highlights the feasibility of using fNIRS for studying early brain injury.

Electroencephalography (EEG) is commonly used in the HIE population for detecting seizures. Transcranial Doppler ultrasound provides real-time measures of cerebrovascular function; however, this technique requires operators to have extensive knowledge on cerebrovascular anatomy [52]. Other less commonly used imaging modalities to characterize injury in the neonate include computed tomography and positron emission tomography. Both techniques involve exposure to radiation.

In general, the limitations of current imaging technologies highlight the need for non-invasive, easily operable and accessible imaging tools that is capable of continuous monitoring on bedside and offering robust biomarkers for characterizing and tracking neonatal brain injury. In the following sections and chapters, it will be demonstrated that fNIRS has the potential to be a new neuroimaging tool for such purposes.

1.2 Functional near-infrared spectroscopy

In general, there are 3 subtypes of fNIRS, namely continuous-wave fNIRS, frequency-domain fNIRS and time-domain fNIRS. Though basic optical principles are shared among the 3 types, designs of the system, signals acquired and methods for processing vary significantly. As in this study, only continuous-wave fNIRS is used, this section focuses only on this fNIRS subtype, and if not specifically pointed out, term "fNIRS" means only continuous-wave type fNIRS in this chapter.

1.2.1 Physics of fNIRS

Functional NIRS is a non-invasive, radiation-free optical imaging technique that measures concentration changes of hemoglobin. It was first introduced by Jobsis in 1977 [53] for continuous monitoring of cerebral oxygenation. In a typical fNIRS system, there are light sources coupled to light detectors, which measure changes in light intensity. The derivation of hemoglobin concentration changes from light intensity differences between incident and detected lights relies on two phenomena of light propagation in tissues – absorption and scattering.

Light absorption is the transfer of energy from photons to molecules (or atoms) when the two interact. In a non-scattering tissue, light absorption is characterized by Beer-Lambert law, which is defined as

$$I = I_0 e^{-\epsilon_\lambda c l}, \tag{1.1}$$

where I_0 is the intensity of incident light, I is the intensity after absorption of molecules, l is the length light travels, c is the concentration of a chromophore, and ϵ is the molar extinction coefficient which is an intrinsic property of a molecule describing how strongly the molecule absorbs light of a certain wavelength λ. The molar extinction coefficients of

oxygenated hemoglobin (HbO) and deoxygenated hemoglobin (Hb) are shown in Fig. 1.1. The incident light used in fNIRS falls within the wavelength range known as the "optical window," specifically ranging from 650 nm to 900 nm [54]. Inside the window, major tissue molecules (e.g., hemoglobin, water, lipid, melanin) have low intrinsic absorption so that light penetrates deep into the tissue. Absorption property of tissue is also and often denoted by the absorption coefficient $\mu_a = \epsilon(\lambda)c$, where $1/\mu_a$ can be considered as the average distance of a free path a photon travels between absorption events.

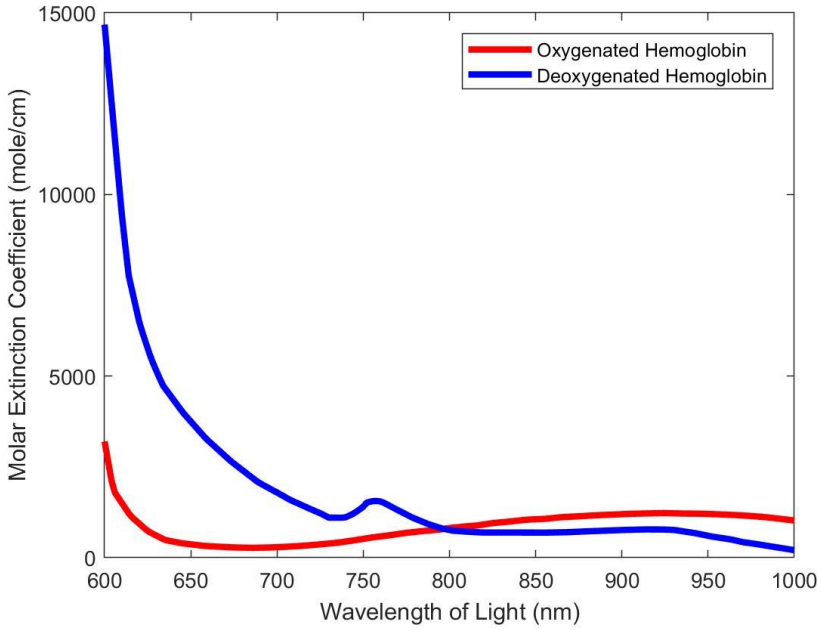

Figure 1.1: Absorption spectrum of HbO and Hb. Data source: W. B. Gratzer, Med. Res. Council Labs, Holly Hill, London.

Scattering of light, specifically elastic scattering which does not change the energy of light, refers to the change in the direction of propagation when a photon interacts with a molecule. Scattering is characterized by the scattering coefficient μ_s, which describes how often scattering events happen, and the asymmetry factor g, which ranges from -1 to 1 and describes the distribution of propagating directions after scattering events. Tissue molecules in general have large μ_s ($\mu_s \gg \mu_a$) and g (over 0.9), meaning the scattering events occur more frequently than the absorbing events, but are largely forward directed, which ensures that light can travel long enough within tissues. Yet a portion of the light

can still travel along a curved trajectory after multiple scattering events within tissues and connect sources and detectors on the same plane.

To further calculate the concentration changes of HbO and Hb from raw light intensity signals, the modified Beer-Lamber law (MBLL) [55] becomes useful. Given two time points t_1 and t_2, the change in optical density of detected light, ΔOD, can be written as

$$\Delta OD = \left(ln \frac{I_{0,t_2}}{I_{t_2}} + G_{t_2} \right) - \left(ln \frac{I_{0,t_1}}{I_{t_1}} + G_{t_1} \right), \tag{1.2}$$

where G is the loss to scattering. Since G relies on the geometry of tissue, which makes it exceedingly difficult to estimate, it is not feasible to directly calculate the concentration of hemoglobin from Eq. 1.2. Note that some fNIRS setup, e.g., time-resolved system, can estimate the scattering effect but not for continuous-wave system [56]. In MBLL, G is assumed to be a constant over time, because absorption coefficient μ_a of hemoglobin is much more susceptible to change in concentration, compared to scattering coefficient μ_S [57]. Then,

$$\Delta OD = ln \frac{I_{0,t_2}}{I_{t_2}} - ln \frac{I_{0,t_1}}{I_{t_1}} = ln \frac{I_{t_1}}{I_{t_2}} = \epsilon_\lambda c_{t_2} l - \epsilon_\lambda c_{t_1} l = \epsilon_\lambda l(\Delta c). \tag{1.3}$$

It is obvious that the tissue is a mixture of various molecules including mainly lipid, water, melanin and hemoglobin. In this setup, only hemoglobin is considered since it is a major absorber compared to other molecules and takes up a generous portion of the tissue. With both HbO and Hb, Eq. 1.2 can be rewritten as

$$\Delta OD = \epsilon_{HbO,\lambda} \Delta c_{HbO} l + \epsilon_{Hb,\lambda} \Delta c_{Hb} l. \tag{1.4}$$

By using two wavelengths of light, Δc_{HbO} and Δc_{Hb} can be derived from

$$\begin{aligned} \Delta OD_{\lambda 1} &= \epsilon_{HbO,\lambda_1} \Delta c_{HbO} l_{\lambda_1} + \epsilon_{Hb,\lambda_1} \Delta c_{Hb} l_{\lambda_1} \\ \Delta OD_{\lambda 2} &= \epsilon_{HbO,\lambda_2} \Delta c_{HbO} l_{\lambda_2} + \epsilon_{Hb,\lambda_2} \Delta c_{Hb} l_{\lambda_2} \end{aligned} \tag{1.5}$$

as

$$\begin{aligned} \Delta c_{HbO} &= \frac{\epsilon_{Hb,\lambda_1} \dfrac{\Delta OD_{\lambda 2}}{l_{\lambda_2}} - \epsilon_{Hb,\lambda_2} \dfrac{\Delta OD_{\lambda 1}}{l_{\lambda_1}}}{\epsilon_{HbO,\lambda_2} \epsilon_{Hb,\lambda_1} - \epsilon_{Hb,\lambda_2} \epsilon_{HbO,\lambda_1}} \\ \Delta c_{Hb} &= \frac{\epsilon_{HbO,\lambda_1} \dfrac{\Delta OD_{\lambda 2}}{l_{\lambda_2}} - \epsilon_{HbO,\lambda_2} \dfrac{\Delta OD_{\lambda 1}}{l_{\lambda_1}}}{\epsilon_{HbO,\lambda_2} \epsilon_{Hb,\lambda_1} - \epsilon_{Hb,\lambda_2} \epsilon_{HbO,\lambda_1}}, \end{aligned} \tag{1.6}$$

where ΔOD can be directly measured from detectors of fNIRS system, and l is estimated [58].

Generally, the trajectory of a photon travelling from a source, through tissues, and not absorbed but end at a detector, is considered to be banana shaped, as shown in Fig. 1.2. The trajectory can be mathematically modelled as a photon hitting density function of possible locations that the photon travels through. The photon hitting density is proportional to the probability density of the photon at unit volume. Introduced in [59], given a photon initiated at location $(0,0,0)$ and detected at $(d,0,0)$, the hitting density P_n at location (x,y,z) is defined as

$$P_n(x,y,z) = \frac{z^2\, exp\left(-k\left\{(x^2+y^2+z^2)^{\frac{1}{2}} + [(d-x)^2+y^2+z^2]^{\frac{1}{2}}\right\}\right)}{(x^2+y^2+z^2)^{\frac{3}{2}}[(d-x)^2+y^2+z^2]^{\frac{3}{2}} \times \left[k(x^2+y^2+z^2)^{\frac{1}{2}}+1\right]\left\{k[(d-x)^2+y^2+z^2]^{\frac{1}{2}}+1\right\}}, \quad (1.7)$$

where k is estimated by Sassaroli et al. as 0.23 [60]. Eq. 1.7 is derived from analyzing diffusive photon flux in homogeneous medium and achieves good correspondence with Monte-Carlo simulation [59]. Eq. 1.7 can be combined with a brain mask in, e.g., MNI space, to limit the domain of the function within cerebrum.

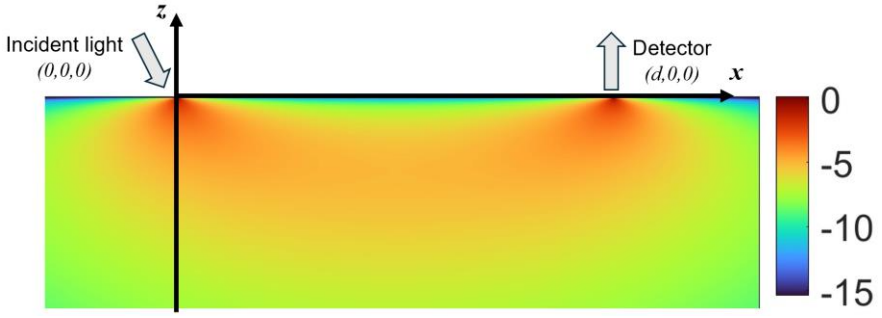

Figure 1.2: A demonstration of Eq. 1.7 is provided. To enhance colour differentiation, the colourbar indicates the value of $ln(P_n)$. For the figure, y is set to 0, and domain of $z > 0$ is also omitted, because the equation is rotationally symmetric to x axis.

Based on the modelling, longer separations between light sources and detectors allows photons to reach deeper layers (e.g., cerebral cortex, while shorter separations are focused on extracerebral layers, Fig. 1.2). A coupling of a source and a detector is often referred to as a channel. A typical design of fNIRS system usually has approximately 3 cm separation

of channels targeted towards the cerebral cortex, and shorter ones (<1 cm) to acquire signals from superficial layers.

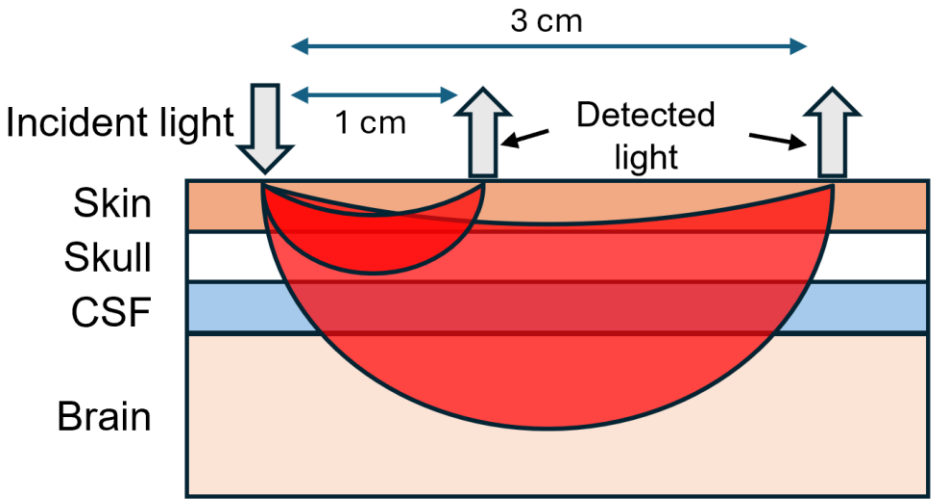

Figure 1.3: Photon trajectories with different separations between light sources and detectors. CSF: cerebrospinal fluid.

1.2.2 Preprocessing fNIRS signals

The raw signals obtained with fNIRS will contain noise from various sources, including background environmental noise, system drift, motion, and systemic physiology. Therefore, preprocessing, or denoising, is essential for obtaining neurologically meaningful data. Note, there is no gold standard for the most appropriate denoising methods to use, but typically, a preprocessing pipeline includes some or all the following steps: data exclusion, motion correction, band-pass filtering, and removal of systemic physiology. In general, it is recommended to customize and optimize the preprocessing pipeline based on the dataset being analyzed [61].

The fNIRS signals may be saturated with noise and not yield any useful information. In such cases, the signals should be excluded from further analysis to avoid misinterpretations of the data. Visual inspection in either time or frequency domain of the signals can be an option. A signal filled with large spikes or cliffs should meet exclusion criteria. Also, cardiac signal comes at a fixed frequency, around 1 Hz. If such frequency is present in

frequency domain, it indicates that the signal is coupled with physiological hemodynamics, but not purely noise [62]. Visual inspection relies on the experience of operators on distinguishing noisy signals from the good, therefore, quantified metrics can also be used to evaluate the quality. Coefficient of variance (CV) is a simple measurement and is used by various commercialized fNIRS software. Also, there is a method introduced in [63] that can measure signal-to-noise ratio through automatically detecting cardiac frequency.

Though fNIRS is known for its resistance to movements of tested subjects [64], motion artifacts may still appear in fNIRS signals as sharp spikes or drastic shifts in baseline, mostly due to disrupted contact between probes and skin. Numerous motion correction methods have been proposed. A common one, introduced in [65], identifies the motion artifacts by calculating standard deviation (STD) within a sliding window, then applies spline interpolation on those sections with STD over a threshold. Notably, this method sometimes combines with Savitzky-Golay filter [66] to further smooth signals. Another popular method is wavelet filtering [67], [68] which decomposes a signal into wavelets, removes the wavelets representing noise components, then re-assembles the whole signal. It is worth mentioning that spline interpolation combined with wavelet filtering is reported to be particularly good with very noisy data from infants [69]. For continuous monitoring of the neonatal brain, prioritizing methods that operate in real-time is important. This is particularly relevant because spline interpolation can promptly detect and rectify motion as soon as it happens. Other options include Kalman filtering [70], and independent component analysis (ICA) [71].

Band-pass filtering is for removing very low-frequency system drift and high-frequency background noise and some types of systemic physiology such as cardiac dynamics. A recent study demonstrated that high-order finite impulse response filter works best [72] but it was never tested on resting-state or neonatal data. There are a few considerations to be taken into consideration when choosing the cutoff frequency of the filter. Firstly, cutoff frequency should not be close to the frequency of tasks in experimental paradigm to avoid task related response being filtered out. And the task frequency should be away from common physiological noise frequencies to avoid false positives and false negatives in hemodynamic responses to the task [73]. Also, for resting-state analysis, note that the

intrinsic fluctuation of brain hemodynamics is low-frequency (<0.1 Hz) [74], which allows a lower cutoff frequency for a low-pass filter, yet the signal may still be contaminated by Mayer waves (~0.1 Hz).

The aforementioned steps can be applied either before or after calculating hemoglobin concentration change with the MBLL from raw optical density data.

Light detected in fNIRS can contain photons from extracerebral layers (Fig. 1.2) which contributes to signal components irrelevant to cerebral hemodynamics. These extracerebral signals contain Mayer waves, respiration and cardiac cycles bringing more physiological noise and irrelevant scalp hemodynamics [75]. It has become increasingly popular to use short-distance channels (SDC) to address this issue. SDCs are from source-detector couplings of shorter separation (typically <1 cm) and mainly record extracerebral signals (Fig. 1.2). By regressing out SDC signals from regular channels, the extracerebral components within regular channels can be weakened. Note that such regression is typically done after the SDC and regular channel signals being corrected for motion, band-pass filtered and applied with MBLL. One can use general linear models (GLM) for regression. GLM is defined as

$$Y = X\beta + R, \tag{1.8}$$

where X contains single or multiple predictors, Y contains an outcome variable, R is the residual or error, and entries of β are scaling factors describing how much predictors in X contribute to the Y. β can be estimated as

$$\beta = (X^T X)^{-1} X^T Y. \tag{1.9}$$

For SDC regression, X is the SDC signals, Y is regular channels, and the residual R would be the signal without SDC components. Note there is no consensus on how to build X. For a regular channel, one can compose X with geometrically close SDCs, all SDCs, average/median of all SDCs, etc. [76], [77]. Also, note that it is rather uncommon to use SDCs for neonates. Thinner scalps and skulls limit extracerebral components within regular channels, and make it too short for separations of SDCs to be realized within fNIRS hardware [75]. Usually, SDC regression is the last step of fNIRS preprocessing, but sometimes pre-whitening is also used to remove autocorrelation within the time series [78]. The denoised fNIRS signals can be used for a variety of analysis, which cannot be

exhaustively documented in this dissertation, but some which are related to this study will be introduced in section 1.4.

1.2.3 Hemodynamic response

The changes in hemoglobin concentration resolved through MBLL can reflect neural activity due to the mechanism of neurovascular coupling. Neural signaling processes in the brain, including generation and propagation of action potentials, synthesis, release, reception and scavenging of synaptic neurotransmitters need energy from adenosine triphosphate, which is primarily produced from oxygen and glucose transported by blood. For example, when neurons need to perform certain functions triggered by motor or cognitive tasks, neural signaling becomes more frequent and therefore consumes more energy. Various chemical signals are released by neurons or astrocytes through multiple pathways, which would lead to dilatation of nearby blood vessels [79]. While glucose concentration can be balanced between consumption and new arrivals to maintain a steady level, it is observed that HbO will be excessively supplied, creating an increase in HbO and decrease in Hb, which can be detected by fNIRS. Such a process is described as the hemodynamic response. Note that in fNIRS data, the neonatal hemodynamic response may show an increase in Hb [80], potentially due to immature neurovascular coupling mechanisms.

1.3 Magnetic resonance imaging

MRI is considered the gold standard for neonatal neuroimaging and is widely used for clinical diagnosis of neonatal brain injury. This study is focused on fNIRS, yet under many scenarios fNIRS data are compared to or validated by MRI data from the same group of subjects. Therefore, in this section, basics of MRI and some common scanning sequences will be introduced.

1.3.1 Basics of MRI

The contrast within MRI images comes from different rates of relaxation from excited magnetization to equilibrium among different tissue molecules [81]. During MRI

acquisition, tissues are placed in a constant magnetic field B_0 so that protons (mainly hydrogen for tissues) are magnetized, and their spins follow the direction of B_0, which is usually defined as longitudinal. Along the transverse plane perpendicular to B_0, an impulsive excitation magnetic field B_1 of radiofrequency would tip the spins towards the transverse plane and start precession. Precessing spins can produce rotating magnetization then induce a tiny electric current (a signal) within a receiving coil nearby. These signals can be later processed into MRI images.

If the protons are in a perfectly homogeneous magnetic field, they will all precess at the same rate. Yet in practice, distortions in magnetic field exist due to heterogeneity of tissues. To be specific, magnetic susceptibility varies among different molecules and protons are also magnetic and influencing each other. Therefore, precessions of spins will proceed at different rates gradually causing phase differences among them. Over time, the overall magnetization along the transverse plane will diminish exponentially, which is called T2* relaxation. T2* is the time it takes for the signal from rotating magnetization reduced to $1/e$ of its maximum at the very beginning of the relaxation. Distortions in magnetic field can be decomposed into two components. The first one is spatially and temporally static and is induced by the magnetic susceptibility and design of the B_0 magnet. And the second one is temporally heterogeneous and induced by interactions between protons and thermal changes of tissues. The two components can be separated by using a so-call "spin-echo" first proposed in [82], whereby a second impulsive magnetic field with direction of opposite B_0 is applied shortly after T2* relaxation to compensate for T2' relaxation so that an echo signal align with only T2 relaxation will present afterwards. Relaxation induced by temporally static distortion is called T2' relaxation and the other one is called T2 relaxation, where T2' and T2 refer to the time for relaxation to $1/e$ of maximum. Note that T2* relaxation is the combination of T2 and T2' relaxation so T2* time is shorter than T2. Relaxation not only happens in the transverse plane, but also along the longitudinal axis, because energy that spins absorb from impulsive B_1 dissipates over time so that the magnetization along the longitudinal axis grows. T1 relaxation characterizes this process and T1 is the time for signal to reach $(1 - 1/e)$ of maximum. At one time point, different

tissues will have different signal magnitudes due to various relaxation rates so that imaging contrast can be formed. For tissues within or close to the brain, T1 is much larger than T2.

T1w imaging and T2w imaging rely on two parameters: the repetition time (TR) and the echo time (TE). TE is the time between B_1 and the peak of the echo signal, and TR is the time between two consecutive B_1 pulses. T1w and T2w imaging rely on the selection of TR and TE respectively to maximize the signal differences between tissues focused on. For example, infarctions or inflammations are bright on T2w images while white matter appears darker, which makes it specifically useful for identifying diffusive injury patterns [36]. In general, T1w imaging has shorter TR and TE times while T2w has longer times for these parameters. Note that the neonatal brain has higher water content than the adult brain, due to lower myelin concentrations[83], so that the parameter settings should be optimized to have better imaging quality [84].

During image acquisition, gradients are applied to B_0 to achieve slice selection, frequency and phase encoding so that only protons in one slice can be excited at a time and the precessions of spins can have different frequencies and phases, to decompose the one signal detected into multiple signals corresponding to their geometrical origins [81]. Typical spatial resolution of T1w images is about $1 \times 1 \times 1$ mm^3 and can be improved by using a scanner with higher B_0 (e.g., 3 Testa or higher) [85].

1.3.2 Functional magnetic resonance imaging

The BOLD signal measured by fMRI originated from the relative change between HbO and Hb. As mentioned in section 1.2.3, the hemodynamic response reflects increases in HbO and decreases Hb. Magnetic susceptibility of HbO and Hb can lead to different reactions to the B_0 field. HbO being diamagnetic while Hb being paramagnetic creates local heterogeneity of the magnetic field further affecting T2* relaxation times of the tissues nearby and creating BOLD contrast. Such contrast depends on the amount of Hb due to its paramagnetism opposed to diamagnetism of most tissues [86]. Temporal sampling rate is determined by the TR, which is typically 2-3 s, yet with multi-slice acquisition where multiple slices along longitudinal axis are acquired simultaneously, the

TR can be reduced to below 1 s [87]. The spatial resolution is typically about 3 × 3 × 3 mm^3 for a voxel, lower than T1w imaging.

Preprocessing of fMRI data has been integrated into many well developed and user friendly software (e.g., FMRIB Software Library, (FSL)) [88], Analysis of Functional NeuroImages (AFNI) [89]). A preprocessing pipeline can include all or some of the following steps: skull stripping, slice-timing correction, motion correction, spatial smoothing, temporal filtering (band-pass) and registration to a standard template. For some analytic routines, physiology regression is also applied using white matter or whole-brain averaged signals as nuisance regressors. Traditionally, fMRI studies are focused on grey matter where most neuronal activity occurs, yet recent findings suggest that white matter BOLD signal also contains meaningful hemodynamic responses, raising questions on using the signal as a regressor [90].

1.4 Functional connectivity and graph theory

Functional connectivity (FC) of brain activity refers to the statistical dependency or temporal synchronization among cerebral regions. Such dependency or synchronization can be associated with cognitive or sensory functions. FC can be derived from functional imaging data including fMRI, fNIRS, EEG, or Magnetoencephalography, which yields time series obtained from different brain regions. This section is mainly focused on fNIRS and fMRI that both evaluate cerebral hemodynamics and methods for deriving and analyzing connectivity are mostly developed earlier for fMRI and expanded to fNIRS. The time sequences being studied, for fMRI, can be BOLD sequences extracted from individual voxels or as average over many voxels forming as large as an anatomical lobe. For fNIRS, they can be hemoglobin concentration signals from channels which correspond to cortical regions.

1.4.1 Functional organization of brain and resting state

FC can be used to reveal the functional organization of the developing brain. It is obvious that neurons interact with each other to perform certain cognitive functions, forming a network containing numerous of them. Multiple functional networks have been identified

from brain imaging, traditionally by inducing activation of brain regions from specifically designed tasks and stimuli.

Resting-state functional connectivity (RSFC) has also been shown to provide organizational information on brain function [91], [92], [93], [94]. Resting-state functional imaging is captured when participants are performing no active tasks and remain still with eyes open or closed. External stimuli should be controlled for as much as possible. Early work from Biswal et al. [74] using fMRI demonstrated that during rest hemodynamic fluctuations still exist, and functional networks emerge. It is argued that such spontaneous processes originate from a combination of unconstrained conscious activity (e.g., mind wandering) and intrinsic neural activity, which is reflected by brain regions that recruit the same cognitive functions will have strong connections, and form functional networks [95].

One functional network specifically emerges from RSFC analysis is the default mode network (DMN) which roughly expands around posterior cingulate cortex, lateral parietal cortex, and medial prefrontal cortex. The DMN is identifiable as it is more activated during resting state [96]. DMN is shown to be involved in multiple functions, such as mind wandering, memory recollection, theory of mind, which reflects the ability of understanding thoughts, emotions and intentions of others [97]. Other identified networks include visual, auditory, somatosensory, and the central executive network, among others. Notablely, Power et al. [98] detect multiple functional networks mentioned above using clustering methods with RSFC maps.

RSFC can offer benefits when it comes to establishing significance in clinical contexts. It is estimated that spontaneous neural activity consumes most of the energy (about 80%) supplied to the brain [99]. Therefore, to have a comprehensive evaluation of cerebral hemodynamics and function, resting-state data is essential. Also, resting-state acquisition does not require active participation by the subjects, so it is better for patients who cannot be instructed or cope with tasks, including those with impaired cognitive ability, individuals with disabilities, young children and infants.

1.4.2 Variations of functional connectivity

Numerous methods have been proposed to calculate FC, which are based on different perspectives on how to characterize the relationships amongst time sequences and cannot be listed exhaustively here. Some typical ones that are widely applied will be introduced in this section.

Principal component analysis (PCA) is a data-driven technique that breaks down a data matrix into components, determined by the variance they explain. The construction of the data matrix can vary depending on the specific perspective intended to be explained. For example, in a given fMRI image, we can build the data matrix with all of the voxels on one axis and all time points on the other. Determining whether to analyze spatial or temporal variance depends on whether the voxels are arranged along rows or time points. The first component contains the direction along which the data matrix shows maximal variance. By projecting the data matrix onto the first component, one can obtain, for example, a spatial map where voxels with close values are considered to share similar temporal patterns therefore have strong FC between them. The strength of using PCA applied to FC data is that it does not rely on presumptive models of hemodynamic functions, yet one of the limitations is that it could split important features into multiple components [100].

Similar to PCA, independent component analysis (ICA) is another matrix decomposition method that identifies statistically independent components and common features shared within components [101]. ICA is considered to be more flexible than PCA as PCA can be constrained to identify either temporal or spatial variance, but does not consider both simultaneously [101]. With ICA, one can obtain various components such as time sequences corresponding to various task stimuli and noises from different sources, and how spatially the components are weighted.

Pearson correlation coefficient (PCC) is probably the simplest way to calculate FC. Given two time sequences x_1 and x_2, PCC is defined as

$$PCC = \frac{\sum_\tau \left(x_{1,\tau} - \overline{x_1}\right)\left(x_{2,\tau} - \overline{x_2}\right)}{\sqrt{\sum_\tau \left(x_{1,\tau} - \overline{x_1}\right)^2}\sqrt{\sum_\tau \left(x_{2,\tau} - \overline{x_2}\right)^2}}, \tag{1.10}$$

where $\bar{x}$ denotes the average of the time sequence. PCC tests for linear correlations and ranges from -1 to 1 where 1 means perfectly positively correlated. The time sequences can be extracted from single voxels, or as averages over larger brain regions. Single correlations between two specific voxels or regions can be examined. PCC can also be used for seed-based analysis, where a seed time sequence is selected from a voxel or region with certain known properties, and other voxels and regions are correlated with this one to test how much they share the same properties. In addition, correlational analysis can be done without seeds, but between many pairs of regions to form a connectivity map. Based on the map, topological properties can be evaluated and analyzed on different levels from local to global. Note that if two regions both have strong correlations with a third region, the two will be very likely to strongly correlated with each other. Therefore, to examine a more direct connection between two regions, partial correlations are proposed in order to remove any third-party effects on a connection [102]. The most straightforward way to calculate partial correlations is to regress out all other time sequences from the two being examined. A more statistically effective method has been proposed in [103]. Given ith and jth brain regions from a total of m, partial correlation ρ_{ij} can be calculated as

$$\rho_{ij} = -\frac{p_{ij}}{\sqrt{p_{ii}p_{ij}}}. \tag{1.11}$$

$P = [p_{ij}] = [cov(X)]^{-1}$ where $cov(X)$ is the covariance matrix of data matrix $X = [x_1, x_2, \dots, x_m]^T$ and $[cov(X)]_{ij} = \sum_\tau (x_{i,\tau} - \bar{x_i})(x_{j,\tau} - \bar{x_j})$ where x is time sequence.

PCC and partial correlation are generally considered as undirected or bidirected connections where information flows both ways, yet there are also directed connections, a group of which is causality modelling. Such modelling is based on that neural signaling passes from one neuron to another then one region to another, forming time lag and causality. One common way to model causality is through Granger causality which is based on solving GLM models of representing future time sequences with weighted combinations of past ones. In practice, given a future time sequence, Granger causality can be calculated. By projecting the data matrix onto the first component, one can obtain, for example, a spatial map where voxels with close values share similar temporal patterns and therefore have strong FC between them [104]. Another causality model is dynamic causal modeling

where a nonlinear dynamic system describing interactions among neural states is predefined and tested with functional images [105].

FC obtained from fMRI and fNIRS is compared through various approaches. Sasai et al. [106] use seed-based correlation on HbO, Hb and BOLD recordings of adults and show good correspondence in functional networks identified, including dorsal attention, fronto-parietal control and DMN. Duan et al. [107] present positive correlation between fMRI FC strength and fNIRS, and in general good similarity of connectivity maps. Bulgarelli et al. [108] apply dynamic causal modelling on data from one infant and show good correspondence of the causal models between the two modalities. However, comparisons are never tested on neonates on a larger scale. And due to the different hemodynamic response of infants compared to adults [109], fMRI, which focuses more on relative differences between HbO and Hb, could yield different functional connectivity patterns from newborns.

1.4.3 Graph theory

In general, relationships that are of interactive or inducive nature can be modeled as graphs, which are also referred to as networks, or connectivity maps in terms of brain FC. A graph comprises two fundamental components: nodes and edges that connect these nodes. The edges can be either directed or undirected. For brain FC, correlation-based connectivity is generally undirected and causality-based connectivity is directed. This section mainly focuses on undirected graphs as the methods in the subsequent chapters use correlation-based connectivity.

Mathematically, a graph G can be defined as $G = (V, E)$ where V is the set of all nodes and E is the set of all edges. Note that an edge can be a self loop connecting one node with itself. Fig. 1.3 shows a demonstration of a simple undirected graph where $V = \{v_1, \dots, v_5\}$ and $E = \{e_{12}, e_{13}, e_{23}, e_{24}, e_{45}\}$. A graph can be represented by the adjacency matrix $A = [a_{ij}]$, where a_{ij} can be either binary for unweighted graphs, denoting the existence of an edge, or $a_{ij} \in R$ for weighted graphs. By analyzing a graph, topological information can be learned and interpreted with practical meanings. In general, a graph can be analyzed on

three levels – local, subgraph and global. Note that many metrics can only be applied to graphs with no negative weighted edges, including those applied in this study, plus the interpretation of negative edges are being argued widely [110]. Therefore, it will not be distinguished whether a method can be used with negative edges in this dissertation and graphic metrics used in this study are all calculated with negative edges removed, which is a common strategy adopted by researchers [98], [111], [112].

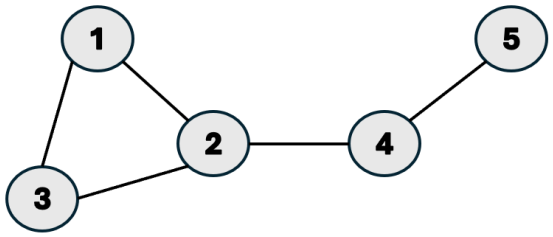

Figure 1.4: An example of a simple graph.

Local analysis focuses on properties of individual nodes or edges. The basic property of an edge is its existence or weight, but it can also be its importance within the graph. A classic metric for measuring the importance is edge betweenness centrality, which can be calculated as, given an edge e,

$$BC_E(e) = \sum_{i,j \in V, i \neq j} \frac{\sigma(i,j|e)}{\sigma(i,j)}, \tag{1.12}$$

where $\sigma(i,j)$ is the number of shortest paths between node i and j while $\sigma(i,j|e)$ is the number of shortest paths between node i and j going through e. Note that Eq. 1.12 must be calculated on connected graphs where there is at least one path between any pairs of nodes. The shortest path, which can be identified by the classic Dijkstra's algorithm [113], describes the most efficient pathway for information transmission. The brain is also a very efficient system for passing information therefore can be characterized by shortest paths. It is widely discussed that the brain is a small-world network where nodes are not all connected but the shortest paths between any pairs of them are short [114]. Node property can also be described as the importance or the centrality of a node. Given a node i, common centrality metrics of i include degree centrality which is defined as

$$DC(i) = \sum_j a_{ij}\,, \tag{1.13}$$

closeness centrality which is the distance (length of shortest path) between a node between all others, betweenness centrality which is similar to Eq. 1.12 but now counting the number of shortest paths going through a node, eigenvector centrality where the ith eigenvector of adjacency matrix A contains the relative centrality of i to other nodes, etc. Nodes with high centrality are often considered as hubs in the graph. Studying hubs in brain networks gives regions with central roles of interactive processes and neural communications [115]. Another type of nodal property is based on its involvement within a local community. For example, clustering coefficient of a node is defined as the proportion of edges among its neighbors over all possible edges. Clustering coefficient of node i is

$$CC(i) = \frac{1}{DC(i)[DC(i)-1]} \sum\nolimits_{h,j} a_{hi} a_{ji} a_{hj}\,, \tag{1.14}$$

Efficiency of a node is calculated as the average of inversed distances between any pairs of other nodes neighboring the node being investigated (mathematically defined in Eq. 3.4). Such measurements are closely related to small-worldness of graph therefore widely adopted for studying brain FC [116].

Subgraphs of a graph, containing only a subset of V and E, can be either manually defined based on certain known properties of nodes, such as anatomical locations of brain regions, or automatically identified with clustering algorithms. Multiple clustering algorithms have been applied to brain networks for identifying functional communities. Power et al. [98] use a Louvain-like algorithm which is also adopted in Chapter 3 of this study. Firstly introduced by Blondel et al. [117], Louvain algorithm is aimed optimized modularity. The modularity can change with how exactly a graph being clustered and is defined as

$$Mod(C) = \frac{1}{\sum_{i,j} a_{ij}} \sum\nolimits_{i,j} \left(a_{ij} - \frac{DC(i)DC(j)}{\sum_{i,j} a_{ij}} \right) \delta(i,j), \tag{1.15}$$

where $C = \{c_1, \dots, c_K\}$ given K clusters in total, c_k is a set containing nodes belonging to kth cluster, and $\delta(i,j)$ is 1 if i and j are in the same cluster or otherwise 0. Intuitively, modularity measures the ratio of edges within clusters over those between clusters. The algorithm has a hierarchical structure, where every node will be assigned to its own cluster at first, followed by randomly inserting or removing nodes into or from clusters until modularity changes only insignificantly. Other clustering algorithms are also used on brain FC, e.g., matrix factorization, etc., with clustering results evaluated by modularity [118].

Global analysis captures the overall properties of a whole graph. It can be a simple average over local properties or calculated in a more macroscopic way. For example, global clustering coefficient can be the average over nodal one (Eq. 1.14) or be defined globally as in Eq. 3.3. Similarly, network efficiency of a graph can be an average of Eq. 3.4, or be defined as

$$NE_{glob} = \frac{1}{|V|(|V|-1)} \sum_{i \neq j} \frac{1}{d_{ij}}, \tag{1.16}$$

where $|V|$ is number of nodes and d is the distance between two nodes. NE_{glob} can be further normalized, being divided by the efficiency of a randomly built graph with the same V but different E [119], [120].

1.4.4 Studying neonatal brain injury with functional connectivity

To demonstrate RSFC can be a reliable approach for characterizing neonatal brain injury and potentially be biomarkers, this section will list some related studies showing altered FC within infants with brain injury.

Preterm birth in general alters functional connectivity patterns, with or without significant injuries. Doria et al. [121] scanned preterm born infants, with no focal abnormalities detected on MRI, from early preterm to TEA and identify multiple functional networks using ICA and seed-based correlations. Compared to term-born healthy controls, most functional networks emerged early in development. However, differences exist when preterm babies reached TEA compared to healthy term newborns. For example, motor, somatosensory, executive control, and dorsal visual networks are clearly unilateral for preterm babies but bilateral for term-born neonates. Also, DMN is significantly larger in preterm infants. Smyser et al. [122] followed very preterm infants to TEA, excluding those with grade III and IV IVH, and found disrupted development of thalamus-cortex connectivity. They also found altered medial prefrontal cortex which is part of DMN. Another study from Smyser et al. [123] showed decreased correlation connectivity in several functional networks, including the DMN, frontal-parietal, and language networks, within preterm born infants without serious injuries, compared to healthy controls. Ball et al. [124] use machine learning to differentiate preterm from term infants and showed that

connections within the basal ganglia and frontal cortex are specifically powerful at distinguishing the two groups. An fNIRS study from White et al. [125] showed that functional correlation is weaker within occipital lobe. Fuchino et al. [126] also used fNIRS and showed significantly decreased connectivity over parietal lobe and some increased interhemispheric connectivity, compared to term-born controls. Combined with graph theory analysis, Cao et al. [127] describe a gradual segregation of functional networks from 31 to 42 weeks postmenstrual age, demonstrating an increase in the clustering coefficients and characteristic path length. The presence of focal injury, such as PVL, can be a modulator of FC as well. Duerden et al. [49] compared preterm neonates with or without white matter injury and showed weaker bilateral connectivity in visual, somatosensory and parietal cortex in the injury group. Smyser et al. [128] reported decreased connectivity within motor, visual, thalamus and auditory cortices, which was associated with the severity of white matter injury. Lee et al. [129] examined neonates with PVL and also found decreased network efficiency in several functional networks.

Term-born infants with HIE have also been examined by applying FC to functional imaging data, although not as many studies have been performed compared to preterm neonates. Overall, HIE is associated with altered brain connectivity. Tusor [130] scanned fifteen newborns with HIE after undergoing TH and identified auditory, somatomotor, visual and default mode networks, which were all altered compared to healthy controls. Further, Jiang et al. [131] showed that HIE newborns have reduced intra-hemispheric connectivity between primary motor regions and increased connectivity between motor regions and frontal, temporal and parietal cortices. Lastly, Zhang et al. [132] used fNIRS to scan HIE newborns before they receive TH and reported higher clustering coefficient, network efficiency and small-worldness compared to health newborns.

Note that, in general, there are mixed findings on whether neonatal brain injury would lead to increased or decreased connectivity. While many studies show weakened connectivity within neonates with brain injury [122], [123], [125], [128], some other studies also show increased graph theory metrics [133], [134], or connectivity strength [126], [135].

1.5 Machine learning

Machine learning methods can be generally defined as a category of statistical algorithms designed to learn hidden information from data and perform certain tasks without explicit instructions [136]. During the last few decades, machine learning has been drawing increasing interest in areas such as clinical decision making, including diagnosis, outcome prediction, and treatment optimization. [137]. In this thesis, machine learning methods were used to classify two groups or regressing continuous values of dependent variables. Since there are numerous machine learning methods and variants developed that have been applied in countless scenarios, this section will introduce some related machine learning methods that were used in this thesis and some of the applications when combined with neuroimaging.

1.5.1 Conventional methods

In general, conventional methods are those without the concept of deep learning or the use of artificial neural networks (ANN). In a broad sense, matrix factorization methods such as PCA also fall into this category.

Support vector machine (SVM) is one of the most commonly used machine learning methods. It is supervised so that labels of samples are to be provided for training. SVM for classification finds two parallel hyperplanes that separate the two classes (i.e., no instances between the two planes if the two classes are separable), and are as far away as possible from each other. Given a training dataset $\{(x_1, y_1), \dots, (x_n, y_n)\}$ where x is the feature vector of an instance and y is the label being either -1 or 1, if the two classes are separable, and the hyperplane can be written as

$$wx - b = 0, \tag{1.17}$$

where w and b can be obtained by optimizing the following:

$$min\|w\|^2, s.t. y_i(wx_i - b) \geq 1 \tag{1.18}$$

where ||w|| is the norm of w and the distance between two hyperplanes. The constraint ensures the instances fall on the correct side of hyperplanes. Yet in practice, the two classes

are not always separable with given features. Therefore, instead, a so-called soft margin is calculated from a modified Eq. 1.18 is proposed as

$$min\|w\|^2 + \Psi \sum_i \phi_i \, , s.t. \, y_i(wx_i - b) \geq 1 - \phi_i, \phi_i \geq 0, \tag{1.19}$$

where ϕ_i determines if x_i falls one the wrong side of hyperplanes and $\phi_i = \max[0, 1 - y_i(wx_i - b)]$, and Ψ is a penalty parameter for instances on the wrong side. Solving Eq. 1.19 can yield some x_i being chosen as support vectors so that hyperplanes will be exactly on these vectors. By slightly modifying Eq. 1.18, one can do support vector regression (SVR)

$$\min\|\mathrm{w}\|^2 \, , s.t. \, |y_i - wx_i - b| \leq \epsilon, \tag{1.20}$$

so that $wx + b$ can predict the exact value of y.

1.5.2 Artificial neural network

Artificial neural networks (ANN) are a loose approximation of the neural networks of the human brain, where a basic unit of ANN, or a node, takes a data input, processes it, then passes the output to other nodes connected to it. ANN is the foundation of deep learning where numerous nodes stacked up forming multiple layers, each of which also contain many nodes. Deep learning outperforms conventional methods in various applications. A typical ANN node can have the structure shown in Fig. 1.4. Given an input $h = (h_1, \dots, h_k)$, the output is $h' = \sigma(\sum_i h_i w_i)$ where σ is an activation function always nonlinear since the relationship between input and expected output is not always linear. Some common activation functions include Sigmoid, Tanh, rectified linear unit (ReLU), etc. [138]. With many nodes, a typical fully connected feedforward ANN can be like Fig. 1.5.

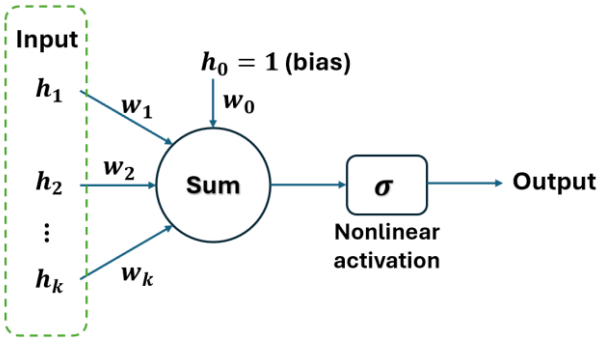

Figure 1.5: A typical structure of an ANN node.

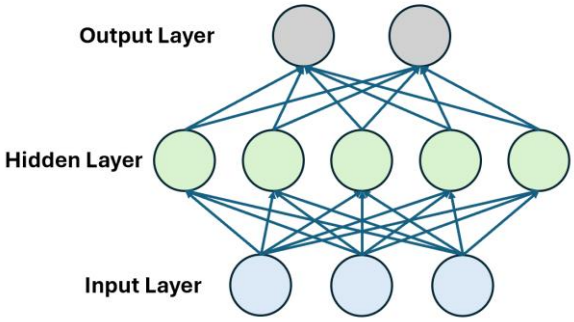

Figure 1.6: A simple demonstration of ANN structure. Each node corresponds to a unit in Fig. 1.4.

ANN models can be used for both supervised and unsupervised learning. For supervised learning, the output of the model is evaluated by comparing it with the true values through a loss function. And the process of training the model is to optimize the loss function. For classification tasks, a common loss function is cross-entropy. To use cross-entropy, each node in the output layer should correspond to a class, and the outputs can be normalized typically with a softmax function. Given an output from one input instance $Y_{pred} = \left(y_{pred}^1, \dots, y_{pred}^K\right)$ for K-class classification, softmax is defined as

$$\left[\sigma_{softmax}\left(Y_{pred}\right)\right]_k = \frac{e^{y_{pred}^k}}{\sum_{q=1}^{K} e^{y_{pred}^q}}, \tag{1.21}$$

so that $\sum_{k=1}^{K} \sigma_{softmax}\left(Y_{pred}\right)_k = 1$ and $\sigma_{softmax}\left(Y_{pred}\right)_k$ is positive. The outputs can be referred as probabilities of the instance belonging to classes. Then, given N instances in total, cross-entropy loss function L_{CE} can be calculated as

$$L_{CE} = -\sum_{n=1}^{N} \left(Y_{true,n}\right)_k \, log\left(Y'_{pred,n}\right)_k, \tag{1.22}$$

where $Y'_{pred,i} = \sigma_{softmax}\left(Y_{pred,n}\right)$ is the output of nth instance, $\left(\mathrm{Y_{true,n}}\right)_\mathrm{k}$ is 1 meaning the nth instance belongs to class k and $\left(Y'_{pred,n}\right)_k$ is the kth entrance of $Y'_{pred,n}$. To minimize the loss function, gradient descent is commonly used to converge the function to a local minimum, while a global minimum of the function can be very difficult to find. The basic idea of gradient descent is to push the function for a small step at a time towards the opposite direction of the gradient at the current point to ensure the function is descending at the fastest rate. Given a fixed input dataset, the loss function L can be considered as a function of trainable weights w (Fig. 1.4), so that the gradient of L is

$$\nabla L = \left[\frac{\partial L}{\partial w_0}, \frac{\partial L}{\partial w_1}, \ldots, \frac{\partial L}{\partial w_Q}\right], \tag{1.23}$$

and change of w_q at a time

$$\Delta w_q = -\eta \frac{\partial L}{\partial w_q}, \tag{1.24}$$

where η is the learning rate which is usually a small positive constant that controls how much a step is. For example, for the network in Fig. 1.5 using cross-entropy function with softmax at the output layer, given h_{ik} as the input from node i of hidden layer and w_{ik} as the corresponding weight at the kth node of the output layer,

$$\Delta w_{ik} = -\eta \frac{\partial L_{CE}}{\partial w_{ik}} = -\eta \left[\left(Y'_{true,n}\right)_k - \left(Y_{pred,n}\right)_k\right] h_{ik}. \tag{1.25}$$

Eq. 1.25 renders the gradients for the weights at the output layer, yet the gradients at the hidden layers and the input layer remain unknown for now. Backpropagation is applied to solve the issue. If assuming there is no activation at hidden layer, given h_{ji} as the input from node j of input layer to hidden node i and w_{ji} corresponding to h_{ji} at node i, the gradient of w_{ji} is

$$\frac{\partial L_{CE}}{\partial w_{ji}} = \frac{\partial L_{CE}}{\partial h_{ik}} \frac{\partial h_{ik}}{\partial w_{ji}} = h_{ji}\left[1 - \left(Y'_{pred,n}\right)_k\right] w_{ik}. \tag{1.26}$$

For regression, one can use the L1-loss as the loss function, which is defined as

$$L_{L1} = \sum_{n=1}^{N} \left|Y_{true,n} - Y_{pred,n}\right|, \tag{1.27}$$

which is the mean absolute error between the true values and the predicted values.

In practice, trainable weights are randomly initiated, therefore, the model can be trained for multiple times so it may reach different minimums from which one run can be chosen with a better performance.

1.5.3 Validation and evaluation of performance

It is a common practice to have separate training and testing datasets in case the machine learning models are overfitted to the training data [139]. For a smaller sample size, leave-one-out validation is suitable, while for larger sample sizes, k-fold validation is more appropriate with k ranging from 4 to 10, typically. Either method is based on using only a portion of data for training and the rest for validation. For example, for k-fold validation, the whole dataset will be separated into k subsets with no overlapping. The model will be trained for k times with the kth subset chosen for validation and the rest for training. The overall performance of the model will be the average over all validation sets. Note that there is no standard for choosing the k . However, there is a trade-off between bias and variance. A larger k gives low bias of the model, as more data are used for training but also there can also be very high amounts of variance in the validation errors and long processing times [139], [140]. Obviously, when k is equal to the number of samples, k-fold becomes a leave-one-out validation. On some occasions, a third testing dataset are also separated to evaluate the model after it is trained and tuned based on k-fold validation as a final testing on the model, so that the performance evaluation is not biased towards the data being evaluated on. But for smaller sample sizes, further separating the dataset may raise the variance and lower the representing power of the model [140].

The performance of a machine learning model can be evaluated by various metrics. For binary classification, one can create a confusion matrix (as shown in Fig. 1.6) with corresponding numbers from the results on a group of samples. Many metrics can be calculated based on the confusion matrix, including accuracy as

$$ACC = \frac{TP + TN}{TP + TN + FP + FN}, \tag{1.28}$$

f1 score as

$$FS = \frac{2TP}{2TP + FP + FN} \tag{1.29}$$

which can be regarded as a harmonic mean of precision ($\frac{TP}{FP+TP}$) and recall ($\frac{TP}{TP+FN}$), Matthews correlation coefficient as

$$MCC = \frac{TP \times TN - FP \times FN}{\sqrt{(TP + FP)(TP + FN)(TN + FP)(TN + FN)}}, \tag{1.30}$$

etc. One can also draw the receiver operating characteristic (ROC) curve with recall on the x axis and FP rate ($\frac{FP}{FP+TN}$) on the y axis over a range of thresholds for classification. Typically, ROC curve starts at $(0,0)$ and ends at $(1,1)$. Area under ROC curve (AUC) can be calculated as the integration of the curve from 0 to 1. Metrics like AUC is to test if the prediction is biased towards one class when the samples are unbalanced between two classes. For regression, one can choose L1-loss, L2-loss as

$$L_{L2} = \sum_{n=1}^{N} \left(Y_{true,n} - Y_{pred,n}\right)^2, \tag{1.31}$$

or correlation-based metrics, etc., to measure the performance.

		Predicted labels	
		True	**Negative**
Actual labels	**True**	True positive (TP)	False negative (FN)
	Negative	False positive (FP)	True negative (TN)

Figure 1.7: The confusion matrix for binary classification therefore it is 2-by-2. For *K*-class classification the matrix would be *K*-by-*K*.

1.5.4 Application of machine learning in neuroimaging

Over the last two decades, there has been a wealth of studies combining neuroimaging and machine learning methods [141]. The applications of machine learning in clinical neuroimaging studies have been introduced to study numerous diseases and disorders to reveal abnormal patterns, guide diagnosis, and predict developmental outcomes [142], [143], [144]. More specifically, for neonatal brain injury, there are various applications as well. For instance, Raad et al. [145] used autoencoders to detect abnormalities on the MRI scans of infants with neonatal encephalopathy and reached over 80% of accuracy. They

also identified new abnormalities that were previously missed from the radiological readings. Pavel et al. [146] examined EEG data from infants with HIE for early prediction of development of seizures using random forest equations. Smyser et al. [147] distinguished fMRI connectivity features in preterm born infants from term born neonates using SVM. As for optical measurements, Ashoori et al. [148] extracted features from cerebral oxygen saturation measured by NIRS to predict IVH severity in preterm born neonates. In another study from Bili et al. [149], a piglet model is scanned with broadband fNIRS and diffusion correlation spectrometer to identify levels of hypoxia-ischemia (HI) insult severity, using PCA for dimension reduction and k-means clustering. Zhang et al. [132] used SVM with RSFC features to distinguish neonates with HIE from healthy newborns.

1.6 Research objectives

The general goal of this research was to determine the potential of fNIRS as a bedside neuroimaging tool for monitoring, neonatal brain activity, examine early brain injury and extend the clinical usage of fNIRS. The utility of RSFC obtained from fNIRS was examined and analyzed to characterize the injury. Specifically, there were three main objectives corresponding to Chapters 2, 3, and 4, respectively:

1. To compare RSFC patterns obtained with fNIRS from a group of preterm-born neonates with IVH with those from healthy term born neonates. It was also tested whether RSFC patterns of fNIRS could distinguish between IVH infants and healthy controls.

2. To examine whether RSFC obtained with fNIRS differed between term-born neonates with HIE. Graph theory metrics calculated from fNIRS RSFC were tested to show differences between HIE infants and controls.

3. To ascertain test whether a predictive model based on machine learning could be used to predict cortico-thalamic connectivity using cortical connectivity.

1.7 Thesis outline

This thesis has 5 chapters in total. Chapter 2 to 4 are adapted from previously published or submitted manuscripts. Chapter 5 is the final concluding chapter.

1.7.1 Chapter 2: Altered functional connectivity in preterm neonates with intraventricular hemorrhage using functional near-infrared spectroscopy

For a group of preterm born neonates with IVH, RSFC yielded from fNIRS and fMRI will be compared and the similarity will be quantified. Connectivity patterns will be compared between the IVH neonates and term-born healthy controls, and associated with severity of IVH. This chapter is adapted from the publication titled “Altered functional connectivity in preterm neonates with intraventricular hemorrhage using functional near-infrared spectroscopy” submitted to Heliyon in 2024 by Lilian M. N. Kebaya, Lingkai Tang (co-first author), Talal Altamimi, Alexandra Kowalczyk, Melab Musabi, Sriya Roychaudhuri, Homa Vahidi, Paige Meyerink, Sandrine de Ribaupierre, Soume Bhattacharya, Leandro Tristao Abi Ramia de Moraes, Keith St. Lawrence, and Emma G. Duerden and is currently under review.

1.7.2 Chapter 3: Altered resting state functional connectivity in newborns with hypoxic ischemic encephalopathy assessed using high-density functional near-infrared spectroscopy

On a group of term-born neonates with HIE, RSFC will be compared between fNIRS and fMRI. Graph theory analysis will be applied to find differences between the HIE infants and healthy controls. A machine learning based classification will be applied with RSFC features to distinguish the two groups. This chapter is adapted from the publication titled “Altered resting state functional connectivity in newborns with hypoxic ischemic encephalopathy assessed using high-density functional near-infrared spectroscopy” published in Scientific Reports in 2024 by Lingkai Tang, Lilian M. N. Kebaya, Talal Altamimi, Alexandra Kowalczyk, Melab Musabi, Sriya Roychaudhuri, Homa Vahidi,

Paige Meyerink, Sandrine de Ribaupierre, Soume Bhattacharya, Leandro Tristao Abi Ramia de Moraes, Keith St. Lawrence, and Emma G. Duerden.

1.7.3 Chapter 4: Predicting cortical-thalamic functional connectivity using functional near-infrared spectroscopy and graph convolutional networks

In this chapter, a predictive model based on graph convolutional network which is a variant of artificial neural network will be proposed and applied to predict cortico-thalamic connectivity with cortical connectivity, using data from adults and NICU neonates. This chapter is adapted from the publication titled “Predicting cortical-thalamic functional connectivity using functional near-infrared spectroscopy and graph convolutional networks” submitted to Scientific Reports in 2024 by Lingkai Tang, Lilian M. N. Kebaya, Homa Vahidi, Paige Meyerink, Sandrine de Ribaupierre, Soume Bhattacharya, Keith St. Lawrence, and Emma G. Duerden and is currently under review.

1.7.4 Chapter 5: Conclusion

In this chapter, the main goals of this thesis will be revisited and the main findings will be generalized, for each chapter and for the whole thesis. The significance of this research will be stated, and limitations reviewed. Future directions will be discussed for further developing fNIRS towards clinical application for diagnosing and monitoring early brain injury.

Chapter 2

2 Altered functional connectivity in preterm neonates with intraventricular hemorrhage using functional near-infrared spectroscopy

This chapter is adapted from the publication titled “Altered functional connectivity in preterm neonates with intraventricular hemorrhage using functional near-infrared spectroscopy” submitted to Heliyon in 2024 by Lilian M. N. Kebaya, Lingkai Tang (co-first author), Talal Altamimi, Alexandra Kowalczyk, Melab Musabi, Sriya Roychaudhuri, Homa Vahidi, Paige Meyerink, Sandrine de Ribaupierre, Soume Bhattacharya, Leandro Tristao Abi Ramia de Moraes, Keith St. Lawrence, and Emma G. Duerden and is currently under review.

2.1 Abstract

2.1.1 Background

Intraventricular hemorrhage (IVH) is a common neurological complication following very preterm birth. Resting-state functional connectivity (RSFC) using functional magnetic resonance imaging (fMRI) is associated with injury severity, yet fMRI is impractical for use in intensive care. Sensitive bedside neuroimaging biomarkers are needed to characterize injury. Functional near-infrared spectroscopy (fNIRS) measures RSFC through cerebral hemodynamics and has greater accessibility. The aims of this study were to determine the comparability of RSFC in preterm neonates with IVH using fNIRS and fMRI at term-equivalent age (TEA) and to examine fNIRS connectivity compared to healthy newborns and with IVH severity.

2.1.2 Methods

Sixteen very preterm born neonates were scanned with fMRI and fNIRS at TEA (postmenstrual age=37±0.92 weeks). Fifteen healthy newborns were scanned with fNIRS. Connectivity maps of IVH infants were compared between fNIRS and fMRI using

Euclidean and Jaccard distances. The severity of IVH in relation to fNIRS-RSFC strength was examined using generalized linear models.

2.1.3 Results

fNIRS and fMRI RSFC maps showed good correspondence. At TEA, connectivity strength was significantly lower in healthy newborns (p-value = 0.023) and preterm infants with mild IVH (p-value = 0.026) compared to infants with moderate/severe IVH.

2.1.4 Conclusions

fNIRS has potential to be a new tool for assessing brain injury and monitoring cerebral hemodynamics and a promising biomarker for IVH severity in very preterm born infants.

2.2 Introduction

Germinal matrix-intraventricular hemorrhage (GMH-IVH) continues to be a major cause of morbidity amongst neonates born premature prior to 32 weeks of gestation [5], [20], [150]. Based on the severity, GMH-IVH is classified into four grades: grade 1, hemorrhage confined to the germinal matrix; grade 2, occupying <50% of the ventricle; grade 3, distending and occupying >50% of the ventricle, and grade 4 – IVH with intraparenchymal hemorrhage [22]. GMH-IVH directly or its consequence such as post-hemorrhagic ventricular dilatation (PHVD) may lead to injury to the developing periventricular white matter that can be seen on conventional imaging at TEA [36]. Furthermore, some of these effects persist later in life, impacting language, cognitive, behavioral, and motor domains [151].

More recently, the use of RSFC revealed with fMRI has been employed to gain a better understanding of brain injury and the impact on brain function, indicating this can be a promising biomarker [121], [128], [152], [153]. The BOLD signal, measured by fMRI, captures the relative change of HbO and deoxygenated hemoglobin (HHb) induced by neuronal activation through the mechanism of neurovascular coupling [79]. Yet it is also evident that during resting state, the brain remains active, and regions with similar

functions tend to have more synchronized BOLD signals, which forms the basis for analyzing RSFC [74]. RSFC has provided new perspectives for studying brain injury in preterm infants [49], [128], [153]. fMRI-based RSFC in neonates with perinatal brain injury was predictive of motor skills at 8 months of age [154]. Yet, the clinical utility of functional MRI is limited due to its accessibility. MRI may be impractical for some neonates with IVH who cannot be transported away from the NICU.

Functional connectivity determined from fMRI shows signal alterations based on BOLD signal and is more reflective of HHb [155]. Functional NIRS is a non-invasive and light-based brain imaging technique that can be used to map functional connectivity at the bedside. fNIRS also exploits the process of neurovascular coupling and measures the absorption of near-infrared light by hemoglobin [152]. Hence, oxygenation of the cerebral cortex is derived as an indirect measurement of neural activity. Both indices reflective of cerebral oxygenation, HHb and HbO along with total hemoglobin can be estimated using fNIRS. fNIRS is an extremely convenient neuromonitoring tool, that can be acquired at the bedside, within a short time period with minimal inconvenience to fragile neonates.

GMH-IVH, regardless of grade, has been associated with disrupted functional connectivity in neonates [156], [157], [158]. RSFC has been demonstrated to be associated with ventricular volumes in very preterm born neonates with PHVD [158], indicating that this method can reliably be used at the bedside in the NICU. Given the strong need for bedside tools to monitor injury patterns in very preterm born neonates and evidence suggesting that fNIRS-based RSFC is comparable to fMRI in adults [107], we sought to compare the RSFC maps acquired using fNIRS and fMRI in very preterm neonates with IVH who were assessed at TEA. We also aimed to investigate whether fNIRS-based RSFC in preterm infants would be associated with the severity of IVH, compared to healthy term-born neonates. Our overall hypothesis was that fNIRS-based measures of RSFC would be comparable to that obtained with fMRI and that severity of injury would be associated with changes in RSFC patterns.

2.3 Methods

2.3.1 Study design and settings

This was a prospective observational cohort study. Study participants were recruited from the NICU at the London Health Sciences Centre (LHSC), London, Canada between January 2020, and December 2022.

2.3.2 Participants

Preterm neonates were eligible for inclusion based on the following criteria: ≤ 32 weeks' gestational age (GA), born at, or referred to NICU, and admitted with a diagnosis of GMH-IVH, made by the most responsible physician on the infant's first routine cranial ultrasound. Exclusion criteria were the following: major anomalies of the brain or other organs, congenital infections, intrauterine growth restriction, metabolic disorder, and ultrasound evidence of a large parenchymal haemorrhagic infarction. Term-born infants with no reported brain injury were recruited as healthy controls. Participants were recruited from the LHSC Mother baby Care Unit (MBCU). Inclusion criteria were birth >36 weeks' GA, born at LHSC, and admitted to MBCU. Exclusion criteria were the following: congenital malformation or syndrome, antenatal infections, antenatal exposure to illicit drugs, small for gestational age and intrauterine growth restriction.

The study was approved by the Health Sciences Research Ethics Board at Western University (116142). Informed consent was provided by the parents/caregivers of the infants enrolled in the study. The study was conducted in accordance with the Declaration of Helsinki.

2.3.3 Clinical variables

The neonatal charts were reviewed by Neonatal-Perinatal Medicine Fellows (LMNK, TA, SR, MM), Paediatric Resident (AK), Research Associate (HV) or NICU Nurses (PM, CM) for demographic and clinical characteristics. The following postnatal events were included: days of mechanical ventilation, bronchopulmonary dysplasia, patent ductus arteriosus

requiring treatment, days of parenteral nutrition, culture proven sepsis, necrotizing enterocolitis.

2.3.4 MRI acquisition & image analysis

Anatomical and functional MRI images were acquired on a 1.5 T GE scanner at LHSC. Each infant underwent a clinical MRI scan consisting of a whole-brain T1-weighted structural image (TR=8.4–11.5 ms [depending on clinical requirements], TE=4.2 ms, flip angle=12/25°, matrix size 512 × 512, 99–268 slices, voxel size typically 0.39 × 0.39 × 0.5 mm (0.31 × 31 × 5 to 0.43 × 0.43 × 0.6 for some infants), and a T2-weighted structural image (TR=3517–9832 ms, TE=7.3–8.4 ms, flip angle = 90/160°, matrix size 256 × 256, 19–60 slices, 0.7 × 0.7 × 2–5 mm voxel resolution). BOLD fMRI data were acquired using an echo planar imaging sequence to examine resting-state functional connectivity (TR=3000ms, TE=50 ms, flip angle=70°, matrix size 64 × 64, 39 slices, voxel size 3 x 3 x 3 mm, total volumes 35).

Preprocessing of fMRI images was conducted with FMRIB Software Library (https://fsl.fmrib.ox.ac.uk/fsl/fslwiki/FSL). The pipeline included brain extraction, motion correction, spatial smoothing (full width at half maximum = 5 mm), band-pass filtering (0.01-0.1 Hz) and registration to a neonatal atlas [159]. Average BOLD sequences were extracted from frontal, parietal, temporal and occipital lobes of both hemispheres, and then correlated to build an 8-by-8 lobe-wise RSFC map for each infant.

2.3.5 Brain injury characterization

A Neuroradiology Fellow (LTARdM) scored the T1-weighted anatomical images for brain injury severity. These were verified by a Paediatric Neuroradiologist. IVH was graded (mild=1-2, and moderate-severe=3-4) using Papile's method [22].

2.3.6 fNIRS acquisition & analysis

All participants (preterm infants with IVH and healthy newborns) were scanned with a NIRSport2 (NIRx, Berlin, Germany) unit with two emission wavelengths (760 and 850 nm). We used an 8-by-8 set up with 20 channels covering the whole brain, and a sampling

rate of 10 Hz. For each hemisphere, there were 4 channels on the temporal, 2 on the parietal, frontal and occipital lobes. On average, scans lasted 487.46 seconds (with a standard deviation of 116.17 seconds) across all participants. For each infant, a 6-minute segment of high-quality data, determined through visual inspection, was selected for further analysis.

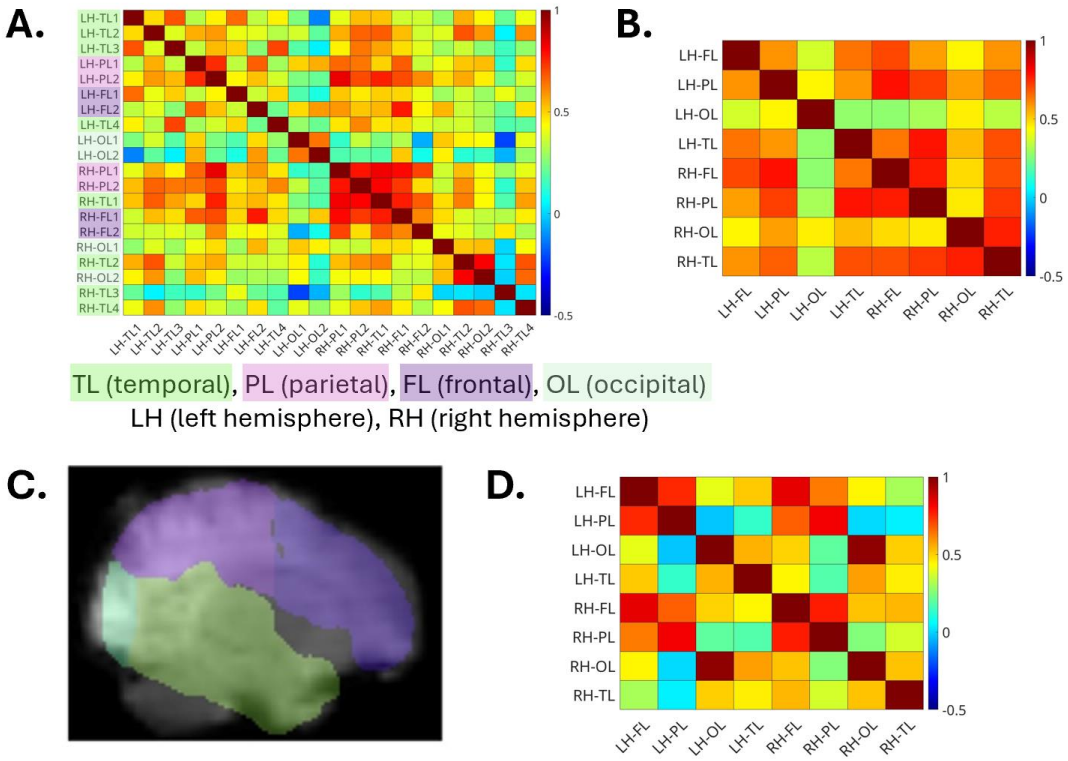

Figure 2.1: Examples of (A) a 20-by-20 connectivity map and (B) an 8-by-8 map for the signals extracted from the fNIRS channels in the left and right hemispheres from the temporal, parietal, frontal and occipital lobes. The 8-by-8 map was obtained by averaging fNIRS signals from one lobe then correlating them with each other. (C) Lobe-based analysis of the fMRI data. A hemisphere was sectioned into temporal, parietal, frontal and occipital lobes. (D) Based on the section, a connectivity map was built from the fMRI image using averaged BOLD series from each region. All figures were obtained from the same participant of the IVH group. Colorbars indicate the value of Pearson correlation.

After data acquisition, for fNIRS recording of each infant, visual inspection was done to select a 6-minute segment with fewer motion artifacts and less white noise. A preprocessing pipeline, built within Homer 3 software, including spline interpolation for motion correction [65], Savitzky–Golay filtering with frame size of 10 [66], band-pass filtering of 0.01-0.1 Hz and modified Beer-Lamber law to convert optical density to concentration change of HbO and HHb, respectively [58]. Pearson correlation was used to calculate connectivity. To compare RSFC maps between fNIRS and fMRI, channels corresponding to one lobe were averaged then correlated with other cortices to create an 8-by-8 lobe-wise connectivity maps for HbO and HHb, respectively (Fig. 2.1B,C,D). For lobe-wise maps of both fNIRS and fMRI, nodes were lobes and edges were weighted by Pearson correlation coefficients between sequences of the two lobes. 20-by-20 channel-wise RSFC maps were also calculated for fNIRS (Fig. 2.1A), yet in this map, nodes were fNIRS channels.

2.3.7 Statistical analysis

Statistical analyses were performed using a combination of Matlab (R2020b, Natick, Massachusetts: The MathWorks Inc) and Statistical Package for the Social Sciences (v.29, Chicago, IL).

To address our first aim, whether the RSFC maps rendered from the fNIRS and fMRI modalities were comparable, we calculated the Euclidean distances and Jaccard distances between the two lobe-wise maps at various levels of sparsity for each participant and for both weighted and binarized maps [160]. Both weighted and binarized maps were analyzed here because there was no indication on which one was preferred from previous studies. Both types showed various strengths in preserving topology of a map [161]. The sparsity was the percentage of non-zero connections in a RSFC map after all negative-weighted and some low-weighted connections were removed (set to zero). Sparsifying the maps has become widely accepted as negative connections are still under debate for their biological interpretations and low-weighted connections can result from noise [110], [162]. A common practice is to start from removing the lowest weighted connections, including negative ones, then continuing to remove the lowest weighted ones until the sparsity

reaches a desired percentage. Weighted maps were obtained in this way. Binarized maps were then calculated with non-zero connections set to 1. In general, there is no standard for choosing the sparsity [163], therefore, the range 0.2-0.4 was tested in this study. With sparsity of 0.4, negative connections were removed. And with 0.2, the maps became sparser but could still stay connected while a representational number of connections remained, as the maps were only 8-by-8. Given maps $G_{fMRI}(V, E_{fMRI})$ and $G_{fNIRS}(V, E_{fNIRS})$ obtained from the two modalities, where V and E denote node and connection set, respectively, and their adjacency matrices $A_{fMRI} = [a_{ij}^{fMRI}]$ and $A_{fNIRS} = [a_{ij}^{fNIRS}]$, respectively, where i and j are nodes, Euclidean distance between two maps was defined as

$$d_E = \sqrt{\sum_{i,j} \left(a_{ij}^{fMRI} - a_{ij}^{fNIRS}\right)^2}. \tag{2.1}$$

Jaccard distance for weighted maps was defined as

$$d_{Jw} = 1 - J_w,$$
$$where\ J_w = \begin{cases} \dfrac{\sum_{i,j} min\left(a_{ij}^{fNIRS}, a_{ij}^{fMRI}\right)}{\sum_{i,j} max\left(a_{ij}^{fNIRS}, a_{ij}^{fMRI}\right)}, if \sum_{i,j} max\left(a_{ij}^{fNIRS}, a_{ij}^{fMRI}\right) > 0 \\ 1, \quad otherwise \end{cases} \tag{2.2}$$

while for binarized maps, Jaccard distance was defined as

$$d_{Jb} = 1 - \frac{|E_{fNIRS} \cap E_{fMRI}|}{|E_{fNIRS} \cup E_{fMRI}|}. \tag{2.3}$$

One level of sparsity yielding the most similarity between two modalities was picked for following analyses. Based on this specific sparsity, we also calculated similarity maps for weighted and binarized RSFC maps. Similarity map was defined as

$$S = [s_{ij}], where\ s_{ij} = 1 - \frac{1}{N}\sum_{n=1}^{N} \left|a_{ij}^{fNIRS,n} - a_{ij}^{fMRI,n}\right|, \tag{2.4}$$

where $a_{ij}^{fNIRS,n}$ and $a_{ij}^{fMRI,n}$ are entries of individual adjacency matrices of n^{th} subject from a total of N. Note that for weighted RSFC maps, s_{ij} was an index based on Euclidean distance, while for binarized maps, s_{ij} equals to the percentage of subjects sharing the connection.

We addressed our second aim, concerning whether fNIRS-based RSFC would predict IVH severity in very preterm born neonates compared to healthy newborns, in generalized linear models, which is more interpretable clinically with the β values. Based on the connectivity maps at the sparsity level yielding the most similarity between fNIRS and fMRI, two generalized linear models were tested to associate IVH severity and RSFC strength. In the first model, the summation of all weighted connectivity values of the whole brain for HHb were entered as the dependent variable, with IVH grade (none [healthy newborns], mild, moderate-severe) as a factor, adjusting for biological sex, GA, and postmenstrual age (PMA) at scan. In the second model, HbO connectivity values were entered as the dependent variable, using the identical independent variables as in the first model. It was assumed the connectivity followed Gaussian distribution, and the tests among groups were corrected using the Bonferroni correction method.

2.4 Results

2.4.1 Participants

Sixteen very preterm born neonates with GMH-IVH were enrolled (GA at birth = 26.28±2.82 weeks). All preterm infants underwent MRI scanning at TEA (GA at scan = 37.04±0.96 weeks). In eleven participants, fNIRS was also acquired. A total of 15 term-born infants were recruited from the LHSC MBCU with mean birth GA of 38.92±1.30 weeks and fNIRS scans performed within 48 hours of life. None of the healthy newborns underwent MRI. Detailed demographics of participants can be found in Table 2.1. Clinical variables of the IVH group can be found in Table 2.2. Most of the infants were scanned during natural sleep for the fNIRS and fMRI scans. The IVH infants were in the incubators during fNIRS scans and healthy newborns were not controlled for this condition, i.e., some of them were held by caregivers.

Table 2.1: Participant demographics

	Neonates with IVH	**Healthy Newborns**
n	16	15

Male sex	12	6
Birth GA (SD) (weeks)	26.1(2.8)	38.9(1.3)
PMA at scan (SD) (weeks)	36.9(0.9)	38.9(1.3)
IVH severity		
mild	7	-
moderate/severe	9	-

Note: Values represents counts for categorical variables and means for continuous variables.

Table 2.2: Clinical variables of the IVH group

Bronchopulmonary dysplasia [%]	**Necrotizing enterocolitis [%]**	**Days of mechanical ventilation (SD)**	**Patent ductus arteriosus [%]**	**Early parenteral nutrition (within 4 weeks of life) [%]**
13 [81]	2 [12]	25.1 (18.4)	13 [81]	16 [100]

2.4.2 Comparing fNIRS and fMRI

Lobe-wise connectivity maps were obtained from fNIRS for both HbO and HHb. The fNIRS maps were then compared against fMRI RSFC maps at various levels of sparsity using metrices of Euclidean and Jaccard distances. Only large- and positive-weighted connections were kept when achieving a certain level of sparsity. Sparsity ranged from 0.2 to 0.4. At 38% of sparsity, for both weighted and binarized maps, for both HbO and HHb maps, least Euclidean and Jaccard distances were achieved (i.e., the fNIRS and fMRI yielded most similar RSFC maps, Fig. 2.2). Therefore, in the subsequent analyses, this level of sparsity was applied.

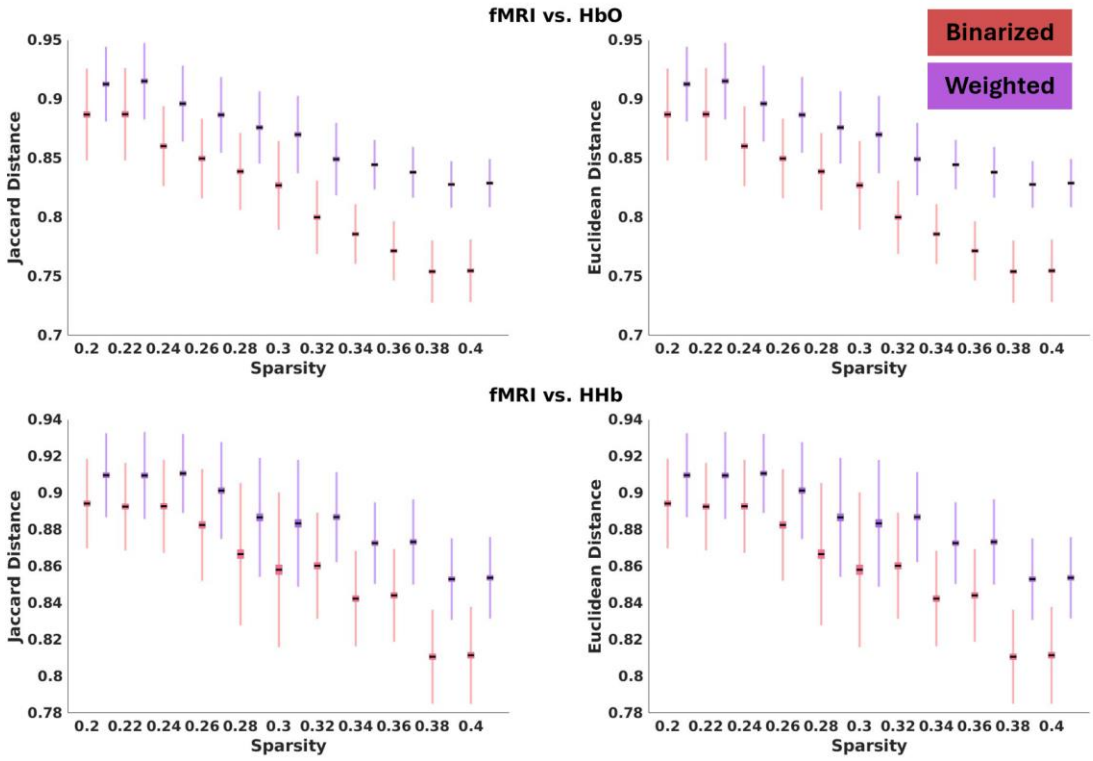

Figure 2.2: Similarity of RSFC maps between fNIRS and fMRI with sparsity, measured by Euclidean distance and Jaccard distance on weighted and binarized maps, respectively. Means and confidence intervals (CI) were estimated using a bootstrapping method. If the sparsity is near 0, the distances will also be close to 0. For sparsity values between 0.4 and 1, distances may fluctuate if all connections are positive. However, in practice, there are often negative connections, which we have not addressed due to uncertainties in their interpretation.

Based on the sparsity of 38%, the similarity maps were calculated comparing every connection between fNIRS and fMRI. Similarity maps of HbO against fMRI and HHb against fMRI had good correspondence for both weighted and binarized cases (Fig. 2.3). This is largely a reflection of the anti-correlation between the two chromophores, yielding similar RSFC maps. Also, most connections demonstrating high correspondence were interhemispheric.

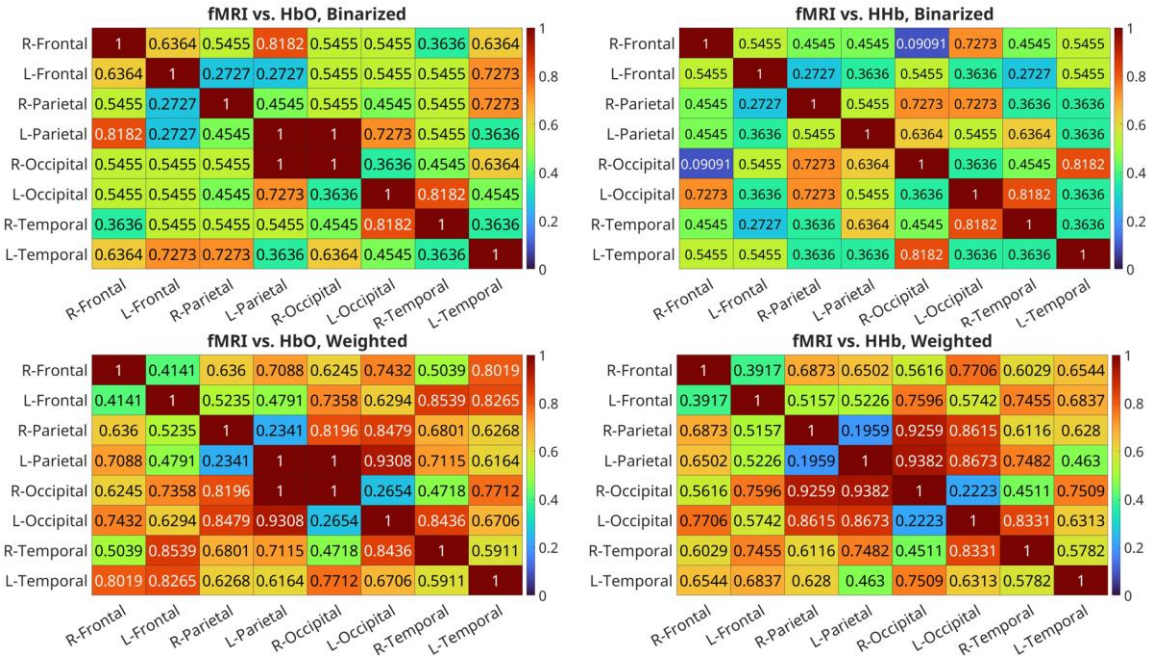

Figure 2.3: Lobe-wise similarity maps at sparsity of 38%. Higher values reflect greater similarity between the two modalities. Average values among channels are 0.55 (upper left, standard deviation [SD]: 0.16, CI: 0.48-0.61), 0.66 (lower left, SD: 0.18, CI: 0.59-0.73), 0.49 (upper right, SD: 0.16, CI: 0.43-0.55) and 0.63 (lower right, SD: 0.19, CI: 0.56-0.71).

2.4.3 Connectivity and severity of IVH

In a generalized linear model, the functional connectivity within the cortical network was examined in relation to IVH severity (none [healthy newborns], mild IVH, moderate/severe IVH). The weighted connectivity values for HHb were significantly lower in healthy newborns (B= -53.5, 95%, CI -94.61 - -12.39, p=0.011, Table 2.3, Fig. 2.4), and preterm neonates with mild IVH (B=-24.7, 95%, CI -42.7- -6.7, p=0.007) compared to preterms with moderate/severe IVH adjusting for birth GA, sex, and PMA at scan. No significant differences in HHb connectivity values were evident between the healthy newborns and very preterm born neonates with mild IVH (p=0.5, Bonferroni corrected for multiple comparisons). Similar results were found when examining HbO in a separate GLM, whereby healthy newborns (B=-42.6, 95%, CI -79.1- -6.0, p=0.023, Table 2.3, Fig. 2.4) and very preterm neonates with mild IVH (B=-18.2, 95%, CI -34.3- -2.2, p=0.026)

compared to very preterm born neonates with moderate/severe IVH. No differences were evident between the HbO sparsity values for healthy newborns and neonates with mild IVH (p=0.6, Bonferroni corrected for multiple comparisons). Similar analysis was done for fMRI data as well, with lobule-wise averaged BOLD signals for developing RSFC maps, yet we found no significant difference (p>0.05) on connectivity strength between mild and moderate/severe groups.

Table 2.3: Results of a generalized linear model examining HHb and HbO connectivity relative to IVH severity

	95% Confidence Intervals							
	HHb				HbO			
	B	**Upper**	**Lower**	**p value**	**B**	**Upper**	**Lower**	**p value**
Birth GA	3.2	0.19	6.22	0.038[b]	2.5	0.23	5.14	0.074
PMA at scan	-2.3	-7.93	3.42	0.436	-0.4	-5.49	4.61	0.865
Male sex	-1.0	-15.18	13.22	0.892	-1.6	-14.19	11.08	0.810
Injury severity								
Healthy newborn	-53.5	-94.61	-12.39	0.011[b]	-42.6	-79.15	-5.98	0.023[b]
Mild IVH	-24.7	-42.72	-6.72	0.007[a]	-18.2	-34.27	-2.23	0.026[b]
Moderate/severe IVH	ref	-	-	-	ref	-	-	-

[a]Statistically significant, $p < 0.01$. [b]Statistically significant, $p < 0.05$.

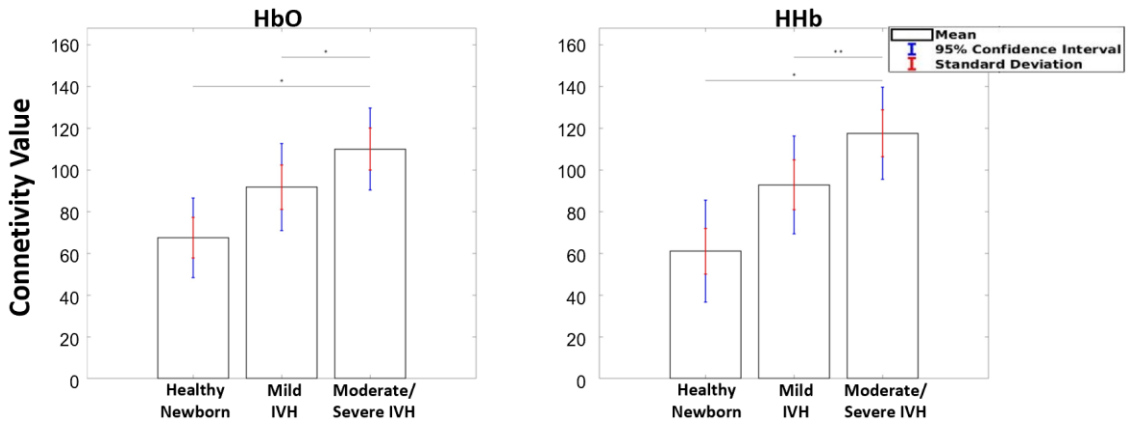

Figure 2.4: Very preterm born neonates scanned at term-equivalent age showed increased HbO (left) and HHb (right) connectivity values relative to healthy newborns and neonates with mild IVH. **p<0.01, * p<0.05.

2.5 Discussion

In a prospective cohort of very preterm born infants with IVH, we examined the predictive utility of fNIRS connectivity in assessing brain health. As expected, RSFC maps were comparable between fMRI and fNIRS in the very preterm born infants with IVH. Findings indicate that fNIRS can be used to study cortical RSFC at the bedside. We further examined whether the severity of injury could be predicted by functional connectivity metrics. We found that for both HHb and HbO, the connectivity values at TEA were increased in infants with moderate/severe IVH relative to healthy newborns and very preterm born infants with mild IVH. Overall, our results highlight the use of fNIRS as a bedside monitoring tool to examine brain-health metrics in very preterm born infants impacted by IVH.

In the first aim, we saw good correspondence of the RSFC maps (HbO vs fMRI and HHb vs fMRI) between the two imaging modalities. Our findings are consistent with other studies. Duan et al., using fNIRS and fMRI data acquired from 21 adult subjects during resting state, demonstrated good correspondence between the two imaging modalities [107]. In another adult study, Sasai et al. also reported that fNIRS HbO and fMRI BOLD maps had a significant positive correlation for all brain regions investigated [106]. We were able to demonstrate similar results in our infant population. Second, except for the occipital region, the other regions (frontal, parietal and temporal) showed high similarity of RSFC

maps between the two imaging modalities. The discrepancy in the occipital region could be because of measurement errors, including thick hair, poor contact between optodes and scalp, cap fit, which are common in fNIRS studies in infants [152], [155], [164]. In addition, all our bedside fNIRS measurements were carried out with the infants laying supine in their cot or caregivers' arms which could explain the poor optode contact in the occipital region. Overall, our study adds to the body of literature showing that fNIRS indeed provides comparable RSFC measures to fMRI. This is especially important given the bedside availability of fNIRS for the vulnerable NICU population.

RSFC of fMRI BOLD was compared to HbO and HHb maps, respectively. It is commonly considered that HHb is more similar to BOLD since the biophysical basis of fMRI relies on the magnetic properties of deoxygenated hemoglobin [165], yet in our comparisons, we showed that HbO RSFC was closer to fMRI with lower between-modality distances at various sparsity levels (Fig. 2.2) and higher averaged similarity (Fig. 2.3). Previous studies also gave inconsistent findings on this issue. Toronov et al. showed BOLD of motor cortex was more correlated with HHb than HbO [166], yet the same group later found that spatial localization of visual networks was more consistent between HbO and BOLD [51]. In terms of RSFC, Duan et al. reported higher correlations between BOLD and HbO compared to HHb [107], and they mentioned possible reason that HbO had higher signal-to-noise ratio than HHb [167], and higher reliability of detecting RSFC [168]. Yet it was also pointed out by Abdalmalak et al. that HbO was more sensitive to systemic physiology than HHb [169]. Further analysis on whether HbO or HHb is more representational to true RSFC would be appreciated.

Filtering connections that are either negative- or low-weighted is a common practice for RSFC research [170]. RSFC yielded from a series of sparsity levels were tested in previous studies, that demonstrated inconsistency among the results [171], [172], [173]. Recent studies have highlighted the necessity of choosing the proper sparsity value and have introduced various strategies [174], [175]. In the current work, we have addressed this issue by identifying a maximal similarity value for two imaging modalities (i.e., fNIRS and fMRI). For future research in fNIRS RSFC, this method may be impractical without access to another imaging modality such as fMRI. Yet, potentially this challenge can be overcome

through scanning larger number of neonates, as this will aid in identifying a sparsity level that could be more universally appliable for neonatal RSFC studies.

Compared with their healthy counterparts, we found increased RSFC at TEA among infants with IVH, regardless of the severity. This was an unexpected finding, as most studies of very preterm infants with IVH have demonstrated reduced RSFC at TEA [156], [157], [176]. Reduced RSFC, especially in higher grades of IVH injury is attributed to disruptions to the periventricular white matter. However, some studies have also shown intact RSFC in infants with IVH [177]. The results from our study, while different from what is previously known in literature, could be explained by several plausible mechanisms. First, our study population was very preterm (mean GA 26.28 ± 2.82), with IVH already evident within the first week of life and our findings represent the RSFC 10-12 weeks post IVH. Thereafter, during their NICU stay and with ongoing surveillance, depending on the IVH severity, some of the study participants underwent neurosurgical interventions to divert cerebrospinal fluid. In tandem with the above-mentioned, over time the neonatal brain undergoes massive growth and reorganization, demonstrating a mature architecture by TEA [178], [179]. Moreover, some case studies have shown neural plasticity in infants with high grade IVH [180]. The immaturity of neurovascular coupling mechanisms could have influenced the increased connectivity seen in the IVH group. It was previously reported in animal models that newborns showed globally correlated hemodynamic fluctuations during resting state [109], likely due to the absence of hyperemia, which is typically present in adults in response to neuronal activity. Also, preterm neonates with IVH, compared to those without, lack vascular responses needed for the compensation of increased metabolism after neuronal activation [181]. Therefore, the IVH group could be also expected to have even lower hemodynamic responses than healthy term newborns, which may have led to less distinction among brain regions rather than reflect increased connectivity. Hence, all these factors could explain our findings. These questions are best addressed in longitudinal studies, correlating RSFC with neurodevelopmental outcomes. Disruptions in neonatal functional connectivity in children with perinatal brain injury have been associated with developmental outcomes, and in turn better characterization of these patterns is needed to improve early care practices [154]. In addition, we found no

significant differences of connectivity strength on our fMRI dataset between mild and moderate/severe groups. This could have resulted from some IVH participants and all controls having no fMRI scans. Another possible explanation is that fNIRS recordings were from more localized positions instead of whole lobules as in fMRI, i.e., some within-lobule disruptions could be overlooked by averaging the lobules. Also, level of localization (e.g., from voxel to anatomical regions) has been shown to have significant impact on network properties of RSFC [182], [183].

Our study has several strengths, namely, both groups (infants with IVH and healthy controls) were recruited from and assessed at the same centre, using the same high-density fNIRS system and at similar postmenstrual ages. The above-mentioned measures ensure uniformity and eliminate potential bias. Second, compared to the clinical NIRS system that is now commonly used in most level III NICUs, high density fNIRS systems provide whole brain coverage and connectivity. Our study population (infants with IVH and healthy controls) was also well characterized. There are also some challenges and limitations that were associated with our study. Primarily, the sample size for our study population was small. This was due to difficulty acquiring excellent quality data, which is a challenge for fNIRS [164]. These challenges could potentially be addressed through the development of hardware specifically designed for neonates. Appropriate and effective hardware may also promote greater use in NICU-settings. Also, our eventual goal is to use fNIRS for clinical decision making in individual neonates at the bedside. Despite some signals of poor quality, we were still able to show comparable fNIRS and fMRI connectivity maps and discriminative fNIRS features for separating the groups. Second, more males than females were recruited, due to lack of competitive enrolment. However, sex differences were not evident in any analyses. Thirdly, including a group of preterm infants without brain injuries would enhance the study by clarifying the association between altered connectivity and brain injury. Previous research indicates that preterm newborns without known brain injuries can also display altered connectivity [184], [185]. Another limitation is that the positions of fNIRS optodes cannot be precisely located in MRI space, therefore, we cannot do more localized analysis on similarity between the two modalities and how severity of IVH affecting RSFCs of the two. As a compromise, we could only use the approximate lobules that covered the fNIRS channels. In addition, some potential covariates were not

analyzed (e.g., clinical variables, whether the neonates were scanned in incubators or caregivers' arms). Calculating an appropriate sample size would enhance the statistical robustness of the results. However, estimating the effect size could be challenging as the data were not normalized. Finally, though the classic Papile's method [22] for grading IVH was used for our population, it is acknowledged that there is a new and more detailed descriptive method for GMH-IVH categorization, with GMH localized and periventricular hemorrhagic infarction separately noted [186]. Despite the limitations, we believe that fNIRS offers promising avenues that can impact clinical care of infants with IVH. Larger prospective studies are needed to address these challenges.

2.6 Conclusions

In a heterogenous cohort of very preterm born neonates with IVH who underwent fNIRS and fMRI we report comparable RSFC maps between the two modalities. Findings indicate that in a small sample of neonates that bedside fNIRS can produce comparable results to that of fMRI. Secondly, fNIRS revealed distinct RSFC patterns between preterm infants with IVH at TEA and healthy infants. Larger prospective studies are needed to better characterize fNIRS-based functional connectivity changes over time and whether they are predictive of functional outcomes.

Chapter 3

3 Altered resting state functional connectivity in newborns with hypoxic ischemic encephalopathy assessed using high-density functional near-infrared spectroscopy

This chapter has been adapted from the publication entitled “Altered resting state functional connectivity in newborns with hypoxic ischemic encephalopathy assessed using high-density functional near-infrared spectroscopy” published in Scientific Reports in 2024 by Lingkai Tang, Lilian M. N. Kebaya, Talal Altamimi, Alexandra Kowalczyk, Melab Musabi, Sriya Roychaudhuri, Homa Vahidi, Paige Meyerink, Sandrine de Ribaupierre, Soume Bhattacharya, Leandro Tristao Abi Ramia de Moraes, Keith St. Lawrence, and Emma G. Duerden.

3.1 Abstract

Hypoxic-ischemic encephalopathy (HIE) results from a lack of oxygen to the brain during the perinatal period. HIE can lead to mortality and various acute and long-term morbidities. Improved bedside monitoring methods are needed to identify biomarkers of brain health. Functional near-infrared spectroscopy (fNIRS) can assess resting state functional connectivity (RSFC) at the bedside. We acquired resting-state fNIRS data from 21 neonates with HIE (postmenstrual age [PMA]=39.59), in 19 neonates the scans were acquired post-therapeutic hypothermia (TH), and 20 term-born healthy newborns (PMA=39.95). Twelve HIE neonates also underwent resting-state functional magnetic resonance imaging (fMRI) post-TH. RSFC was calculated as correlation coefficients amongst the time courses for fNIRS and fMRI data, respectively. We showed that the fNIRS and fMRI RSFC maps were comparable. RSFC patterns were then measured with graph theory metrics and compared between HIE infants and healthy controls. HIE newborns showed significantly increased clustering coefficients, network efficiency and modularity compared to controls. Using a support vector machine algorithm, RSFC features demonstrated good performance in classifying the HIE and healthy newborns in separate groups. Our results indicate the utility of fNIRS-connectivity patterns as potential biomarkers for HIE and fNIRS as a new bedside tool for newborns with HIE.

3.2 Introduction

HIE results from insufficient cerebral oxygen delivery and disrupted blood supply during the prenatal, intrapartum, or postnatal periods [16]. HIE occurs in 1 to 2 per 1000 live births in developed countries [3]. HIE is one of the most serious birth complications affecting term-born neonates and a major cause of death and long-term disabilities, including cerebral palsy, epilepsy and impairments of various cognitive functions [13], [14]. Neonates with HIE are typically identified shortly after birth and deteriorate within the first days of life [16]. Therefore, early diagnosis and monitoring are key for TH, which is the standard treatment for moderate to severe HIE [187].

With high spatial resolution, magnetic resonance imaging (MRI) is widely considered the gold standard for diagnosing and characterizing neurological disorders and brain injuries, including HIE [19]. However, MRI is limited by its accessibility within the neonatal intensive care unit (NICU) and sensitivity to movements, requiring imaging preferably when neonates are either asleep or sedated. Cerebral monitoring is also commonly practiced, especially during TH. Electroencephalography (EEG) based modalities are used for detecting seizures; however, they may not provide all the necessary physiological information for a continuous assessment, considering that HIE injuries are closely related to cerebral oxygenation and oxidative metabolism [16], [155]. NIRS has been used to examine cerebral hemodynamics and oxygenation changes during the pre-TH period, as well as during and after rewarming[188]. In the first 6 hours of life following injury due to hypoxia-ischemia (HI), cerebral oxygenation decreases but recovers by 18 to 20 hours of life. Cerebral oxygenation changes are predictive of brain injury in this population [189]. Increased cerebral oxygenation during 24 to 36 hours of life significantly increased the likelihood of developing brain injury [190]. Increases in cerebral oxygenation may reflect mitochondrial changes due to decreased oxygen utilization. Cerebral perfusion may exceed metabolism demands reflected in increased cerebral oxygenation.

RSFC offers new perspectives for examining early brain injuries. RSFC, typically derived from fMRI images, explores the functional synchronization among brain regions and reveals the organization of brain networks, for adults and infants [98], [179], [191], [192].

RSFC has been widely introduced to study prematurity and early brain injuries [50]. Chiarelli et al. used multivariate analysis to find spatially diffused alterations of RSFC on neonatal cortices [193]. In preterm-born neonates with post-hemorrhagic infarction, reduced functional connectivity (FC) was reported [128]. In another cohort of preterm-born neonates with periventricular hemorrhage, reduced connectivity within the motor networks was also reported [194]. In newborns with HIE, functional networks have been explored with reported reduced inter- and intra-hemispheric connectivity strength [130], particularly in primary motor regions [131]. Also, functional connectivity and graph-theory measurements were positively associated with developmental outcomes [12].

Functional NIRS, similar to fMRI, can also yield cerebral RSFC for neonates. However, fNIRS is more accessible for the NICU population and insensitive to head motion. fNIRS measures the amount of near-infrared light absorbed by hemoglobin, which is converted into concentration changes of oxygenated and deoxygenated hemoglobin (HbO and Hbr), as an indirect measurement of neural activity [195]. RSFC derived from fNIRS and fMRI is comparable in several studies on adults [107] and a month-old infant [108]. Less is known about the comparability between fNIRS and fMRI in the newborn period. Considering the rapid growth and maturation of the brain during the early months of life [196], the penetration depth of fNIRS can vary, i.e., portions of white and grey matter covered by near-infrared light can be different during early development of the brain. As the key modulator of penetration depth, an optimal source-detector distance for infants is still being discussed [197]. Since fMRI RSFC is largely based on grey matter, RSFC of fNIRS may differ from fMRI in newborns.

fNIRS RSFC has also been examined in previous studies with critically ill neonates to determine whether this analytic method can be used as a biomarker for brain health. In preterm-born neonates, altered FC was reported at term equivalent age compared to term-born neonates [126]. Lower FC on short-range and inter-hemispheric connections has also been reported in the preterm population [198], associated with brain injury and larger ventricular volumes [158]. Few studies to date have examined RSFC using fNIRS to examine the impact of brain injuries after term birth. Zhang et al. [132] reported, in a small sample of newborns with HIE (n=13), who were examined with fNIRS in the pre-TH

period, that decreased RSFC patterns compared to a comparable number of healthy newborns. Reduced long-range connectivity was reported in the HIE cohort. Graph theory measures applied to the data indicated that newborns with HIE had an increased ability for local information transmission, reflected in higher local network efficiency. The findings could reflect compensation mechanisms. Further, graph theory-based measures such as small-worldness effectively distinguish HIE and healthy newborns. This study provided key evidence for altered FC at baseline before TH was initiated in the HIE population.

The short-term effects of the injury associated with HI in newborns remain poorly understood. fNIRS-based RSFC is a promising avenue for biomarker identification in this vulnerable population. In the current work, we examined fNIRS-based RSFC in newborns with HIE, of whom the majority were assessed post-TH after rewarming. Our central hypothesis was that fNIRS-based RSFC would be decreased in newborns with HIE and that graph theory-based measures of these metrics would be viable metrics for classifying these newborns. Our first aim was to compare patterns of RSFC obtained using fNIRS and fMRI to determine whether similar findings would be obtained between the two modalities. As part of a subaim, we further examined FC obtained using both fNIRS and fMRI in relation to structural MRI-based volumes of grey and white matter as additional markers of brain health. The second aim of our study was to compare fNIRS-based RSFC between term-born neonates with HIE and healthy controls. We subsequently examined whether graph theory-based metrics would serve as useful indicators of an HIE diagnosis. Using a support vector machine model applied to the HIE and healthy newborn data, we determined whether graph theory measures would predict diagnostic group membership.

3.3 Methods

3.3.1 Participants

This study was conducted as part of an ongoing study investigating brain injury in critically born neonates. Participants were recruited between April 2021 and August 2022. Participants with HIE were recruited from the NICU at the Children's Hospital of South Western Ontario, London, Canada. Eligibility criteria for the patients with HIE included:

HIE diagnosis, gestational age ≥ 36 weeks, birth weight≥ 2000 g. HIE diagnosis was based on a cord gas pH of ≤7.0 and/or base deficit of ≥16 mmol per L; if pH was between 7.01 and 7.15 or a base deficit was between 10 and 15.9 mmol per L, additional history of an acute perinatal event and an APGAR score at 10 minutes of ≤5, or need for assisted ventilation/resuscitation at birth, and the presence of seizures or evidence of moderate or severe encephalopathy based on a standardized neurological examination [34]. We excluded neonates if they had evidence of major anomalies of the brain or other organs, congenital infections (e.g., TORCH), intrauterine growth restriction (IUGR), identifiable metabolic disorder or ultrasound evidence of a large parenchymal hemorrhagic infarction.

Term-born healthy newborns with no reported brain injury were also recruited to the study from the Mother Baby Care Unit (MBCU). Inclusion criteria were admission to the MBCU, birth >36 weeks' GA, and inborn. Exclusion criteria were evidence of congenital malformation or syndrome, antenatal infections, antenatal exposure to illicit drugs, small for gestational age (SGA) and IUGR.

The study was approved by the Health Sciences Research Ethics Board at Western University. Informed consent was provided by the parents/caregivers of the newborns. The study was conducted in accordance with the Declaration of Helsinki.

3.3.2 Clinical and Demographic Variables

Maternal and newborn health data were extracted from electronic medical records by a Paediatric Nurse, Paediatric Resident or NICU Fellow. For participants with HIE, the demographic data extracted included gestational age, birth weight, biological sex, HIE stage (based on Sarnat staging [32]), resuscitation details, Apgar scores and cord pH. We also collected the following data: 72 h treatment with TH, the presence of brain injury on MRI, and postnatal infections (clinical sepsis or positive culture infection, confirmed necrotizing enterocolitis).

3.3.3 MRI Image Acquisition

Newborns with HIE underwent at least one MRI scan post-TH after rewarming. Healthy newborns did not undergo MRI scanning. Newborns with HIE were scanned on a 1.5 T GE MRI scanner. A T1-weighted structural image was acquired (TR=8.4–11.5 ms [depending on clinical requirements], TE=4.2 ms, flip angle=12/25°, matrix size 512 × 512, 99–268 slices, voxel size typically 0.39 × 0.39 × 0.5 mm (0.31 × 31 × 5 to 0.43 × 0.43 × 0.6 for some neonates), as well as a T2-weighted structural image (TR=3517–9832 ms, TE=7.3–8.4 ms, flip angle = 90/160°, matrix size 256 × 256, 19–60 slices, 0.7 × 0.7 × 2–5 mm voxel resolution). Additionally, an echo planar imaging sequence to measure Blood Oxygen Level–Dependent (BOLD) fMRI data was also acquired to examine RSFC (TR=3000ms, TE=50 ms, flip angle=70°, matrix size 64 × 64, 39 slices, voxel size 3 × 3 × 3 mm, total volumes 35).

3.3.4 fMRI preprocessing and analysis

The fMRI data were preprocessed using FMRIB Software Library [88] (https://fsl.fmrib.ox.ac.uk/fsl/fslwiki/FSL). The preprocessing pipeline included brain extraction, motion correction, spatial smoothing (full width at half maximum = 5 mm), band-pass filtering (0.01-0.2 Hz) and registration to a neonatal atlas [159]. From the frontal, parietal, temporal and occipital lobes of both hemispheres, we extracted the average BOLD sequences. Then, we calculated the Pearson correlation among them to build an 8-by-8 RSFC map for each neonate (Fig. 3.1B).

3.3.5 T1-weighted image processing and segmentation

The T1 weighted scans were automatically segmented using infant FreeSurfer [199]. Automatic processing steps included intensity normalization, skull stripping, and segmentation of the cortex, white matter and subcortical structures [199]. A multi-atlas approach was employed for the segmentation. Multiple brain atlases of newborns were first registered to native space, and structure labels were transferred. The atlases were developed from neonatal MRI scans [200]. To initially create the atlases, manually segmented labels were developed using MRI scans from a representative sample of neonates (0-2 years of

age). In the current study, developmentally appropriate atlases for newborns were employed. Labels were fused into a single segmentation result, providing higher accuracy than single-atlas approaches [201]. Volumetric measurements for anatomical features could then be extracted [199]. Brain subcortical brain structure volumes were extracted, as well as cerebral white matter and cerebral cortex volumes, to compute total cerebral volumes (TCV). Each segmented T1-weighted image was visually inspected using Freeview software, available within FreeSurfer. Manual segmentation was employed to correct any segmentation errors (i.e., partial volume effects) using ITK-SNAP (http://www.itksnap.org/).

3.3.6 Brain injury characterization

A pediatric neuroradiology fellow (LTARdM) scored the T1-weighted anatomical images for brain injury severity. White matter injury (WMI) was defined as foci exhibiting T1 hyperintensity without T2 hypointensity or by low-intensity T1 foci and was scored on a 3-point scale (none=0, minimal=1, moderate-severe=2-3 combined) using the methods of de Vries[202]. Intraventricular haemorrhage (IVH) was graded (none=0, mild=1-2, and moderate-severe=3-4) using Papile's method[22]. Only supratentorial injuries were scored.

3.3.7 fNIRS acquisition and analysis

fNIRS was acquired in newborns with HIE (within 3 days post-TH after rewarming) and healthy newborns using the same experimental setup. Participants were scanned using a NIRSport2 (NIRx, Berlin, Germany) system with 8 light sources and 8 detectors covering the whole brain. The system operates at two wavelengths of light (760 nm and 850 nm), and the sampling rate was 10.1725 Hz. For either hemisphere, 4 channels were located on the temporal, 2 on the parietal, frontal and occipital lobes (Fig. 3.1A). fNIRS scans lasted for a minimum of 6 minutes during rest or natural sleep with the neonates lying in the incubator, cot, or caregiver's arms.

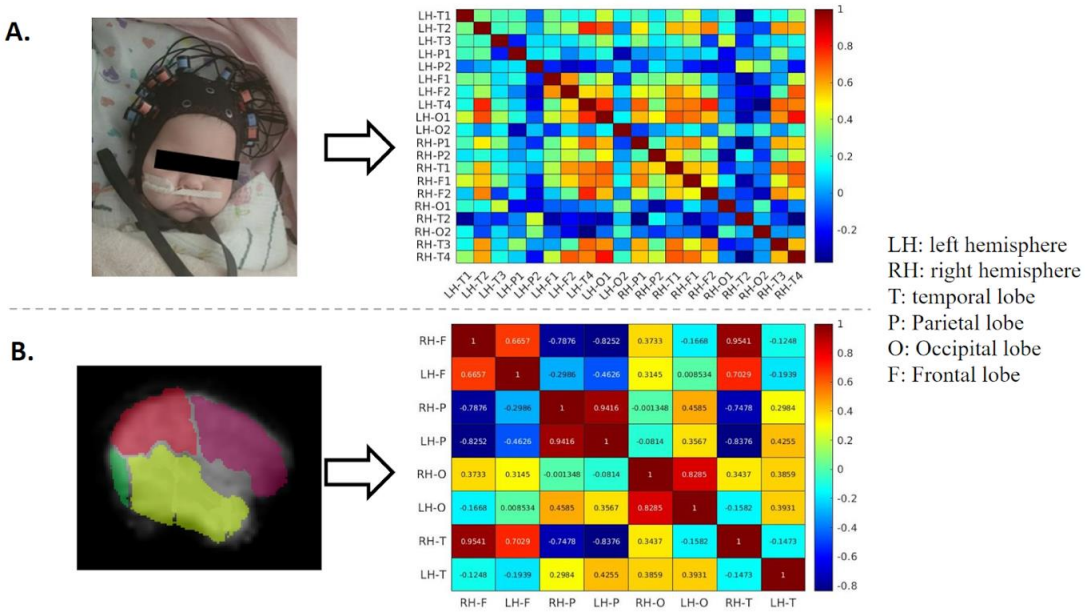

Figure 3.1: (A) Newborn wearing the fNIRS cap. Based on fNIRS recordings of oxygenated hemoglobin (HbO), 20-by-20 connectivity maps were created. (B) Atlas (lobe)-based analysis of the fMRI data. A hemisphere is sectioned into temporal, parietal, frontal and occipital lobes. 8-by-8 connectivity maps were built upon fMRI data. Colourbars indicate the Pearson correlation values.

After data acquisition, Homer3 software [203] was used for preprocessing. The pipeline included spline interpolation for motion correction[66], band-pass filtering of 0.01-0.1 Hz and conversion to HbO and Hbr fluctuations with modified Beer-Lambert law [58]. For each neonate, two connectivity maps, sized differently, were calculated using Pearson correlation. Channels corresponding to one lobe were averaged and then correlated with other cortices to build lobe-wise connectivity maps (8 by 8). 20-by-20 channel-wise RSFC maps were also calculated with individual channels corresponding with each other. HbO and Hbr data were both used for building connectivity maps separately (Fig. 3.1A).

3.3.8 Statistical Analysis

Statistical analyses were performed using Matlab (R2020b, Natick, Massachusetts: The MathWorks Inc).

For the first aim, which was comparing the RSFC maps yielded from the fNIRS and fMRI, Euclidean distances and Jaccard distances were calculated between the two 8-by-8 maps at various levels of sparsity [160]. It is considered common practice to filter out negative or low-weighted (positive but smaller than certain threshold) connections when analyzing RSFC maps, where the percentage of connections remaining is the level of sparsity of a map, i.e., the thresholds for filtering vary among individual connectivity maps. For weighted maps, we kept the original weights of connections, while for binarized maps, the remaining connections after filtering were rounded to 1. Given adjacency matrices of two maps $A_1 = [a_{ij}^1]$ and $A_2 = [a_{ij}^2]$, where a_{ij} was the weight of connection between node i and j, Euclidean distance between the two was defined as

$$d_E = \sqrt{\sum_{i,j} \left(a_{ij}^1 - a_{ij}^2\right)^2}, \tag{3.1}$$

while Jaccard distance was defined as

$$d_J = 1 - J, where\ J = \begin{cases} \frac{\sum_{i,j} min\left(a_{ij}^1, a_{ij}^2\right)}{\sum_{i,j} max\left(a_{ij}^1, a_{ij}^2\right)}, if \sum_{i,j} max\left(a_{ij}^1, a_{ij}^2\right) > 0 \\ 1, \quad otherwise \end{cases}. \tag{3.2}$$

We also calculated similarity maps for weighted and binarized RSFC maps between fNIRS and fMRI. Note that similarity maps had the same dimension as connectivity maps. For weighted cases, entries of similarity maps were the average Euclidean distance among subjects for the corresponding connections. In contrast, for binarized cases, they were the percentage of subjects sharing the connection. Volume counts of cortical grey matter obtained from T1-weighted images were associated with overall fNIRS and fMRI connectivity strength, respectively, using linear regression, adjusted for GA at birth, postmenstrual age (PMA) at scan and sex.

To address the second aim, which was identifying altered connectivity patterns between HIE neonates and healthy controls, we used graph theory-based measurements to quantify the patterns of 20-by-20 RSFC maps. On HbO and Hbr maps, we calculated the clustering coefficient of a map as

$$C_p = \frac{1}{N} \sum_i \frac{\sum_{j,k} a_{ij} a_{ik} a_{jk}}{\left(\sum_j a_{ij} - 1\right) \sum_j a_{ij}}, \tag{3.3}$$

where N was the number of nodes in the map. Network efficiency was also calculated locally as

$$NE = \frac{1}{N}\sum_i \left[\frac{1}{|G_i|(|G_i|-1)}\sum_{k\neq j\in G_i}\frac{1}{d_{jk}}\right], \tag{3.4}$$

where d_{ij} was the shortest distance N_i between i and j, G_i the node set containing i and its direct neighbors only, and $|G_i|$ the number of nodes of G_i. Modularity was defined as

$$M = \sum_p \left[e_{pp} - \left(\sum_q e_{pq}\right)^2\right], \tag{3.5}$$

where p was one of communities identified by a Louvain-like algorithm [117] and e_{pq} denoted the fraction of connections between community p and q. Based on clustering, the between-subject variation was calculated using mutual information[204]. Given a confusion matrix $C = [c_{wv}]$, where c_{wv} was the number of nodes in both community w and community v of two separate clusterings, respectively, mutual information was defined as

$$MI = \frac{-2\sum_{w,v}(c_{wv}\, ln\frac{c_{wv}N}{\sum_w c_{wv}\sum_v c_{wv}})}{\sum_w\left(\sum_v c_{wv}\, ln\frac{\sum_v c_{wv}}{N}\right)+\sum_v\left(\sum_w c_{wv}\, ln\frac{\sum_w c_{wv}}{N}\right)}. \tag{3.6}$$

T-tests were used to determine if the two groups were significantly different over a measurement.

To further demonstrate the distinctive power of connectivity measurements separating HIE neonates from healthy controls, we trained machine learning models of support vector machine (SVM) with several local metrics, including connectivity, clustering coefficient, nodal efficiency, degree centrality and closeness centrality, with 4-fold cross validation. The accuracies of classification were calculated, and receiver operating characteristic (ROC) curves were plotted. Areas under ROC curves (AUC) were also obtained.

3.4 Results

3.4.1 Participants

Twenty-one term-born neonates with HIE were enrolled (GA at birth = 38.92, SD=1.55 weeks, Table 3.1). Nineteen (90.4%) of the HIE neonates underwent TH before they were scanned with MRI and fNIRS. Two newborns who did not undergo TH were diagnosed with mild or moderate HIE. All newborns with HIE underwent an fNIRS scan at a PMA of 39.96, SD=1.43 weeks. Twelve (57%) of the HIE neonates had MRI scans (PMA = 39.94, SD=1.15 weeks). Detailed Characteristics for HIE participants can be found in Table 3.2.

Table 3.1: Participant Characteristics.

	HIE participants N=21	**Healthy newborns N=20**	**P-value**
Gestational Age, *weeks [SD]*	38.92 [1.55]	39.08 [1.21]	0.7
Sex, *male n, (%)*	12 (57.1)	9 (45)	0.4
Birth Weight, *kgs [SD]*	3.13 [0.59]	3.49 [0.4]	0.08
PMA at scan, *weeks [SD]*	39.96 [1.43]	39.93 [1.27]	0.1

Note. The median values and interquartile ranges. Probability values provide results using the t-test for continuous measures and Chi-square tests for categorical measures.

Table 3.2: Characteristics for HIE participants.

	HIE newborns (*n = 21*)
First pH (cord or peripheral)	Mean = 6.98, SD=0.16 Min = 6.8, Max = 7.4

	HIE newborns (*n = 21*)
	25th Percentile: 6.90 50th percentile: 6.92 75th percentile: up to 7.03
Apgar 5 min	Mean = 3.94, SD=2.6, Min = 0, Max = 9 25th Percentile: 2.25 50th percentile: 3.5 75th percentile: 5.75
Sarnat staging	**Mild**: 3 (14.3%) **Moderate**: 15 (71.4%) **Severe**: 3 (14.3%)
Therapeutic hypothermia	19 (90.5%)
Intubation at birth	10 (47.6%)
Days of ventilation	Mean = 4 days, SD = 7.0 Min = 0 days, Max = 28 days, SD = 5.11 days 25th Percentile: up to 0 days 50th percentile: up to 1.0 days 75th percentile: up to 5.3 days

Twenty healthy term-born infants were recruited from the MBCU of LHSC with a birth GA of 39.08, SD=1.21 weeks, and fNIRS scans were performed within 48 hours of life (Table 3.1). None of the healthy newborns underwent an MRI.

3.4.2 Brain Injury Characterization

Most newborns with HIE (n=20, 95%) had white matter injury identified using MRI (Table 3.3). Mild white matter injury was commonly seen in the neonates, regardless of HIE severity (n=19, 90%). Injury to the basal ganglia was identified in one (5%) neonate with severe HIE. The presence of IVH was only seen in one (4%) participant with severe HIE. No watershed injury was evident in any MRI scans of the newborns with HIE.

Table 3.3: Brain injury patterns in HIE participants.

HIE severity	Grade	Mild (n=3)	Moderate (n=15)	Severe (n=3)
White matter injury, n [%]	grade 1	3[67]	14[93]	2[67]
	grade 2	0	0	1[33]
	grade 3	0	0	0
Intraventricular haemorrhage, n [%]	grade 1	0[0]	0[0]	0[0]
	grade 2	0[0]	0[0]	1[33]
	grade 3	0[0]	0[0]	0[0]
Basal ganglia, n [%]		0[0]	0[0]	1[33]
Watershed injury, n [%]		0[0]	0[0]	0[0]

Note. White matter injury was scored according to de Vries [202]. Intraventricular haemorrhage grade was scored using the method of Papile [22]; Positive = any morphological abnormality.

3.4.3 Comparing fNIRS and fMRI

Lobe-wise 8-by-8 connectivity maps were obtained from fNIRS for HbO and Hbr for neonates with HIE. Euclidean and Jaccard distances were used to compare fNIRS and fMRI connectivity maps at levels of sparsity (Fig. 3.2A). Means, standard deviations (SD) and 95% confidence intervals (CI) of the two metrics were calculated based on subject-by-subject comparisons. Sparsity ranged from 0.2 to 0.46. We also calculated the similarity map (Fig. 3.2B) between the two modalities.

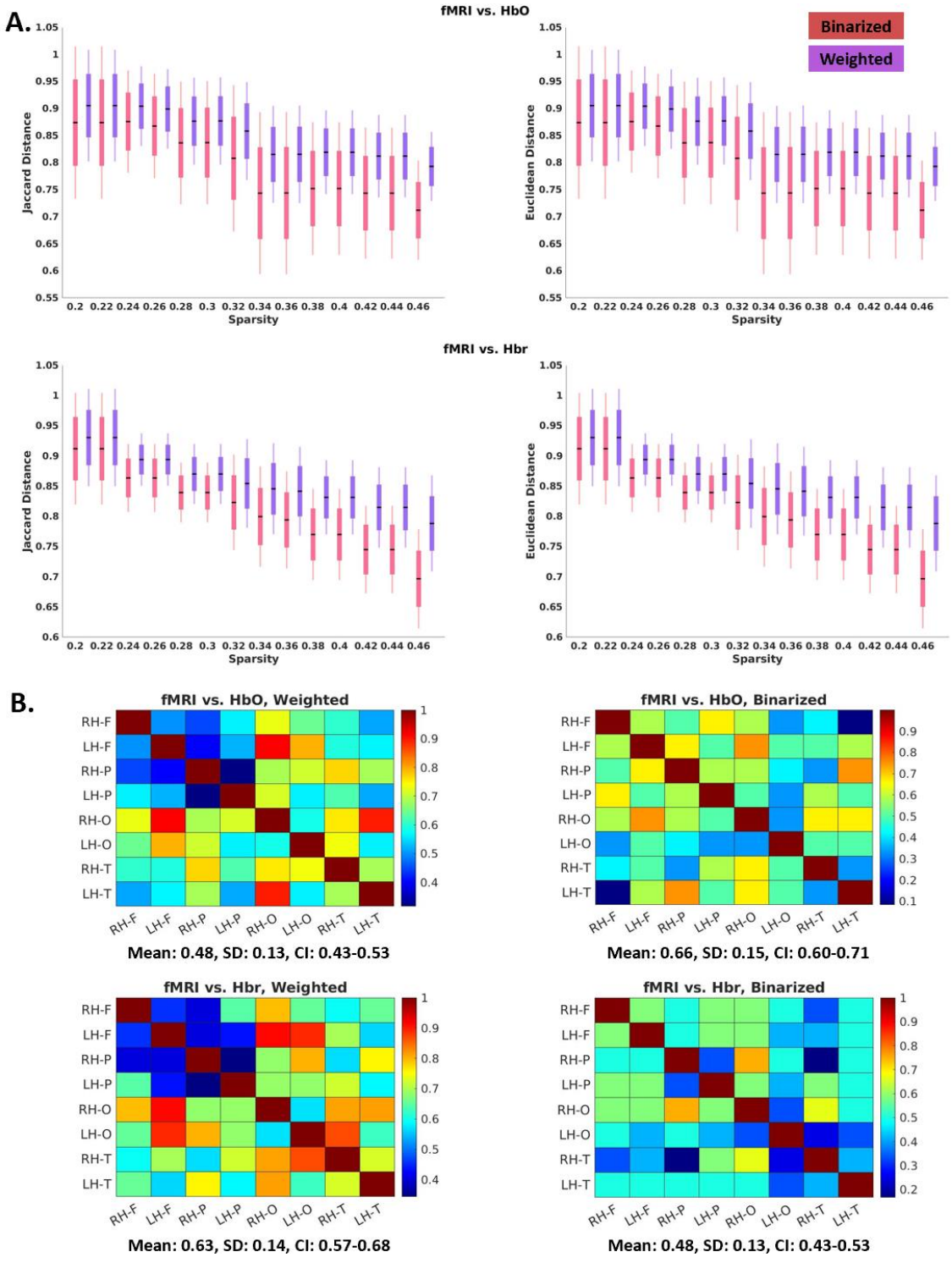

Figure 3.2: (A) Similarity of RSFC maps between fMRI with respect to HbO and Hbr, measured by Euclidean distance (right panel) and Jaccard distance (left panel). Both weighted and binarized maps were implemented. (B) Lobe-wise similarity maps at a

sparsity of 45%. Color bar denotes the value of similarity. Higher values reflect greater similarity between the two modalities. For weighted cases, entries of similarity maps were the average Euclidean distances among subjects for the corresponding connections. In contrast, for binarized cases, they were the percentage of subjects sharing the connection.

We also showed the correlation between brain volume and FC (Fig. 3.3). Correlations were calculated with whole-brain grey matter or white matter volume against HbO, Hbr or fMRI connectivity. Connectivities were summed over all connections, which were weighted and not filtered. We showed that FC increases with either grey or white matter volume. HbO connectivity showed a significant positive correlation with grey and white matter volumes (p-values were 0.015 and 0.011, respectively.), adjusted for birth GA, PMA at scan and sex. While Hbr and fMRI connectivities were not significantly correlated with volumes, they still increased with volume growth.

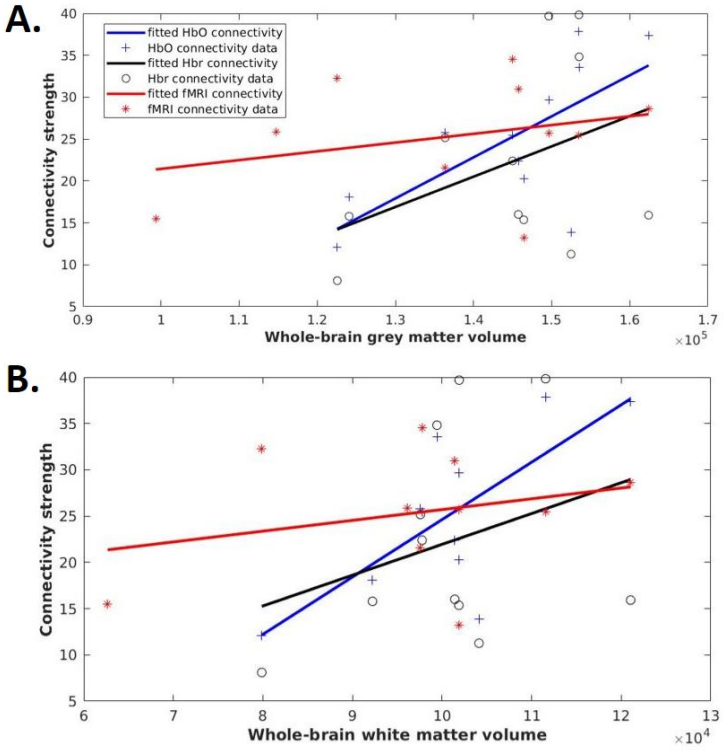

Figure 3.3: Brain volumes (in voxel count) and fNIRS- and fMRI-based functional connectivity strength. Total functional connectivity strength (y axis) of oxygenated

(HbO, blue lines and plus [+] signs), deoxygenated (HBr, black lines and open circles [o]) hemoglobin and fMRI-based functional connectivity (red lines and stars [*]) in relation to grey matter volumes (A, x axis) and white matter volumes (B, x axis).

3.4.4 Altered RSFC patterns of neonates with HIE

Based on the connectivity maps obtained from fNIRS data, graph theory-based metrics were calculated to characterize patterns of RSFC and identify differences between HIE and control groups (Fig. 3.4). It was shown that the HIE group had increased clustering coefficient, network efficiency and modularity compared to controls, but had lower consistency within the group.

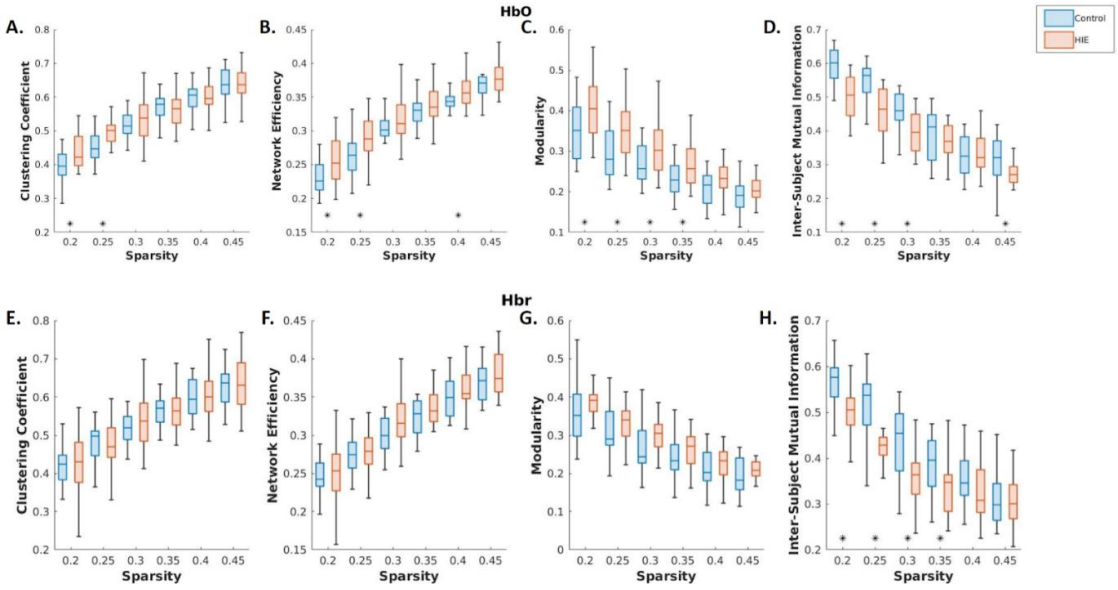

Figure 3.4: Graph theory-based metrics measuring the differences in fNIRS RSFC patterns between newborns with HIE (red) and healthy controls (blue). The metrics were calculated at various levels of sparsity (0.2-0.45). *p<0.05

Local measurements, including connectivity, degree centrality, closeness centrality, clustering coefficient and node efficiency, were calculated and used as features for training SVM classifiers to distinguish the HIE group from the control. Note that only features showing significance in t-tests were selected to train SVM models. We achieved a maximal

accuracy of 75.61% and a maximal AUC of 0.75 with connectivity features (Fig. 3.5A) using 4-fold cross validation.

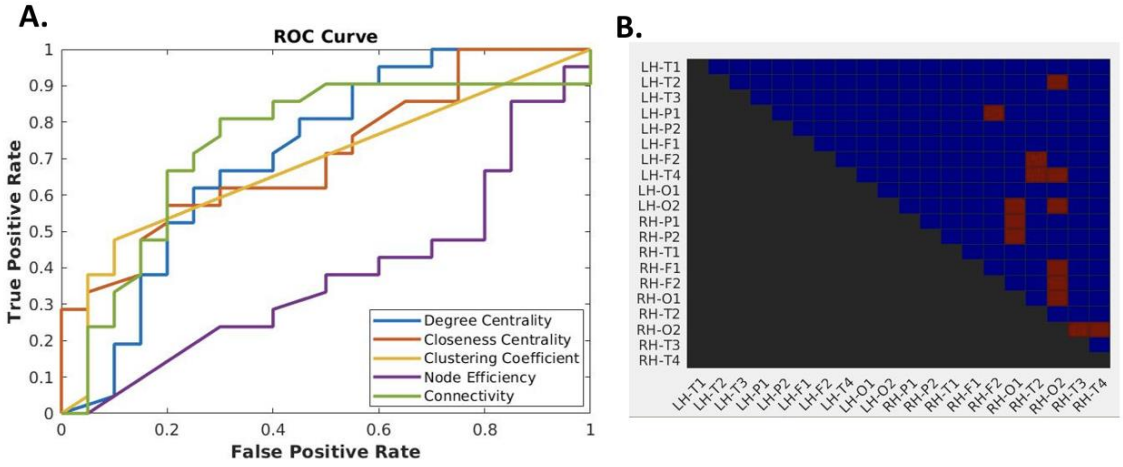

Figure 3.5: A. ROC curves of SVM classifiers trained with connectivity features. In the order shown in the legend, maximal accuracies of individual feature sets were 68.29%, 68.29%, 68.29%, 51.22% and 75.61%, respectively. AUCs were 0.71, 0.71, 0.69, 0.36 and 0.75, respectively. B. The connections marked red were those showing significance in t-test and chosen to train SVM.

3.5 Discussion

Despite the wide adoption of TH along with other interventions, HIE remains a major cause of mortality as well as later physical and cognitive difficulties. In this study, we examined functional connectivity patterns in a heterogeneous cohort of newborns with HIE using multi-modal imaging methods. RSFC maps yielded from fNIRS and fMRI were comparable within the cohort of HIE newborns. Further, positive associations between grey and white matter volumes, a marker of brain health, and fNIRS and fMRI connectivity strength were evident. Our findings provide support for fNIRS to be a promising bedside monitoring method to be used alongside other imaging technologies, especially for newborns receiving care in the NICU. We also demonstrated altered fNIRS-based connectivity patterns in HIE neonates compared to healthy newborns and the distinctive power of these connectivity features with machine learning models. Results indicated that fNIRS-based RSFC may be a novel biomarker of brain health in HIE.

The RSFC maps derived from fNIRS (HbO or Hbr) were comparable to fMRI in newborns with HIE who underwent TH. Our findings align with previous studies demonstrating good correspondence between fNIRS and fMRI. In adults, Sasai et al. [106] reported good spatial correspondence between fNIRS and fMRI on several resting-state networks using seed-based analyses. Further, Duan et al. [107] in an adult population reported positive correlations between fNIRS and fMRI connectivity strength as well as similar topological patterns at different levels of sparsity. Anwar et al. [205] recorded simultaneous fNIRS, fMRI and EEG in adults to show bi-directional connectivity that occurs within sensorimotor networks, using Granger causality. In infants, less work has focused on comparing resting-state networks using fNIRS and fMRI. However, Bulgarelli et al. [108] demonstrated a strong resemblance between fNIRS and fMRI connectivity using dynamic causal modeling in a 6-month-old infant.

In the current work, we further examined fNIRS- and fMRI-based connectivity in relation to grey and white matter volumes as a separate marker of brain health. Previous MRI studies conducted during the early stages of brain development demonstrated positive associations between FC strength and brain volumes [122], [206], [207]. fNIRS-based connectivity was significantly associated with both grey and white matter volumes. Our findings indicate that in the hypoxic newborn, FC can be maintained while adapting to changes in brain volume. However, this finding was primarily driven by HbO-based connectivity. In contrast, fMRI- and Hbr-based connectivity only showed positive trends towards an association with brain volumes. The physiological basis of the BOLD and Hbr signals are comparable in that they are both sensitive to changes in Hbr and are coupled to underlying changes in neuronal activity. In turn, connectivity based on deoxygenation changes may show less association with grey and white matter development in the rapidly changing newborn brain, as these processes are supported by synaptogenesis and myelination and are highly dependent on oxygen and nutrient delivery. An additional consideration is that the temporal dynamics of RSFC have been widely documented [208], [209], and methodological differences in the fNIRS and fMRI acquisition and analyses could further explain the inconsistency in the results.

When comparing fNIRS-based RSFC between neonates with HIE and healthy controls, the HIE group showed increased clustering coefficients, network efficiency and modularity. These metrics are commonly considered to be indicative of the small-worldness of networks. Small-worldness is characterized by high clustering and short path length and is commonly seen in brain networks [114], [210]. Findings suggest that brain regions with similar functions demonstrated more synchronized activity and had more highly connected hubs that support efficient global communication. Similar findings were documented by Gozdas et al. [211], who reported increased modularity in preterm-born neonates, but using fMRI-based connectivity metrics. Additionally, using fNIRS, Zhang et al. [132] also reported increases in several small-world metrics in newborns with HIE. An increase in small-worldness in the HIE population may reflect disruptions in the underlying white matter fiber pathways that may be reflected in severed long-range connectivity but strengthened local connectivity through neural compensation and reorganization. These compensatory mechanisms may be a common feature in neonates born critically ill [180] that can even be seen later in adulthood [212] or neurological disease states [213]. Increased functional connectivity within local networks has been reported previously. For example, newborns scanned with fNIRS demonstrated positive associations between connectivity strength of homologous-interhemispheric networks as well as behavioral measures of negative emotionality [214]. In relation to the current study, our findings of increased functional connectivity could also partially be influenced by exposure to invasive NICU procedures (TH, tape removal, skin breaks, etc.) experienced by the newborns. Further, increased grey matter cerebral blood flow within sensorimotor networks has been reported in preterm born infants [215], which may have also been a contributing factor to the increased functional connectivity within the networks seen in our study. Future studies could address whether these changes are related to underlying brain injuries associated with HIE and predict local changes in connectivity. Further, an increased variation of clustering among neonates with HIE was evident and could also be a result of variations in the severity of HIE, IVH, or be related to white matter injury or a combination of these factors. Given our sample size, we could not further assess whether the variations in clustering were related to clinical factors or variations in care practices, but this could be explored in future work.

Machine learning models were implemented in the current study to determine whether RSFC features can be potential biomarkers of HIE. Optimal performance was realized when using connectivity features that were a product of significant connections that were either interhemispheric or within the right hemisphere. Altered interhemispheric or long-range connections have been reported in multiple studies [130], [131], which may be related to HIE-induced injury or inflammation localized to the white matter or even subcortical areas, which are key to long-range neuronal signal transmission. Connections within hemispheres were significantly different in the right but not the left hemispheres. Further examination as to whether there may be hemispheric vulnerability to HIE is needed. Massaro et al. [216] demonstrated that the magnitude of cerebral pressure in the right hemisphere was predictive of adverse outcomes detectable by MRI. Whether a similar lateralization effect due to changes in intracranial pressure occurred in the current sample remains unknown but could have been an underlying factor.

The majority of the HIE participants were scanned after TH and rewarming. The two participants who had mild HIE were not candidates for TH. Given that these newborns represented a small fraction of the total dataset, they were unlikely to have unduly influenced the results. While TH is the standard of care for newborns with severe or moderate HIE, our findings demonstrating altered RSFC maps suggest that disrupted functional organization of the brains persists after TH. The persisting disrupted RSFC patterns could also contribute to adverse developmental outcomes in the first few years of life [217], [218]. The present study focused on RSFC patterns in newborns with HIE, and future studies should incorporate long-term developmental outcomes. This would be the next step to determine how fNIRS markers of brain health at the bedside can predict developmental abilities in newborns with HIE.

The strengths of our study are grounded in several areas. Firstly, this was a single-centre study with a well-characterized cohort of newborns with HIE and healthy newborns. Also, a high-density fNIRS system offered coverage of the newborn brain's frontal, parietal, temporal and occipital areas. We also had the opportunity to characterize functional networks that were related to brain structure in the HIE population; however, not all participants had the same measures available. The MRI scans were conducted as part of

clinical care and after TH and rewarming. Given the timing of the MRI scans, some families could only consent to the fNIRS component of the study. While the goal of the study was to compare RSFC maps obtained using fNIRS and fMRI, these two modalities could not be obtained at the same time in our sample due to a lack of resources in a clinical imaging center. The duration of the fMRI scanning sequence was relatively short. However, the neonates underwent clinical imaging before the research sequences and could only be away from the NICU for a short period of time. The fMRI protocol was tested in an adult prior to scanning the newborns, further the networks were assessed in individual newborns to determine their robustness. Additionally, the fNIRS probes were not precisely located in the MRI space, and the fMRI data were analyzed using an atlas approach. In turn, the spatial correspondence between the fNIRS and fMRI data could be improved in future work. Another consideration is that the fNIRS data may have been influenced by physiological noise. In adults, short-distance channels are frequently implemented in fNIRS studies as a means to assess surface-artefacts, signal quality, source localization, and improve signal decomposition [77]. However, in neonates placing short distance channels on channels that already very close together is ineffective due to the smaller surface area of the head in neonates compared to adults [75]. Another approach for future studies with neonates would be to collect physiological measurements (i.e., heart rate) using external monitoring and use these measurements to improve signal decomposition.

3.6 Conclusions

In this study, we determined the utility of fNIRS to assess RSFC as a potential biomarker for brain health in term-born neonates with HIE. By incorporating a multimodal neuroimaging investigation using fNIRS, fMRI and structural MRI, we showed that fNIRS-based RSFC patterns were comparable to those seen with fMRI and that these metrics were predictive of brain volumes. We further demonstrated that fNIRS-based RSFC maps differed between HIE and healthy newborns. Lastly, fNIRS-based connectivity metrics performed well in machine learning models to determine diagnostic group membership. Overall, study findings indicate that altered fNIRS-based RSFC patterns can be potential biomarkers of HIE. fNIRS at the bedside could be complementary to other imaging modalities in terms of characterizing neonatal brain function.

Chapter 4

4 Predicting cortical-thalamic functional connectivity using functional near-infrared spectroscopy and graph convolutional networks

This chapter is adapted from the publication entitled “Predicting cortical-thalamic functional connectivity using functional near-infrared spectroscopy and graph convolutional networks” submitted to Scientific Reports in 2024 by Lingkai Tang, Lilian M. N. Kebaya, Homa Vahidi, Paige Meyerink, Sandrine de Ribaupierre, Soume Bhattacharya, Keith St. Lawrence, and Emma G. Duerden and is currently under review.

4.1 Abstract

Functional near-infrared spectroscopy (fNIRS) measures cortical changes in hemoglobin concentrations, yet cannot collect this information from the subcortices, such as thalamus which is involved in several key functional networks. To address this drawback, we propose a machine-learning-based approach to predict cortical-thalamic functional connectivity using cortical fNIRS data. We applied graph convolutional networks (GCN) on two datasets obtained from healthy adults and neonates with early brain injuries. Each dataset contained fNIRS connectivity data as input to the predictive models and connectivity of functional magnetic resonance imaging (fMRI) as training targets. GCN models performed better compared to conventional methods, such as support vector machine and feedforward fully connected artificial neural network, on both identifying the connections as binary classification tasks, and regressing the quantified strengths of connections. We also propose the addition of inter-subject connections into the GCN kernels could improve performance and the GCN models are robust against noise in fNIRS data. Our results show it is feasible to indicate subcortical activity from cortical fNIRS recordings and the study can potentially extend the use of fNIRS in clinical settings for monitoring brains of critically ill patients.

4.2 Introduction

Functional NIRS measures changes in hemoglobin concentrations as an indirect measure of brain activity [195]. Functional NIRS has been successfully introduced in clinical settings in both adult and paediatric populations, as a bedside monitoring tool, particularly for patients impacted by critical illness, where minimizing invasive imaging procedures involving transport or exposure to radiation are key priorities [158], [164], [219], [220]. However, one major drawback is that fNIRS can only detect changes at the cortical level, as it is limited by penetration depth of near-infrared light. Consequently, fNIRS cannot collect hemodynamic information from deep brain regions, such as the thalamus, an important relay between the cortex and the nervous system that subserves key cognitive, motor, and sensory processes [221], [222], [223]. Further alterations in thalamocortical pathways due to clinical care or brain injury can lead to cognitive and motor deficits [224], [225], [226], [227]. At the same time, conventional clinical magnetic resonance imaging (MRI) approaches to study deep brain regions are limited by the accessibility of MRI scanners to patients who are critically ill and sensitivity to motion. fNIRS can be applied under many scenarios where MRI cannot such as at the bedside of patients for short- or long-term monitoring. Therefore, deriving deep brain, especially thalamic, connectivity pathways from cortical recordings with computational methods, would largely extend the range of fNIRS studies and clinical applications.

Despite the strong need in fNIRS research for analytic tools to predict subcortical activation from that seen in the cortex, as far as we know, little research has focused on this issue [228]. A previous study implemented a supervised machine learning model, using support vector regression (SVR), to predict hemodynamic responses of several deep brain regions using simultaneously recorded fNIRS and fMRI in healthy adult participants. The SVR models were trained with subject-dependent cortical time series as inputs and fMRI subcortical recordings as ground truths for validation. Positive correlations between predicted and true sequences were evident, highlighting the feasibility of the method to predict subcortical activation from fNIRS-based cortical activation.

The popularization of machine learning methods over the last decade has opened up opportunities for the development of universal (subject-independent) models to predict subcortical activity from cortical activity. A specific type of artificial neural network, namely GCN, was recently introduced by Kipf et al. [229] Derived from convolutional neural networks, GCN is efficient for extracting high-level features from graphs by using the topology among samples as kernels. GCN models have been combined with neuroimaging technologies, where connectivity maps of brains were introduced as graph kernels for GCN. Zhao et al. combined GCN with functional connectivity maps from resting-state fMRI (rs-fMRI) to predict attention deficit hyperactivity disorder (ADHD) diagnosis and identify atypical connectomes [230]. Li et al. predicted infant age using rs-fMRI data; yet, graph paths were incorporated into convolutional kernels to compensate for indirect paths between brain regions [231]. Functional NIRS data have been also used for training GCN models. Zhang et al. predicted autism diagnosis by combining GCN units with recurrent structures to capture both spatial and temporal dynamics of fNIRS functional connectivity [232].

In the current work, we aimed to develop a universal model, that is not subject-dependent as in [228], using GCN methods to determine whether task-based and task-free cortical fNIRS connectivity would predict cortical-thalamic connectivity. The current study examined two heterogenous cohorts of adults and neonates. The models were developed from an fMRI-fNIRS dataset in healthy adults and infants born critically ill, respectively. The two cohorts were examined because firstly, the long-term goal of the research is to develop fNIRS based analytic tools to monitor brain function in infants in intensive care. In turn, better characterization of cortical and subcortical in the neonate are needed to evaluate a prediction model to use with fNIRS data recorded at the bedside. Secondly, inherent differences in connectivity patterns in adults and neonates were identified. Imaging studies have demonstrated the rapid development of the infant brain during the first few years of life [133], [233]. Basic functional networks (default mode, somatomotor, visual, etc.) emerge at very early ages [191], [206], [234], [235]. Differences in the connectivity patterns are evident between infants and adults. For example, adult default mode networks integrate long- and short-range areas, while in the neonatal and infant brain, individual parts may demonstrate less synchronized organization [236]. Also, in a very

early study of resting-state connectivity, network hubs were localized differently in adults compared to infants [237].

To train the GCN models along with other machine learning models for comparison, we considered cortical fNIRS connectivity as input and cortical-thalamic fMRI connectivity for validation. Participants underwent both fMRI and fNIRS. Adult participants completed a resting-state scan along with a visually-guided finger-tapping task during simultaneous fMRI and fNIRS scanning, so that the predictive models could be examined in different brain states (i.e., task-based or task-free activity), and finger tapping can reliably activate primary motor cortex where fNIRS probes were located. We compared fully connected feedforward artificial neural networks (ANN), support vector machines (SVM), and GCNs, to identify the best method to predict deep brain connectivity from cortical fNIRS recordings in adults. The fNIRS-prediction method was also applied to data collected in a clinical population of neonates who were scanned using a task-free paradigm. The overall goal was to determine if the fNIRS-prediction method could be used in clinical settings, for patients who require brain-monitoring but whose access to conventional imaging methods such as MRI would be limited.

4.3 Methods

4.3.1 Participants

A total of 20 healthy adult participants were recruited from the local London community for the study (average age: 25.6, standard deviation [SD]=3.1 years, male: 9). Neonatal participants with hypoxic ischemic encephalopathy (HIE) or intraventricular hemorrhage (IVH) were recruited from the neonatal intensive care unit (NICU) at the Children's Hospital of South Western Ontario, London, Canada. A total of 21 HIE neonates (gestational age [GA] at birth: 39.27, SD=1.26 weeks, male: 9) and 16 IVH ones (birth GA: 27.08, SD=3.03 weeks, male: 10) were recruited. Neonates were excluded from the study if there was evidence of major anomalies of the brain or other organs, congenital infections (e.g., TORCH), intrauterine growth restriction (IUGR), identifiable metabolic

disorder or ultrasound evidence of a large parenchymal hemorrhagic infarction. Detailed severity of brain injuries can be found in Table 4.1.

Table 4.1: Clinical scores of newborns with HIE and IVH.

HIE severity	**Mild**	**Moderate**	**Severe**		
n [%]	3[14]	15[71]	3[14]		
IVH severity	**Grade 0**	**Grade 1**	**Grade 2**	**Grade 3**	**Grade 4**
Left hemisphere, n [%]	2[13]	2[13]	5[31]	4[25]	3[19]
Right hemisphere, n [%]	1[6]	2[13]	4[25]	7[44]	2[13]

Note. HIE severity was categorized according to de Vries [202]. Intraventricular hemorrhage grade was using scored using the method of Papile [22]. The percentages were rounded therefore the summations were not 1.

Studies were approved by the Health Sciences Research Ethics Board at Western University. Informed consent was provided by the adult participants or parents/caregivers of the newborns. The study was conducted in accordance with the Declaration of Helsinki.

4.3.2 Experimental procedures

Adult participants underwent simultaneous fMRI and fNIRS for 3 consecutive finger-tapping sessions followed by a task-free session. All sessions were 6 minutes. Finger-tapping sessions included repetitive 30-second tapping and 30-second rests. Participants were asked to tap sequentially with all fingers of their right hands. There were short breaks between sessions.

Neonates were scanned at term equivalent age (age at fNIRS scan [HIE and IVH infants]: 38.57, SD=2.00 weeks) for 6 minutes during natural sleep (i.e., task-free state). fNIRS and fMRI were not acquired simultaneously due to incompatibility of NICU fNIRS system with fMRI. The fNIRS and fMRI scans were 3.48 days away on average.

4.3.3 MRI Image Acquisition

Adult participants were scanned on a 3T Biograph mMR PET-MR system (Siemens, Erlangen, Germany) (Fig. 4.1a). Anatomical T1 weighted images were acquired for each participant using an MPRAGE sequence (TR=2000 ms, TE=4.18 ms, Inversion time [TI]=900, flip angle=9°, matrix size 256 × 256, 176 slices, voxel size typically 1 × 1 × 1 mm). An EPI (echo planar imaging) sequence was used to acquire blood oxygen level-dependent (BOLD) fMRI data under the task-free (resting-state) condition as well as during the finger-tapping sessions (TR=3000 ms, TE=30 ms, flip angle=90°, matrix size 64 × 64, 45 slices, voxel size 3 × 3 × 3 mm, total volumes 122).

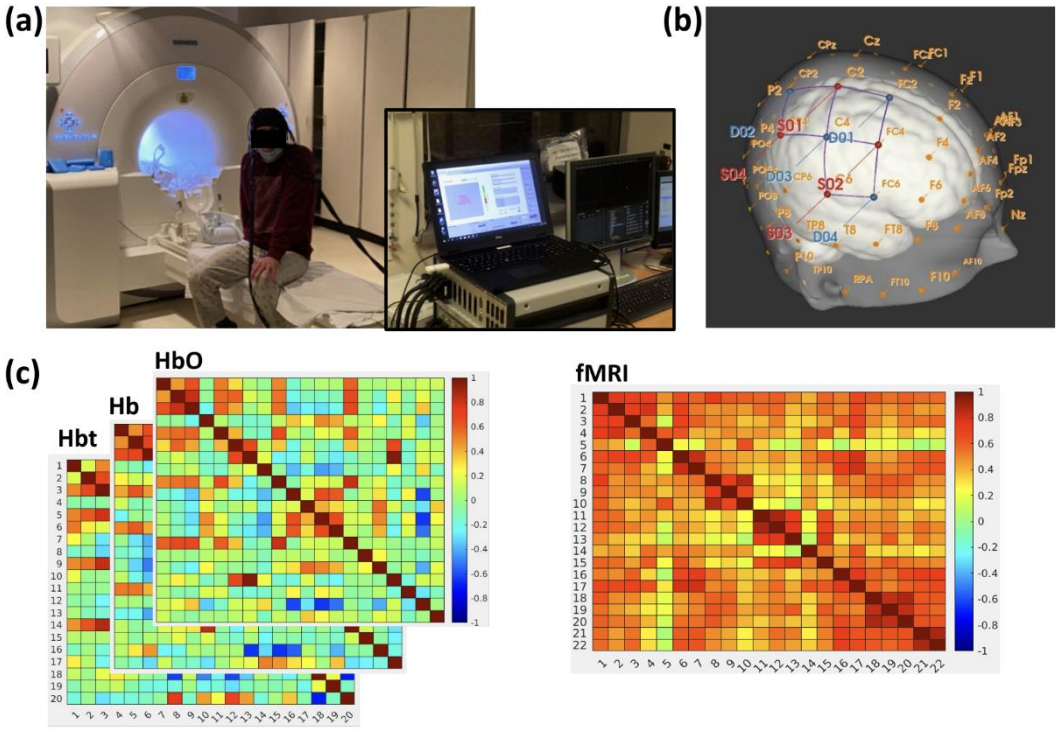

Figure 4.1: (a) An adult participant prepared for an fNIRS/fMRI scan. fNIRS optodes were connected to the console in the control room. (b) Adult fNIRS montage generated with NIRSite software (NIRx, Berlin, Germany). Only data from the right hemisphere is displayed, but the montage was symmetrical between left and right hemispheres. Light sources were marked in red and detectors in blue. Layout of probe locations followed the 10-10 system [238]**. Coordinates of the fNIRS probes in MNI**

space can be found in Table 4.2. (c) Example connectivity maps developed using Pearson correlations for fNIRS (left) and fMRI (right), respectively, from a participant. Numbers on the axes provide indexes for fNIRS channels (for HbO, Hb and Hbt), or the thalami and cortical regions that were covered by fNIRS channels (for fMRI). Colourbars indicate the Pearson correlation values.

Newborns underwent MRI scans with a 1.5 T GE MRI scanner. A T1-weighted structural imaging volume was acquired (TR=8.4–11.5 ms [depending on clinical requirements], TE=4.2 ms, flip angle=12/25°, matrix size 512 × 512, 99–268 slices, voxel size typically 0.39 × 0.39 × 0.5 mm (0.31 × 31 × 5 to 0.43 × 0.43 × 0.6 for some neonates), as well as T2-weighted structural image (TR=3517–9832 ms, TE=7.3–8.4 ms, flip angle = 90/160°, matrix size 256 × 256, 19–60 slices, 0.7 × 0.7 × 2–5 mm voxel resolution). Additionally, an EPI sequence was used to acquire resting-state functional connectivity data (TR=3000ms, TE=50 ms, flip angle=70°, matrix size 64 × 64, 39 slices, voxel size 3 × 3 × 3 mm, total volumes 35).

4.3.4 fMRI preprocessing and analysis

The fMRI data were preprocessed using FMRIB Software Library (https://fsl.fmrib.ox.ac.uk/fsl/fslwiki/FSL) [88]. The preprocessing pipeline included brain extraction, motion correction, spatial smoothing (full width at half maximum = 5 mm) and band-pass filtering (0.01-0.1 Hz). The adult fMRI images were registered to MNI152 space and average thalamic BOLD signals were extracted using Harvard-Oxford subcortical structural atlases [239] integrated within FSL. The cortico-thalamic connectivity, later used for training the machine learning models, was measured as the BOLD correlations between thalami and cortical brain regions covered by fNIRS channels. To extract these BOLD sequences, firstly, the fNIRS optodes, which followed the 10/10 system of probe placement [238], were localized to MNI152 space following the work of Jurcak et al. (Table 4.2) [240]. Then, a banana-shaped photon-hitting density function introduced by Feng et al. was implemented to evaluate a probability density map corresponding to each fNIRS channel [59]. Finally, BOLD time-series were extracted from brain voxels weighted by the probability density map and averaged to obtain one sequence for a single fNIRS channel

[60]. This yielded 20 BOLD time-series in total, corresponding to 20 cortical regions covered by 20 fNIRS channels. For each session of each participant, Pearson and partial correlations were calculated amongst the BOLD signals from the thalami (i.e., both hemispheres) and 20 cortical regions covered by the fNIRS channels (Fig. 4.1c).

Table 4.2: MNI coordinates of fNIRS probes (in mm).

Source No.	X Coordinate	Y Coordinate	Z Coordinate
1	30.30	-15.34	71.93
2	54.14	-45.20	54.30
3	68.27	-19.49	27.21
4	50.28	15.11	46.81
5	-28.42	-14.61	71.47
6	-53.52	-45.00	55.10
7	-66.97	-18.78	27.57
8	-48.32	15.47	45.88
Detector No.			
1	27.88	17.56	63.22
2	27.84	-45.22	72.83
3	56.09	-17.28	54.34
4	63.63	9.02	21.85
5	-25.97	16.31	62.52
6	-27.72	-45.09	72.19
7	-54.45	-17.14	54.73

8	-61.27	10.60	21.22

The neonatal images were preprocessed with the same pipeline but were registered to a neonatal atlas [159]. From the frontal, parietal, temporal and occipital lobes, as well as thalamus of both hemispheres, we extracted the average BOLD sequences. Then, we calculated the Pearson and partial correlations among them to build a functional connectivity map for each neonate (Fig. 4.2b).

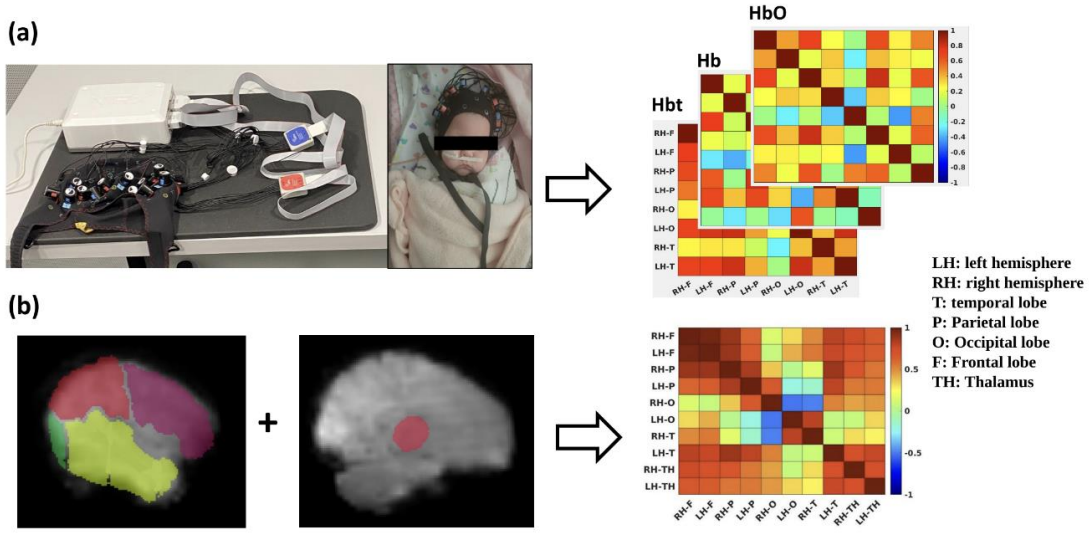

Figure 4.2: (a) The NIRSport2 system used in this study (left) and a neonate wearing optodes in the NICU (Caregiver permission was obtained, right). Based on fNIRS data, 8-by-8 connectivity maps were built for participants. (b) Time series of 10 regions (5 in each hemisphere) were extracted from fMRI images of neonates, then used to build the connectivity maps. Connectivity maps in this figure are from data collected from a single participant. Colorbars indicate the value of Pearson correlation.

4.3.5 fNIRS acquisition and analysis

Adult fNIRS was acquired using a NIRScout2 (NIRx, Berlin, Germany) system with 8 light sources (laser, wavelengths of 785 and 850 nm) and 8 detectors (sampling at 7.81 Hz) yielding 20 channels covering parts of the frontal and parietal lobes (Fig. 4.1b). Neonatal

participants were scanned using a NIRSport2 (NIRx, Berlin, Germany) system with 8 light sources (LED, wavelengths of 760 and 850 nm) and 8 detectors (sampling at 10.17 Hz) covering the whole brain. For either hemisphere, 4 channels were over the territories of the temporal, 2 on the territories of the parietal, frontal and occipital lobes (Fig. 4.2a).

Preprocessing both adult and neonate fNIRS data was done through Homer3 software [203]. The pipeline included spline interpolation for motion correction[65], band-pass filtering of 0.01-0.1 Hz and conversion to concentration changes of three chromophores, which were oxygenated hemoglobin (HbO), deoxygenated hemoglobin (Hb) and total hemoglobin (Hbt) [58]. For each neonate, fNIRS channels corresponding to one lobe were averaged first to have lobe-wise sequences, since anatomically, we could not localize them more accurately. Pearson and partial correlations [102] were subsequently calculated between fNIRS sequences for adults (Fig. 4.1c) and neonates (Fig. 4.2a), respectively. The three chromophores were calculated separately.

4.3.6 Graph convolutional networks

We aimed to predict functional cortical-thalamic connectivity from cortical connectivity using machine learning models, particularly the GCN. The GCN is derived from an ordinary convolutional neural network, and uses connectivity maps as kernels [229]. Given the adjacency matrix A of a connectivity map with n nodes and the node attribute matrix H_l, a convolutional block can be expressed as

$$H_{l+1} = \sigma\left(D^{-\frac{1}{2}}AD^{-\frac{1}{2}}H_l W_l\right), \tag{4.1}$$

where D is a diagonal matrix with $D_{ii} = \sum_j A_{ij}$, W_l is a linear transformation with trainable entries, and σ is an activation function which was rectified linear unit (ReLU) in this study. D also serves as kernels in the model.

A recent development of GCN allowed multiple kernels to be introduced into the model [241]. A convolutional block corresponding to kernel k that combines outputs from all kernels can be defined as

$$H_{l+1}^{(k)} = \sigma\left(\sum_m D^{(m)^{-\frac{1}{2}}} A^{(m)} D^{(m)^{-\frac{1}{2}}} H_l^{(m)} W_l^{(mk)}\right), \tag{4.2}$$

where $D^{(m)^{-\frac{1}{2}}}A^{(m)}D^{(m)^{-\frac{1}{2}}}$ denotes the kernel m and $W_l^{(mk)}$ denotes the linear transformation from kernel m to kernel k. (Fig. 4.3). At the end to convolutional layers, the summation of output from all kernels is obtained as

$$H_l = \sigma\left(\sum_k H_{l-1}^{(k)}\right), \tag{4.3}$$

which is then input to fully connected layers, so that the whole model can do either classification or regression.

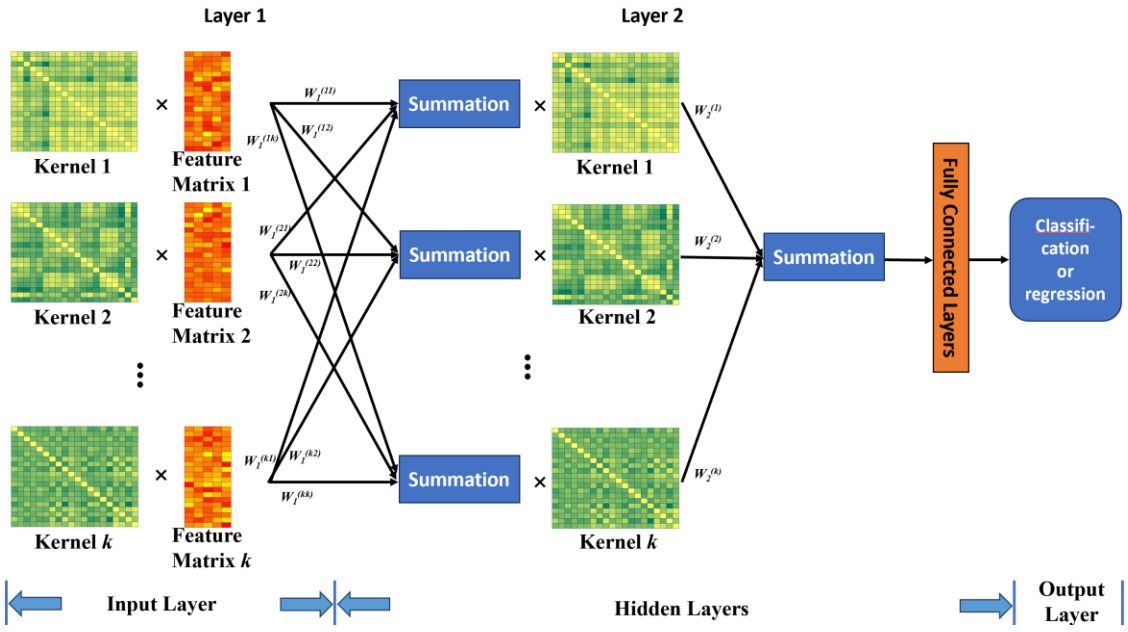

Figure 4.3: Structure of GCN models with multiple kernels with *W* denoting the trainable weights of linear transformations. There could be more layers, but in our settings, we had only 2 convolutional layers. With fully connected layers attached, the model can do either classification or regression. In our settings, there were 3 kernels, each corresponding to HbO, Hb or Hbt. Each kernel was multiplied by a feature matrix of the corresponding chromophore.

4.3.7 Implementation details

In our setup, each cortical node from each session for each participant was considered as a sample, meaning for adults, the samples were fNIRS channels and for the neonates, the samples were combinations of several channels within the same neuroanatomical lobes.

Given the number of subjects as n_{par}, number of imaging sessions (finger tapping or task-free) as n_{ses} and number of cortical nodes as n_{node}, the number of samples $N = n_{par}n_{ses}n_{node}$. By this, we obtained 1200 samples for adult finger tapping sessions and 400 for resting-state sessions. For neonates, there were 184 samples in total.

For each node (or sample), its partial correlations with all other cortical nodes were calculated as features, respectively calculated with HbO, Hb and Hbt. Therefore, we obtained the input feature matrix $X \in \mathbb{R}^{N \times n_{node}}$. Convolutional kernels were calculated based on the Pearson correlations of HbO, Hb and Hbt, respectively. Such strategies for calculating features and kernels can be found previously in [230]. To match the dimensions of kernels and feature matrices, adjacency matrices of all sessions of all participants were concatenated on the diagonal (Fig. 4.4a), so that kernels $\in \mathbb{R}^{N \times N}$. For the multi-kernel models, kernels were applied to feature matrices of corresponding chromophores and all three chromophores were used. For mono-kernel GCN models, only one chromophore was applied.

The Pearson correlation coefficients between cortical nodes and thalamus calculated with fMRI were targets for prediction. We used leave-one-out validation (LOOV), where all samples of all sessions of one subject were left out during training. The models were built for classification and regression, respectively. For classification, the target fMRI connectivities were binarized using a threshold yielding two balanced classes. The connectivities with thalamus of two hemispheres were predicted separately (i.e., training two models with the same set of features but different targets). The performances of the models were measured using accuracy, area under receiver operating characteristic curves (AUC) and f1 scores. For regression, the actual values of targets were predicted, with testing errors measured by L1-losses. The model was trained for both task-free (i.e., resting state) and task-based (i.e., finger-tapping) data, separately. We also compared our multi-kernel and mono-kermel models with some commonly used machine learning methods, such as fully connected feedforward networks (ANN), which are the basic model of deep learning, and support vector machines (SVM), which are also widely adopted in many scenarios.

To improve the performance of GCN models, inter-subject connections (Fig. 4b) were added to the kernels. Two ways to calculate inter-subject connections were tested (Fig. 4.4c). The 1st one was Pearson correlations between all samples. The 2nd one was geometrical meaning channels from different subjects, but at the same location in the fNIRS montage that were related to a coefficient λ. Different choices of λ were tested. Also, considering that fNIRS data can be noisy, the models were trained and tested with noisy samples removed to see the robustness of the models against noise. The noise level of a sample was determined by its coefficient of variance (CV) of the raw optical density data of fNIRS from the corresponding cortical node.

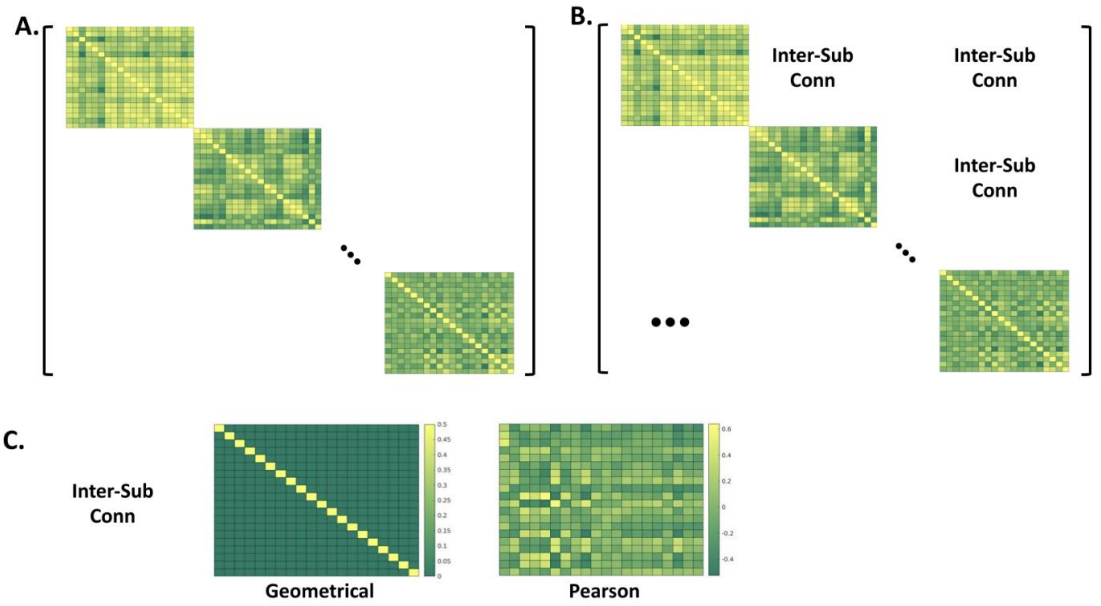

Figure 4.4: (a) An example of a concatenated adjacency matrix, serving as a kernel, with all participants' individual ones on the diagonal. One adjacency matrix of this kind was derived from data of one chromophore. (b) Concatenated adjacency matrix with added inter-subject connections, which would be replaced by matrices in Fig. 4c. (c) Two inter-subject connections tested in this study, which were geometrical (left, with a coefficient λ on the diagonal) and Pearson (right).

4.4 Results

4.4.1 Adult group

The classification and regression results for both the resting state and finger tapping sessions are shown in Fig. 4.5. GCN models had, in general, better performances compared with ANN and SVM. Compared to GCN models, SVM could have comparable AUC or f1 score for classification but lower accuracy, and higher L1-loss for regression, while ANN was better at classification (still with marginally higher loss than GCN), yet had lower accuracy, AUC and f1 score. Within GCN models, multi- or mono-kernel ones had comparable performances. As comparisons, fMRI features kernels and features were also calculated and applied for training GCN, yet the results were no better than using fNIRS based input.

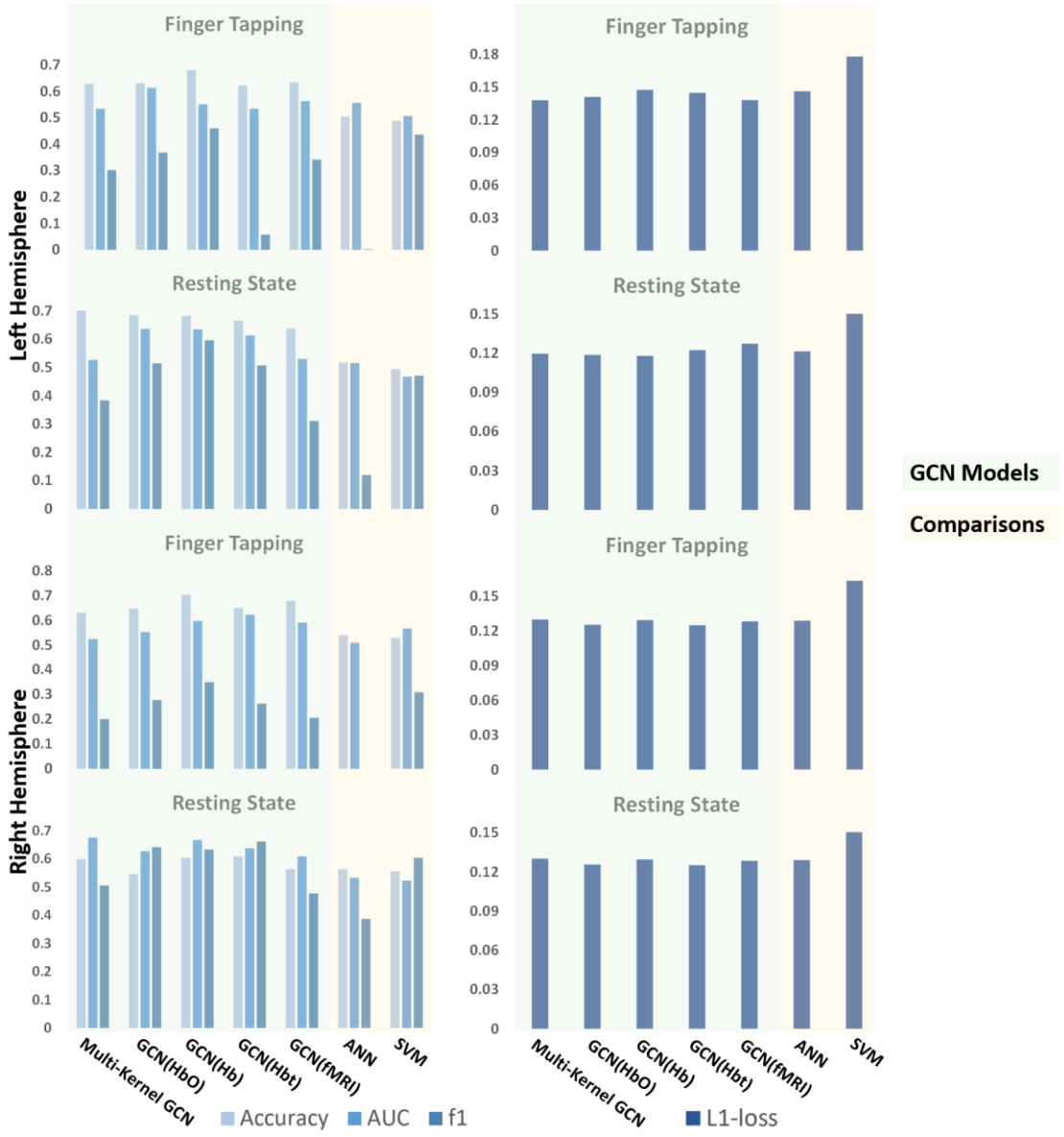

Figure 4.5: Results of classification (left panel) and regression (right panel) from finger tapping and resting state sessions.

With inter-subject connections, shown in Fig. 4.6, model performance was improved for both classification and regression. λ was kept at 0.5 for geometric connections. While Pearson connections did not always yield the best performance, the models were much improved geometric connections for all tasks. Also as shown in Table 4.3, the multi-kernel models especially benefited from geometric connections in terms of regression.

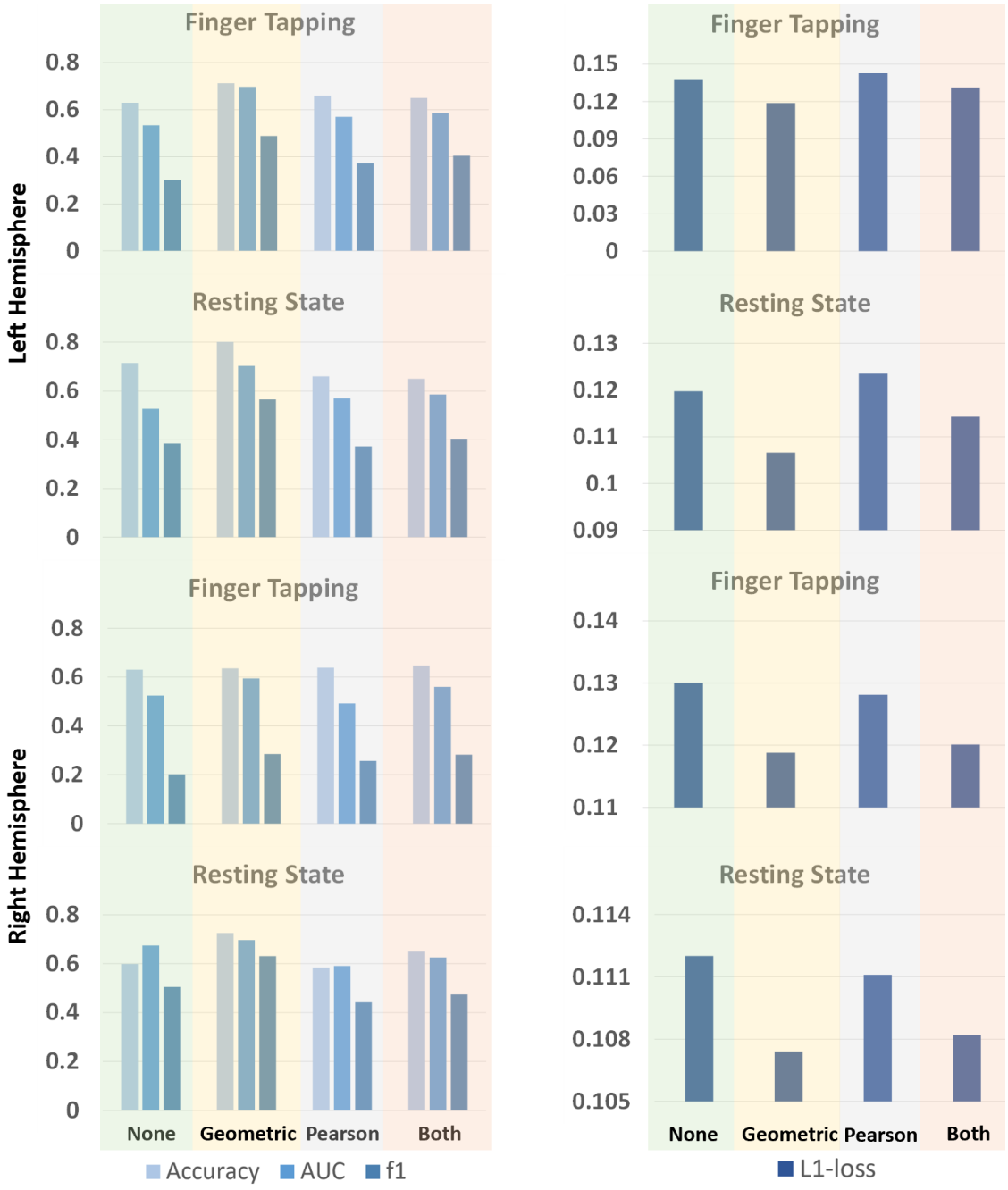

Figure 4.6: Performance of multi-kernel GCN models on classification (left panel) and regression (right panel) with inter-subject connections added to kernels. "Both" means geometric and Pearson connections were summed up then added to the kernels.

Table 4.3: Comparison between different GCN models with geometric kernels.

			Multi-Kernel GCN	**GCN (HbO)**	**GCN (Hb)**	**GCN (Hbt)**
Finger Tapping	**Cl**	**LH**				
		Accuracy	**0.7125**	0.7071	0.6933	0.7066
		AUC	**0.6971**	0.6626	0.6848	0.6733
		f1	0.4882	0.4672	0.5961	**0.6193**
		RH				
		Accuracy	0.6359	**0.7400**	0.7008	0.6950
		AUC	0.5948	**0.6670**	0.6362	0.6130
		f1	0.2847	**0.5007**	0.5006	0.4807
	Re	**LH**				
		L1-loss	**0.1187**	0.1347	0.1374	0.1222
		RH				
		L1-loss	**0.1188**	0.1320	0.1326	0.1196
Resting State	**Cl**	**LH**				
		Accuracy	**0.8050**	0.7675	0.7225	0.7325
		AUC	0.7032	**0.7800**	0.7217	0.7256
		f1	0.5657	**0.7116**	0.5939	0.6669
		RH				

		Accuracy	**0.7259**	0.6700	0.6600	0.6475
		AUC	0.6975	**0.7295**	0.7216	0.6552
		f1	0.6309	0.6761	**0.7064**	0.6619
	Re	**LH**				
		L1-loss	**0.1066**	0.1086	0.1230	0.1122
		RH				
		L1-loss	**0.1074**	0.1069	0.1111	0.1058

Note. Cl: classification, Re: regression.

To further examine the effects of the geometric connection coefficient λ, we tested a series of different values of it. The value of the coefficients yielding the best performances could vary based on the tasks (Fig. 4.7a and b), but usually fell into the range from 0.3 to 0.7. In Fig. 4.7c are significant linear correlations between true and predicted connectivities, providing yet another validation for our models.

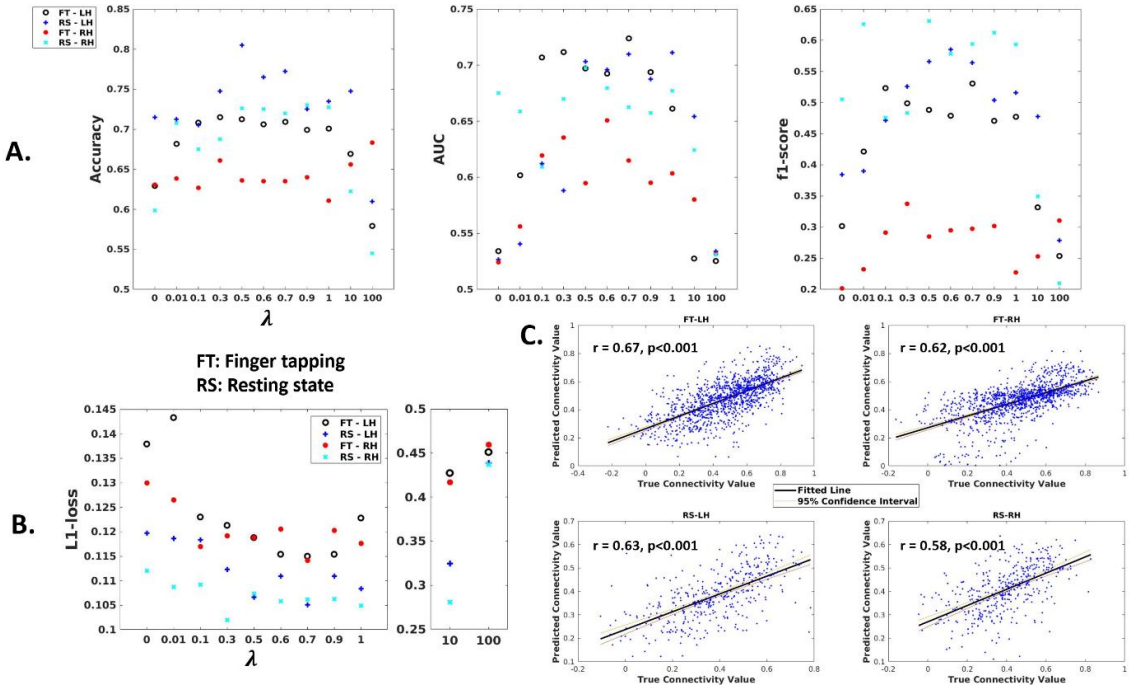

Figure 4.7: Change of performances of multi-kernel GCN models with geometric connection coefficients λ ranging from 0.01 to 100, measured for classification (a) and regression (b). (c) Linear correlations between true fMRI connectivity and predicted connectivity obtained from the regression models using λ with lowest L1-loss.

Since fNIRS signals can be noisy, we tested the models with noisy samples removed from training and testing datasets. 10%, 15%, and 20% of the noisiest samples were excluded, and thresholded by different values of CV. Removal of noisy samples did not yield better results (Table 4.4), for most of the tasks, which indicated the robustness of our models against noise.

Table 4.4: Performance of multi-kernel models with or without noisy samples removed.

			No Removal	**10% (CV>0.52)**	**15% (CV>0.51)**	**20% (CV>0.38)**
Finger Tapping		**LH**				
		Accuracy	0.7125	0.6987	0.7071	0.6846

	Cl	AUC	0.6971	0.6819	0.6626	0.6981
		f1-score	0.4882	0.4504	0.4672	0.4597
		RH				
		Accuracy	0.6359	0.6137	0.6481	0.5902
		AUC	0.5948	0.5959	0.6291	0.6104
		f1-score	0.2847	0.2620	0.2879	0.2306
	Re	**LH**				
		L1-loss	0.1187	0.1109	0.1129	0.1265
		RH				
		L1-loss	0.1188	0.1265	0.1135	0.1144
Resting		**LH**				
State		Accuracy	0.8050	0.8110	0.7602	0.7320
		AUC	0.7032	0.7170	0.7175	0.7465
	Cl	f1-score	0.5657	0.6657	0.5616	0.6358
		RH				
		Accuracy	0.7259	0.7160	0.7367	0.7062
		AUC	0.6975	0.7196	0.7450	0.7114
		f1-score	0.6309	0.6128	0.6753	0.6242
		LH				

	Re	L1-loss	0.1066	0.1015	0.1047	0.1101
		RH				
		L1-loss	0.1074	0.1047	0.1054	0.1053

4.4.2 Neonatal group

We also used task-free (i.e., resting state) neonatal fNIRS and fMRI data to train the models. As shown in Fig. 4.8a, GCN based models outperformed ANN and SVM, yet there were no advantages for multi-kernel methods. Though not as good as they performed on adult data, for regression, GCN models could yield a significant linear regression between predicted values and ground truths (Fig. 4.8b). Also, in Table 4.5, we found no improvement by applying inter-subject connections.

Table 4.5: Model performances with or without inter-subject connections.

	No inter-subject connections				**Geometric inter-subject connections, λ=0.5**			
	MultiKernel-GCN	**GCN(HbO)**	**GCN(Hb)**	**GCN(Hbt)**	**MultiKernel-GCN**	**GCN(HbO)**	**GCN(Hb)**	**GCN(Hbt)**
LH								
Accuracy	0.6141	0.6630	0.6702	0.6685	0.6032	0.6793	0.6902	0.6521
AUC	0.5067	0.6040	0.6538	0.5777	0.4943	0.6732	0.6538	0.6297
f1	0.0957	0.2703	0.3064	0.2622	0.0565	0.3965	0.3064	0.2420
RH								
Accuracy	0.6064	0.6413	0.6467	0.6522	0.6059	0.6576	0.6359	0.6630
AUC	0.5022	0.6708	0.6203	0.6509	0.5408	0.6483	0.5940	0.6283
f1	0.0899	0.3939	0.4563	0.3730	0.2241	0.4098	0.3894	0.3890
LH								
L1-loss	0.2081	0.1984	0.1821	0.1981	0.2115	0.2313	0.1900	0.1951
RH								

L1-loss	0.2081	0.1984	0.1821	0.1981	0.2115	0.2313	0.1684	0.1620

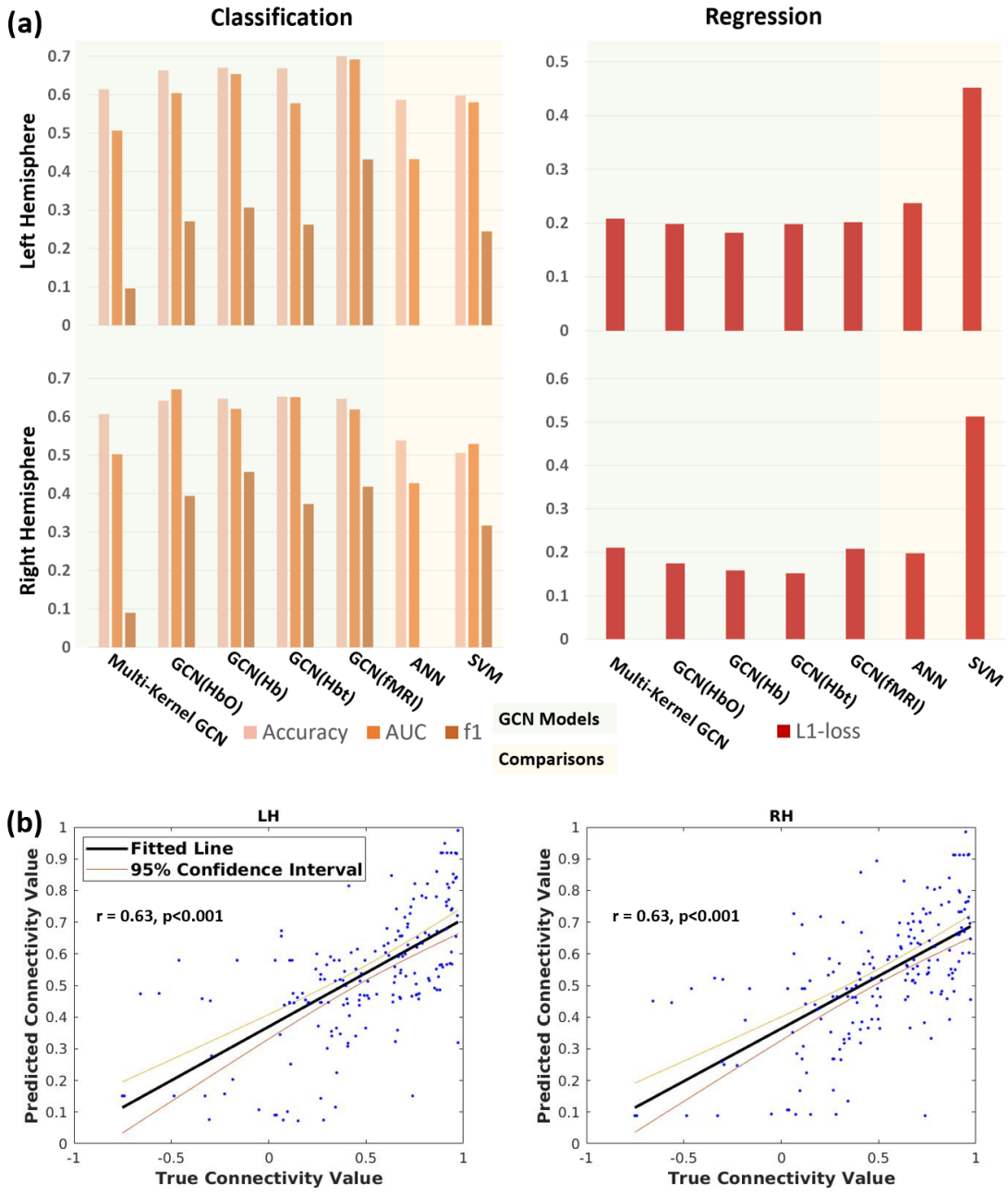

Figure 4.8: (a) Performance of machine learning models on the neonatal dataset. (b) Linear correlations between true fMRI connectivity and predicted connectivity obtained from regression models for the neonatal dataset.

4.5 Discussion

Despite the growing interest and involvement of fNIRS in clinical settings, even new fNIRS technology is still largely limited by the penetration depth and cannot offer critical information on subcortical areas. In this study, we proposed machine learning approaches using GCN models for predicting cortical-thalamic connectivity using cortical fNIRS data. The GCN models were examined on adult and neonatal populations, respectively, for either determining the existence of a connection (classification) or inferring the exact value of connectivity strength (regression). The performances of the models were mainly evaluated with accuracy, AUC and f1 scores for classification and L1-loss for regression. We showed that GCN models outperformed two conventional methods, ANN and SVM. Using multi-kernel strategy, combined with inter-subject connections within kernels, can further improve the results.

The strength of GCN models, compared to ANN and SVM, was robust in that when analyzing features of one sample, the features of its neighboring samples were taken into consideration, which made the models specifically suitable for studying brain networks. The brain is largely characterized by connectivity, ranging from individual neurons through synaptic connections to more broad widespread anatomical connectivity of short- and long-range cortical and subcortical areas [242]. Representations, or features, of brain regions can be dependent on each other through connectivity in various terms such as neurophysiology, biochemistry, etc. [26]. Yet, the representations manually chosen or extracted automatically with algorithms might not be sufficient to encode connectivity on their own. GCN models enable connectivity to be represented by multiplying the connectivity matrices on every level of the models, yielding latent features of samples fully embraced with connectivity information. This was especially true for the adult data, where cortical regions, as samples, were densely located around the sensory cortices, which potentially strengthened connectivity among them [98]. In addition, in our setup, features were calculated as partial correlations between one region and all others, which were already connectivity measurements. Yet, the performance with ANN was poor, indicating that full correlations, potentially containing extra information through indirect connections, could also be vital [230].

The multi-kernel strategy of GCN enabled us to take full advantage of three chromophores obtained from fNIRS and yielded better performances on some tasks, especially using regression. Though conventionally HbO and Hb signals are perfectly anti-correlated, and it was sufficient to report only one chromophore, recent developments pointed out some considerable heterogeneity amongst chromophores for adults and infants [244], [245]. While HbO is considered more sensitive to cerebral blood flow changes and activation induced changes [244], it is more susceptible to physiological noise than Hb [169]. In the current study, we considered the three chromophores to be complementary to each other, as HbO and Hb measured different molecules and Hbt corresponded more to blood volume. Yet this could also be a limitation of the study, whereby overlapping information could still be shared by the three chromophores leading to redundant input. It could explain that for some tasks, multi-kernel models were not as good as mono-kernel ones.

Using short channels to remove superficial physiological noise is becoming a standard method for fNIRS data collection on adults. However, we did not include short channels in our protocols, which can be considered a limitation. In fact, results of Hb, which is less sensitive to systemic physiology [169], showed better performances than HbO and Hbt on many tasks, which could possibly be explained by the lack of short channels. Yet, the models were still shown to be robust to samples with higher CV, which was more related to background noise, system drift and motion artifacts. In neonates, since scalps and skulls are thinner than adults, superficial physiology might take up less of the portion of the whole signal. Also, to use short channels on newborns, their feasible separation would be too short (<5 mm) to be implemented on most available fNIRS caps [75].

The adult participants were asked to tap with their right hands only, therefore, it was likely to have laterality issues with different activation patterns between two hemispheres. Such issues were not examined, but we saw no consistent hemispheric differences from our classification and regression results. This potentially demonstrated that our models would work regardless of laterality.

For both classification and regression, results from the neonatal data were not as optimal as in adults. This was possibly due to the limitations of this study concerning neonatal data

acquisition. Namely, fNIRS and fMRI date were not collected simultaneously for neonates. Temporal dynamics of BOLD signals and functional connectivity has been documented before [208], [209]. Plus, the awake status of neonates was not controlled during the two scans using objective measures. The second limitation was that the duration of the neonatal fMRI scans was potentially short for robust calculations of functional correlations [246]. In addition, the models were limited by the sample size for both adults and neonates. The samples were divided only into training and testing sets. However, including a third validation set, which was not used for training or testing, could provide a clearer assessment of model performance. Additionally, the variations in model-evaluating metrics were not recorded, which limits the ability to statistically compare the models.

Also in the neonatal group, the inter-subject connections failed to improve model performances. The inter-subject connection was based on the functional similarity amongst the data collected from different sessions and different participants. Additionally, the neonates recruited for this study were from the NICU and were receiving clinical care, which could increase the variability within the whole population. Despite the limitations on neonatal data, our models still achieved binary classification results better than random, and strong linear correlations between the ground truths and predicted values for regression.

The current study results are very promising for fNIRS to be used as a bedside monitoring tool. These results could be further validated by having longer fMRI scanning runs, including larger normative samples, and objective measures of sleep/awake state (i.e., electroencephalography). Additionally, a better understanding of alterations in functional connectivity measures in relation to brain health and outcomes in critically ill populations would further the clinical use of fNIRS as a biomarker.

Chapter 5

5 Conclusions and future directions

This chapter revisits the overall goals of the thesis and generalizes important findings and the significance of each chapter. Limitations of the whole thesis and of each chapter are discussed along with potential solutions. Future directions to further develop fNIRS for clinical applications are also discussed.

5.1 Research objectives

Neonatal brain injury is a serious threat to the long-term health of newborns. Brain injury in the neonatal period is associated with high rates of mortality and affect neurodevelopmental outcomes in survivors, including cerebral palsy, or other cognitive, visual, or language deficits [1]. Neonatal brain injury can happen to both term and preterm born neonates [15], [247]. For preterm born neonates, intraventricular hemorrhage (IVH) is a common complication that usually begins with a mechanical disruption to the germinal matrix then bleeds within or around ventricular systems. The early development of the brain can be seriously affected by IVH. The germinal matrix contains precursor cells of neurons and glia. Hemorrhage can lead to inflammations and fibrosis. Sequentially, IVH is also associated with other conditions, such as posthemorrhagic ventricular dilatation, periventricular hemorrhagic infarction and periventricular leukomalacia, which can damage the white matter and disturb the maturation of neuronal fibres [24], [25], [26], [27]. For term born infants, hypoxic ischemic encephalopathy (HIE) is a major neurological insult that typically results from hypoxia (i.e., birth asphyxia), which leads to inflammation, excitotoxicity, oxidative stress, and eventually cell death [16]. HIE injury can appear in various areas including thalamus, basal ganglia, and watershed areas of white matter. The prevalence of HIE is recently estimated to be 0.01% in the United States amongst term-born infants [33]; yet, the incidence is much higher in developing countries [3].

Current clinical tools for diagnosing brain injury rely on imaging techniques, such as cranial ultrasound (cUS) and magnetic resonance imaging (MRI). Major disadvantages of cUS include that it cannot identify abnormalities in cerebral cortex, or diffusive injury

patterns in white matter [36]. Further, cUS cannot monitor the development of injury continuously to capture ventricular dilatation or white matter cysts and infarctions, for prompt interventions. cUS is not commonly used for HIE diagnosis as some abnormal patterns identifiable to cUS take days to develop. The optimal timing for initiating treatment (therapeutic hypothermia) is shortly after birth on the first day of life [40]. While MRI is more powerful in identifying injury patterns, it is mostly limited by its accessibility to newborns, cost and sensitivity to motion.

Functional near-infrared spectroscopy (fNIRS) is an emerging technique that could be an alternative or complimentary tool for monitoring neonatal brain injury. As an optical measurement, fNIRS is non-invasive, radiation-free, and compared to cUS and MRI, it is fairly resistant to motion, cost friendly, easy to use and accessible in the neonatal intensive care unit (NICU) at the bedside. fNIRS measures concentration changes of oxygenated hemoglobin (HbO) and deoxygenated hemoglobin (Hb). Numerous studies have shown that alterations in cerebral hemodynamics related to neonatal brain injury can be picked up by NIRS [188], [248], [249]. In addition, resting-state functional connectivity (RSFC) derived from either functional MRI (fMRI) or fNIRS data shows differences between infants with brain injury and healthy controls, and associations with severity of the injury, indicating RSFC features can be potential biomarkers for characterizing the injury [49], [122], [123], [126], [132]. RSFC features are also used with machine learning based methods for automated diagnosis and identification of new markers [124], [132], [147], [193]. Therefore, it is believed that a combination of fNIRS and RSFC can be a promising innovative approach to monitoring neonatal brain injury.

However, a major drawback of fNIRS is that it cannot provide information on deep brain regions, such as the thalamus, which is involved within several key functional networks, due to poor penetration depth of near-infrared light. A study from Liu et al. [228] demonstrated that it is possible to use computational methods to predict deep brain activity by cortical fNIRS recordings. Yet the models in this previous study were subject-dependent and were trained on a small sample. Another gap in the knowledge base is that though fNIRS and fMRI are comparable in adults and children [51], [106], [107], [166], [205], the

two modalities have rarely been studied in newborns, especially those with brain injuries who may have altered cerebral hemodynamics [245].

Therefore, the general goal of this research was to test the potential of fNIRS as a bedside neuroimaging tool for monitoring neonatal brain activity and identifying biomarkers for early brain injury in order to extend the research and clinical use of fNIRS by addressing major drawbacks of the technology. RSFC obtained from fNIRS will be examined and analyzed to characterize the injury. To be more specific, there were three objectives under the overall goal:

1. To examine RSFC obtained from fNIRS in a group of preterm born neonates with IVH and whether RSFC patterns of fNIRS can distinguish between neonates with and without IVH.

2. The RSFC derived from fNIRS in a cohort of full-term neonates with HIE will be investigated. Graph theory metrics computed from fNIRS RSFC will then be analyzed to examine between newborns with HIE and control subjects.

3. To ascertain whether a predictive model based on machine learning can be used to predict cortico-thalamic connectivity using cortical connectivity.

5.2 Summary of findings

5.2.1 Altered functional connectivity in neonates with IVH

This chapter examined RSFC obtained from fNIRS in a group of preterm born neonates with IVH by comparing it with fMRI, which was considered as ground truth in this study. Also, it was tested whether fNIRS RSFC patterns can distinguish between IVH infants and healthy controls. Lastly, whether RSFC patterns are associated with severity of IVH was also assessed. Sixteen very preterm born neonates with IVH of various grades were scanned with fMRI and fNIRS at term equivalent age (TEA). Fifteen healthy newborns were scanned with fNIRS only. Correlation-based connectivity maps of IVH infants were compared between fNIRS and fMRI using Euclidean and Jaccard distances to measure how similar the modalities were in a global sense. The severity of IVH in relation to fNIRS-

RSFC strength was examined using generalized linear models. Only large- and positive-weighted connections were kept when achieving a certain level of sparsity ranging from 0.2 to 0.4. At a sparsity level of 0.38, with both weighted and binarized maps, and for both HbO and Hb maps, the least Euclidean and Jaccard distances were observed, indicating the most similarity between RSFC maps from fNIRS and fMRI. At this level of sparsity, some individual connections also showed good correspondence between the two modalities. Subsequently, the whole population was separated into 3 groups: healthy controls, mild/moderate IVH (grade I and II) and severe IVH (grade III and IV). It is also shown that, at TEA, connectivity strength was the lowest in healthy newborns, then preterm infants with mild IVH, while infants with moderate/severe IVH have the strongest, on both HbO and Hb maps. The differences between groups are tested to be significant either. In general, fNIRS yielded comprehensive RSFC maps and revealed distinct RSFC patterns between preterm infants with IVH and healthy newborns, showing its potential to characterize brain injury.

5.2.2 Altered functional connectivity within neonates with HIE

This chapter tested whether RSFC obtained with fNIRS from a group of term-born neonates with HIE post TH and rewarming is feasible. And graph theory metrics calculated from fNIRS RSFC will be tested for whether HIE infants and controls can be separated. Twenty-one term-born neonates with HIE were enrolled. Twenty healthy term-born infants were recruited from the MBCU with a birth GA of 39.08, and fNIRS scans were performed within 48 hours of life. Firstly, fNIRS RSFC was compared to RSFC fMRI to determine whether similar findings would be obtained from the two modalities. The study also investigated the association between RSFC obtained from both fNIRS and fMRI with the volumes of grey and white matter based on structural MRI. This was done to further illustrate the comparability between fNIRS and MRI. Euclidean and Jaccard distances were used to compare fNIRS and fMRI connectivity maps with different levels of sparsity ranging from 0.2 to 0.46. RSFC was associated with increased trends towards larger grey or white matter volumes. HbO connectivity also showed significant positive associations with grey and white matter volumes. Hb and fMRI RSFC also demonstrated trends towards positive associations with volumetric growth. This further demonstrated that fNIRS- and

fMRI- based connectivities were comparable to each other. An analysis was conducted on fNIRS-derived RSFC data, comparing term-born neonates with HIE to healthy controls using graph theory metrics. The findings revealed that the HIE group exhibited notably heightened clustering coefficient, network efficiency, and modularity compared to healthy newborns. However, there was lower consistency within the HIE group, suggesting that newborns affected by HIE demonstrated increased connectivity within functional networks, but the differences in injury patterns could possibly explain variability among individuals. Support vector machine (SVM) was applied to distinguish between the HIE and healthy newborn data, using nodal connectivity features. Through 4-fold cross-validation, the highest achievable accuracy and area under the receiver operating characteristic curve (AUC) were reached. In general, we showed that fNIRS RSFC is comparable to fMRI and can be a potential indicator of brain health HIE in neonates.

5.2.3 Predicting cortico-thalamic connectivity from cortical connectivity

fNIRS is limited to measuring cortical hemodynamics and cannot capture information from the subcortices. To overcome this limitation, a computational approach was proposed in this thesis to predict cortical-thalamic functional connectivity using cortical fNIRS data. Specifically, a predictive model known as the graph convolutional network (GCN), a variant of the convolutional network, was utilized. In this model, samples are structured as networks, allowing for the calculation of high-level features based on the geometrical relationships within the network.

The GCN models were applied to two datasets obtained from healthy adults and neonates with early brain injuries. Each dataset included fNIRS connectivity data as inputs to the predictive models, with the connectivity of fMRI serving as the training targets. Healthy adult participants and thirty-seven neonatal participants with HIE and IVH were tested.

The GCN models were trained using individual fNIRS channels as samples, employing Pearson correlations among channels to construct the network and partial correlations between one channel and all others as features. The results were validated using fMRI cortico-thalamic connectivity data, with one subject's data left out for validation.

The performance of the GCN models was compared with feedforward fully connected artificial neural networks (ANN) and SVM for both classification (predicting binarized connections) and regression (predicting exact connection values). Evaluation metrics included accuracy, AUC, f1 score for classification, and L1-loss for regression. The study demonstrated that GCN models outperform ANN and SVM for both regression and classification on both adult and neonatal datasets, exhibiting higher accuracy, AUC, f1 scores, and lower L1-loss.

Multi-kernel GCN models, which can utilize all three chromophores of fNIRS, also showed improved performance compared to models using only one chromophore. Additionally, adding inter-subject connections enhanced model performance. Moreover, the robustness of GCN models against noise in fNIRS time series was tested by removing noisy channels, which showed no significant changes in model performance. Overall, the study highlights the potential of computational methods to predict deep brain connectivity, thereby extending the utility of fNIRS for clinical applications.

5.3 Limitations

5.3.1 Neonatal data

Chapters 2-4 all involved neonatal datasets from infants in NICU with brain injury, collected with the same protocol. Therefore, some limitations are shared among the chapters.

There is a disparity between fNIRS and fMRI RSFC when comparing these two modalities, and predicting subcortical connectivity produced poorer results in neonates compared to adults. A few possible reasons for this include measurement errors that can occur during data collection, whereby optodes lose contact between probes and skin, which are rather common in fNIRS studies in infants [152], [155], [164]. This is especially the case when whole-brain coverage is implemented whereby a cap holding all probes must be used, yet may not fit perfectly on the infants' heads, instead of only one or two channels, which can be attached to skin. Plus during data collection infants are laying supine in their incubators or in their caregiver's arms, which could further worsen optode contact, especially in the

occipital region where probes cannot keep perpendicular to the scalp. Also, movement can be an issue for both fNIRS and fMRI acquisition as the neonates are not sedated and are not always asleep during the limited time window for data collection (i.e., recording between feeds or handling). Secondly, discrepancies may have occurred due to inherent differences in the scanning protocols for fNIRS and fMRI. The two modalities could not be obtained simultaneously for neonates due to several reasons. Namely, acquisition of fNIRS during fMRI scanning would add time for the neonates to be away from the unit, posing some risks to their care. Additionally, the duration of the fMRI scanning sequence was relatively short. However, this was also to minimize the overall scan time as the neonates also had clinical sequences collected during MRI. The fMRI protocol was tested in an adult participant before scanning newborns. Though functional networks were identified for the adult, ideally it would have been assessed in a healthy infant. However, recruiting and testing healthy newborns in the first week of life on the same clinical scanner would pose many challenges. Thirdly, the localization of the fNIRS probes was not precise in MRI space. Therefore, an atlas-based analysis was applied where fNIRS channels or fMRI voxels within the same lobes were averaged, leading to some within-lobe discrepancies being potentially overlooked. Fourthly, not every participant was scanned with both fNIRS and fMRI. Given the timing of the MRI scans, some families would only consent to the fNIRS component of the study. This yielded even smaller sample size for comparing the two modalities, undermining the power of statistical analysis on the sample.

There were also some cohort-specific limitations. Among IVH infants, certain subjects underwent neurosurgical interventions to divert cerebrospinal fluid in cases of severe IVH and ventricular dilatation. These interventions could impact overall brain development and were not controlled in the analysis. Regarding HIE infants, while most of the participants with HIE were scanned after TH and rewarming, two infants had only mild HIE and were not cooled. Additionally, the neonatal analysis was generally constrained by a small sample size.

5.3.2 Adult data

In adults, short-distance channels are frequently implemented in fNIRS studies to assess extracerebral artifacts and improve signal quality. Yet they were not used in this study due to inaccessibility of the equipment. Also, for the finger-tapping portion of the protocol, the participants were asked to tap with the fingers on the right hand only; however, some of the participants were left-handed. Left-handed individuals are more likely to activate the cortex bilaterally [250], which could have influenced our dataset. However, there were no consistent hemispheric differences within the classification and regression results, potentially indicating that the predictive models perform well regardless of laterality. Another potential limitation of the multi-kernel GCN model, which has not been tested before, is the assumption that the three chromophores are completely independent of each other. However, in practice, fNIRS chromophores collected simultaneously in the same individual are always correlated to some degree. Therefore, the model relies on integrating the three chromophores and extracting distinct representations from them. In certain tasks, the multi-kernel model demonstrated superior performance compared to a single-kernel model, suggesting that it may not consistently integrate all the information from every chromophore effectively. Also, the whole dataset was separated into training and validation sets, but not testing sets, the performance potentially was in turn potentially biased towards the validation set. Yet, considering the sample size and the complexity of the model, an extra testing set could have undermined the representational power of the models since they would have been trained with even less data.

5.4 Future directions

The results of this study show the potential promise of fNIRS combined with RSFC as an indicator for characterizing neonatal brain injury at the bedside. Based on the current results, several directions for improving the distinguishing power of the models can be taken, as well as identifying new RSFC-based indicators and exploring more clinical and research applications.

Addressing certain limitations in fNIRS data collection for neonates can be challenging. Specifically, the utilization of short-distance channels is relatively uncommon in neonatal studies. This is because placing short-distance channels alongside regular channels that are already very close in close proximity is ineffective, given the smaller surface area of the head and the thin scalp in neonates [75]. Other approaches for addressing physiological noise could be potentially applied in future studies, using physiological monitoring and use these measurements to improve signal decomposition. Additionally, better characterization the of the sleep/wake states of the neonatal participants could be documented in greater detail. The inclusion of EEG in these protocols would also help to better characterize sleep/wake states. Further, the spatial correspondence between fNIRS and fMRI could be improved by introducing fiducial markers on the fNIRS caps during the MRI scans.

Other indicators of neonatal brain injury based on RSFC could be explored, such as dynamic functional connectivity (DFC). DFC captures the constant reconfiguration of brain networks and adaptive adjustments in response to internal and external stimuli [251]. Previously, DFC has been introduced to study early development of brain on both term and preterm born infants. Franca et al. [252] explored state transitions (e.g., fluctuations in neural activity, connectivity patterns) using fMRI and examined the variations in brain dynamics between term-born and preterm-born infants. Wen et al. [253] reported increased temporal variability in infants from birth to 2 years of age, indicating the exponential functional flexibility of the human brain during development. Studies from Zhang and Zhu [134], and Li et al. [254] also demonstrated the feasibility of using fNIRS for extracting the dominant functional networks based on RSFC dynamics.

DFC analysis was applied to the neonatal datasets used in this thesis and provided promising results. Utilizing amplitude of low frequency fluctuations (ALFF) and standard deviations (SD) as temporal variance metrics in a DFC model, the three groups of participants (IVH, HIE, and healthy newborns) exhibited distinct developmental trajectories (Fig. 5.1). Therefore, DFC-based measurements could be promising indicators for charactering neonatal brain injury in future work.

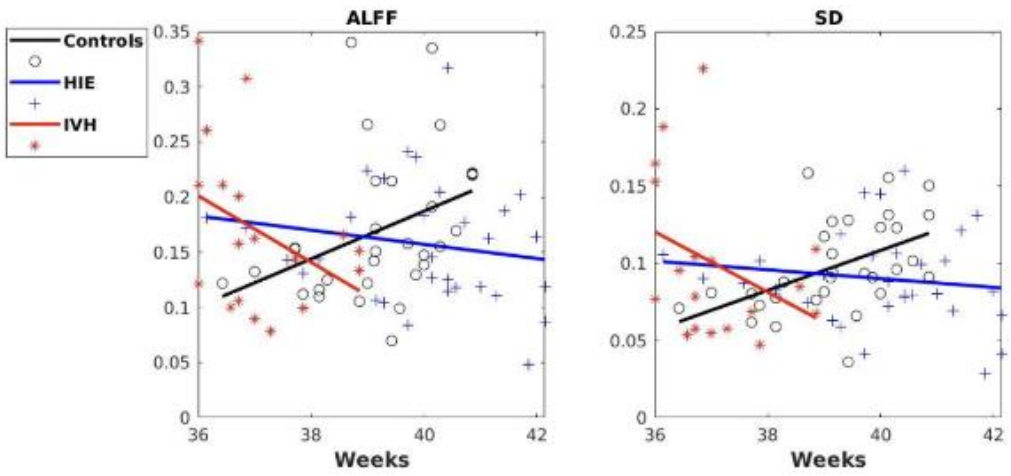

Figure 5.1: Temporal variance metrics on infants during early days of life. X-axis are the postmenstrual age at the time of the fNIRS scan.

In this work, it was demonstrated that machine learning methods can be used for distinguishing functional connectivity data in neonates with brain injury compared to healthy controls and predicting subcortical connectivity. However, considering that the accuracy was generally about 70-80%, there is still room for improvement. The predictive models could potentially be modified using recent developments in deep learning. One deep learning method named transformer is attracting increasing attention partially due to the popularity of ChatGPT (generative pre-trained transformer). Transformer is based on recurrent neural networks, which are specifically designed for processing time series of data. Unlike traditional recurrent models, transformers utilize attention mechanisms that enable the model to assign importance to sequential inputs, replicating human cognitive attention. However, transformers lack the recurrent architecture, resulting in faster training times [255]. Transformer networks have been used on neuroimaging data for diagnosis [256], learning brain dynamics [257], [258], and optimizing image interpretation [259]. A recent work from Yun et al. [260] also combined transformer with GCN to model the dynamics of networks, which is another promising option for the data in this thesis.

In upcoming research studies, a broader dataset will be incorporated regardless of the specific analytical approaches being employed. Presently, data collection efforts in the NICU and the mother baby care unit are ongoing. The aim is to include more participants with IVH, HIE, and healthy controls to enhance the statistical robustness of the analyses,

along with individuals from other relevant cohorts. Apart from IVH and HIE, various other neonatal brain complications, such as meningitis and hypoglycemia, which are anticipated to affect cerebral hemodynamics and could also potentially be characterized using fNIRS. It is envisioned that multi-class classification tasks could be explored by inputting data from all cohorts into machine learning models.

5.5 Conclusions

In summary, this research highlights the feasibility of leveraging fNIRS technology to characterize neonatal brain injury through the lens of RSFC, underscoring its potential as an innovative bedside monitoring tool for newborns facing neurological challenges. Furthermore, it suggests that computational methodologies could mitigate one of the primary limitations of fNIRS—penetration depth—by enabling the prediction of subcortical connectivity. This advancement has the potential to significantly broaden the applicability of fNIRS in both research and clinical settings.

References

[1] D. Webster, “Neonatal brain injury,” in *Neonatal Intensive Care Nursing: Third Edition*, vol. 19, no. 4, 2019, pp. 351–373. doi: 10.4324/9781315150451-17.

[2] J. J. Volpe, “Brain injury in premature infants: a complex amalgam of destructive and developmental disturbances,” *The Lancet Neurology*, vol. 8, no. 1. pp. 110–124, Jan. 2009. doi: 10.1016/S1474-4422(08)70294-1.

[3] J. J. Kurinczuk, M. White-Koning, and N. Badawi, “Epidemiology of neonatal encephalopathy and hypoxic–ischaemic encephalopathy,” *Early Hum. Dev.*, vol. 86, no. 6, pp. 329–338, Jun. 2010, doi: 10.1016/J.EARLHUMDEV.2010.05.010.

[4] J. E. Lawn, A. C. C. Lee, M. Kinney, L. Sibley, W. A. Carlo, V. K. Paul, R. Pattinson, and G. L. Darmstadt, “Two million intrapartum-related stillbirths and neonatal deaths: Where, why, and what can be done?,” in *International Journal of Gynecology and Obstetrics*, John Wiley and Sons Ltd, 2009. doi: 10.1016/j.ijgo.2009.07.016.

[5] C. Siffel, K. D. Kistler, and S. P. Sarda, “Global incidence of intraventricular hemorrhage among extremely preterm infants: A systematic literature review,” *Journal of Perinatal Medicine*, vol. 49, no. 9. De Gruyter Open Ltd, pp. 1017–1026, Nov. 01, 2021. doi: 10.1515/jpm-2020-0331.

[6] M. J. Herrmann, J. B. M. Langer, C. Jacob, A. C. Ehlis, and A. J. Fallgatter, “Reduced prefrontal oxygenation in alzheimer disease during verbal fluency tasks,” *Am. J. Geriatr. Psychiatry*, vol. 16, no. 2, pp. 125–135, Feb. 2008, doi: 10.1097/JGP.0b013e3180cc1fbc.

[7] E. A. Christian, D. L. Jin, F. Attenello, T. Wen, S. Cen, W. J. Mack, M. D. Krieger, and J. G. McComb, “Trends in hospitalization of preterm infants with intraventricular hemorrhage and hydrocephalus in the United States, 2000-2010,” *Journal of Neurosurgery: Pediatrics*, vol. 17, no. 3. American Association of Neurological Surgeons, pp. 260–269, Mar. 01, 2016. doi: 10.3171/2015.7.PEDS15140.

[8] S. P. Miller, D. M. Ferriero, C. Leonard, R. Piecuch, D. V. Glidden, J. C. Partridge, M. Perez, P. Mukherjee, D. B. Vigneron, and A. J. Barkovich, “Early Brain Injury in Premature Newborns Detected with Magnetic Resonance Imaging is Associated with Adverse Early Neurodevelopmental Outcome,” *J. Pediatr.*, vol. 147, no. 5, pp. 609–616, Nov. 2005, doi: 10.1016/j.jpeds.2005.06.033.

[9] L. Treluyer, M. Chevallier, P. H. Jarreau, O. Baud, V. Benhammou, C. Gire, L. Marchand-Martin, S. Marret, V. Pierrat, P. Y. Ancel, and H. Torchin, “Intraventricular hemorrhage in very preterm children: Mortality and neurodevelopment at age 5,” *Pediatrics*, vol. 151, no. 4, 2023, doi: 10.1542/peds.2022-059138.

[10] J. Park, S. H. Park, C. Kim, S. J. Yoon, J. H. Lim, J. H. Han, J. E. Shin, H. S. Eun, M. S. Park, and S. M. Lee, “Growth and developmental outcomes of infants with hypoxic ischemic encephalopathy,” *Sci. Rep.*, vol. 13, no. 1, Dec. 2023, doi:

10.1038/s41598-023-50187-0.

[11] M. Finder, G. B. Boylan, D. Twomey, C. Ahearne, D. M. Murray, and B. Hallberg, “Two-Year Neurodevelopmental Outcomes after Mild Hypoxic Ischemic Encephalopathy in the Era of Therapeutic Hypothermia,” *JAMA Pediatr.*, vol. 174, no. 1, pp. 48–55, Jan. 2020, doi: 10.1001/jamapediatrics.2019.4011.

[12] A. Ramirez, S. Peyvandi, S. Cox, D. Gano, D. Xu, O. Tymofiyeva, and P. S. McQuillen, “Neonatal brain injury influences structural connectivity and childhood functional outcomes,” *PLoS One*, vol. 17, no. 1 January, Jan. 2022, doi: 10.1371/journal.pone.0262310.

[13] D. Azzopardi, B. Strohm, N. Marlow, P. Brocklehurst, A. Deierl, O. Eddama, J. Goodwin, H. L. Halliday, E. Juszczak, O. Kapellou, M. Levene, L. Linsell, O. Omar, M. Thoresen, N. Tusor, A. Whitelaw, and A. D. Edwards, “Effects of Hypothermia for Perinatal Asphyxia on Childhood Outcomes,” *N. Engl. J. Med.*, vol. 371, no. 2, pp. 140–149, Jul. 2014, doi: 10.1056/NEJMOA1315788/SUPPL_FILE/NEJMOA1315788_DISCLOSURES.PDF.

[14] S. Shankaran, A. Pappas, S. A. McDonald, B. R. Vohr, S. R. Hintz, K. Yolton, K. E. Gustafson, T. M. Leach, C. Green, R. Bara, C. M. P. Huitema, R. A. Ehrenkranz, J. E. Tyson, A. Das, J. Hammond, M. Peralta-Carcelen, P. W. Evans, R. J. Heyne, D. E. Wilson-Costello, Y. E. Vaucher, C. R. Bauer, A. M. Dusick, I. Adams-Chapman, R. F. Goldstein, R. Guillet, L.-A. Papile, and R. D. Higgins, “Childhood Outcomes after Hypothermia for Neonatal Encephalopathy,” *N. Engl. J. Med.*, vol. 366, no. 22, pp. 2085–2092, May 2012, doi: 10.1056/NEJMOA1112066/SUPPL_FILE/NEJMOA1112066_DISCLOSURES.PDF.

[15] N. Badawi, J. J. Kurinczuk, J. M. Keogh, L. M. Alessandri, F. O’Sullivan, P. R. Burton, P. J. Pemberton, and F. J. Stanley, “Antepartum risk factors for newborn encephalopathy: The Western Australian case-control study,” *Br. Med. J.*, vol. 317, no. 7172, pp. 1549–1553, 1998, doi: 10.1136/bmj.317.7172.1549.

[16] M. Douglas-Escobar and M. D. Weiss, “Hypoxic-Ischemic Encephalopathy: A Review for the Clinician,” *JAMA Pediatr.*, vol. 169, no. 4, pp. 397–403, Apr. 2015, doi: 10.1001/JAMAPEDIATRICS.2014.3269.

[17] F. Cowan, M. Rutherford, F. Groenendaal, P. Eken, E. Mercuri, G. M. Bydder, L. C. Meiners, L. M. S. Dubowitz, and L. S. De Vries, “Origin and timing of brain lesions in term infants with neonatal encephalopathy,” *Lancet*, vol. 361, no. 9359, pp. 736–742, Mar. 2003, doi: 10.1016/S0140-6736(03)12658-X.

[18] R. C. McKinstry, J. H. Miller, A. Z. Snyder, A. Mathur, G. L. Schefft, C. R. Almli, J. S. Shimony, S. I. Shiran, and J. J. Neil, “A prospective, longitudinal diffusion tensor imaging study of brain injury in newborns,” *Neurology*, vol. 59, no. 6, pp. 824–833, Sep. 2002, doi: 10.1212/WNL.59.6.824.

[19] C. E. J. Parmentier, L. S. de Vries, and F. Groenendaal, “Magnetic Resonance Imaging in (Near-)Term Infants with Hypoxic-Ischemic Encephalopathy,” *Diagnostics*, vol. 12, no. 3, p. 645, Mar. 2022, doi:

10.3390/DIAGNOSTICS12030645.

[20] P. Ballabh, “Pathogenesis and Prevention of Intraventricular Hemorrhage,” *Clin. Perinatol.*, vol. 41, no. 1, pp. 47–67, Mar. 2014, doi: 10.1016/j.clp.2013.09.007.

[21] S. Al-Abdi and M. Al-Aamri, “A systematic review and meta-analysis of the timing of early intraventricular hemorrhage in preterm neonates: Clinical and research implications,” *J. Clin. Neonatol.*, vol. 3, no. 2, p. 76, 2014, doi: 10.4103/2249-4847.134674.

[22] L. A. Papile, J. Burstein, R. Burstein, and H. Koffler, “Incidence and evolution of subependymal and intraventricular hemorrhage: A study of infants with birth weights less than 1,500 gm,” *J. Pediatr.*, vol. 92, no. 4, pp. 529–534, Apr. 1978, doi: 10.1016/S0022-3476(78)80282-0.

[23] A. S. Morgan, M. Mendonça, N. Thiele, and A. L. David, “Management and outcomes of extreme preterm birth,” *BMJ*, vol. 376, Jan. 2022, doi: 10.1136/bmj-2021-055924.

[24] J. J. Volpe, “Dysmaturation of Premature Brain: Importance, Cellular Mechanisms, and Potential Interventions,” *Pediatr. Neurol.*, vol. 95, pp. 42–66, Jun. 2019, doi: 10.1016/J.PEDIATRNEUROL.2019.02.016.

[25] J. J. Volpe, H. C. Kinney, F. E. Jensen, and P. A. Rosenberg, “The developing oligodendrocyte: key cellular target in brain injury in the premature infant,” *Int. J. Dev. Neurosci.*, vol. 29, no. 4, pp. 423–440, Jun. 2011, doi: 10.1016/J.IJDEVNEU.2011.02.012.

[26] J. J. Volpe, T. E. Inder, B. T. Darras, L. S. de Vries, A. J. du Plessis, J. J. Neil, and J. M. Perlman, “Volpe’s Neurology of the Newborn,” *Volpe’s Neurol. Newborn*, pp. 1–1224, Jan. 2018, doi: 10.1016/C2010-0-68825-0.

[27] L. S. De Vries, A. M. Roelants-van Rijn, K. J. Rademaker, I. C. Van Haastert, F. J. Beek, and F. Groenendaal, “Unilateral parenchymal haemorrhagic infarction in the preterm infant,” *European Journal of Paediatric Neurology*, vol. 5, no. 4. W.B. Saunders Ltd, pp. 139–149, 2001. doi: 10.1053/ejpn.2001.0494.

[28] R. L. Sherlock, P. J. Anderson, L. W. Doyle, C. Callanan, E. Carse, D. Casalaz, M. P. Charlton, N. Davis, J. Duff, G. Ford, S. Fraser, M. Hayes, M. Kaimakamis, E. Kelly, G. Opie, A. Watkins, H. Woods, and V. Yu, “Neurodevelopmental sequelae of intraventricular haemorrhage at 8 years of age in a regional cohort of ELBW/very preterm infants,” *Early Hum. Dev.*, vol. 81, no. 11, pp. 909–916, Nov. 2005, doi: 10.1016/j.earlhumdev.2005.07.007.

[29] I. Adams-Chapman, N. I. Hansen, B. J. Stoll, and R. Higgins, “Neurodevelopmental outcome of extremely low birth weight infants with posthemorrhagic hydrocephalus requiring shunt insertion,” *Pediatrics*, vol. 121, no. 5, May 2008, doi: 10.1542/peds.2007-0423.

[30] B. M. Van Den Hout, L. S. De Vries, L. C. Meiners, P. Stiers, Y. T. Van Der Schouw, A. Jennekens-Schinkel, D. Wittebol-Post, D. Van Der Linde, E. Vandenbussche, and O. Van Nieuwenhuizen, “Visual perceptual impairment in children at 5 years of age with perinatal haemorrhagic or ischaemic brain damage in

relation to cerebral magnetic resonance imaging," *Brain Dev.*, vol. 26, no. 4, pp. 251–261, Jun. 2004, doi: 10.1016/S0387-7604(03)00163-3.

[31] J. C. Harteman, P. G. J. Nikkels, M. J. N. L. Benders, A. Kwee, F. Groenendaal, and L. S. De Vries, "Placental pathology in full-term infants with hypoxic-ischemic neonatal encephalopathy and association with magnetic resonance imaging pattern of brain injury," *J. Pediatr.*, vol. 163, no. 4, 2013, doi: 10.1016/j.jpeds.2013.06.010.

[32] H. B. Sarnat and M. S. Sarnat, "Neonatal Encephalopathy Following Fetal Distress: A Clinical and Electroencephalographic Study," *Arch. Neurol.*, vol. 33, no. 10, pp. 696–705, Oct. 1976, doi: 10.1001/ARCHNEUR.1976.00500100030012.

[33] C. Acun, S. Karnati, S. Padiyar, S. Puthuraya, H. Aly, and M. Mohamed, "Trends of neonatal hypoxic-ischemic encephalopathy prevalence and associated risk factors in the United States, 2010 to 2018," in *American Journal of Obstetrics and Gynecology*, Elsevier Inc., Nov. 2022, pp. 751.e1-751.e10. doi: 10.1016/j.ajog.2022.06.002.

[34] B. Lemyre and V. Chau, "Hypothermia for newborns with hypoxic-ischemic encephalopathy," *Paediatr. Child Health*, vol. 23, no. 4, p. 285, Jul. 2018, doi: 10.1093/PCH/PXY028.

[35] S. Mehta, A. Joshi, B. Bajuk, N. Badawi, S. McIntyre, and K. Lui, "Eligibility criteria for therapeutic hypothermia: From trials to clinical practice," *J. Paediatr. Child Health*, vol. 53, no. 3, pp. 295–300, Mar. 2017, doi: 10.1111/jpc.13378.

[36] T. E. Inder, L. S. de Vries, D. M. Ferriero, P. E. Grant, L. R. Ment, S. P. Miller, and J. J. Volpe, "Neuroimaging of the Preterm Brain: Review and Recommendations," *J. Pediatr.*, vol. 237, no. 0, pp. 276-287.e4, 2021, doi: 10.1016/j.jpeds.2021.06.014.

[37] M. Guillot, V. Chau, and B. Lemyre, "Routine imaging of the preterm neonatal brain," *Paediatr. Child Heal.*, vol. 25, no. 4, pp. 249–255, Jun. 2020, doi: 10.1093/pch/pxaa033.

[38] J. Ibrahim, I. Mir, and L. Chalak, "Brain imaging in preterm infants <32 weeks gestation: a clinical review and algorithm for the use of cranial ultrasound and qualitative brain MRI," *Pediatric Research*, vol. 84, no. 6. Nature Publishing Group, pp. 799–806, Dec. 01, 2018. doi: 10.1038/s41390-018-0194-6.

[39] G. van Wezel-Meijler, S. J. Steggerda, and L. M. Leijser, "Cranial Ultrasonography in Neonates: Role and Limitations," *Seminars in Perinatology*, vol. 34, no. 1. pp. 28–38, Feb. 2010. doi: 10.1053/j.semperi.2009.10.002.

[40] J. L. Wisnowski, P. Wintermark, S. L. Bonifacio, C. D. Smyser, A. J. Barkovich, A. D. Edwards, L. S. de Vries, T. E. Inder, and V. Chau, "Neuroimaging in the term newborn with neonatal encephalopathy," *Semin. Fetal Neonatal Med.*, vol. 26, no. 5, Oct. 2021, doi: 10.1016/j.siny.2021.101304.

[41] J. Intrapiromkul, F. Northington, T. A. G. M. Huisman, I. Izbudak, A. Meoded, and A. Tekes, "Accuracy of head ultrasound for the detection of intracranial hemorrhage in preterm neonates: Comparison with brain MRI and susceptibility-weighted imaging," *J. Neuroradiol.*, vol. 40, no. 2, pp. 81–88, May 2013, doi: 10.1016/j.neurad.2012.03.006.

[42] S. J. Steggerda, L. M. Leijser, F. T. Wiggers-de Bruïne, J. Van Der Grond, F. J. Walther, and G. Van Wezel-Meijler, "Cerebellar injury in preterm infants: Incidence and findings on US and MR images," *Radiology*, vol. 252, no. 1, pp. 190–199, Jul. 2009, doi: 10.1148/radiol.2521081525.

[43] T. E. Inder, S. J. Wells, N. B. Mogridge, C. Spencer, and J. J. Volpe, "Defining the nature of the cerebral abnormalities in the premature infant: A qualitative magnetic resonance imaging study," *J. Pediatr.*, vol. 143, no. 2, pp. 171–179, Aug. 2003, doi: 10.1067/S0022-3476(03)00357-3.

[44] J. H. Miller, D. M. E. Bardo, and P. Cornejo, "Neonatal neuroimaging," *Semin. Pediatr. Neurol.*, vol. 33, Apr. 2020, doi: 10.1016/j.spen.2020.100796.

[45] M. Hinojosa-Rodríguez, T. Harmony, C. Carrillo-Prado, J. D. Van Horn, A. Irimia, C. Torgerson, and Z. Jacokes, "Clinical neuroimaging in the preterm infant: Diagnosis and prognosis," *NeuroImage: Clinical*, vol. 16. Elsevier Inc., pp. 355–368, 2017. doi: 10.1016/j.nicl.2017.08.015.

[46] O. Ciccarelli, M. Catani, H. Johansen-Berg, C. Clark, and A. Thompson, "Diffusion-based tractography in neurological disorders: concepts, applications, and future developments," *The Lancet Neurology*, vol. 7, no. 8. pp. 715–727, 2008. doi: 10.1016/S1474-4422(08)70163-7.

[47] P. L. Hope, E. B. Cady, P. S. Tofts, P. A. Hamilton, A. M. D. L. Costello, D. T. Delpy, A. Chu, E. O. R. Reynolds, and D. R. Wilkie, "Cerebral energy metabolism studied with phosphorus NMR spectroscopy in normal and birth-asphyxiated infants," *Lancet*, vol. 324, no. 8399, pp. 366–370, 1984, doi: 10.1016/S0140-6736(84)90539-7.

[48] C. E. Rogers, R. E. Lean, M. D. Wheelock, and C. D. Smyser, "Aberrant structural and functional connectivity and neurodevelopmental impairment in preterm children," *Journal of Neurodevelopmental Disorders*, vol. 10, no. 1. BioMed Central Ltd, Dec. 13, 2018. doi: 10.1186/s11689-018-9253-x.

[49] E. G. Duerden, S. Halani, K. Ng, T. Guo, J. Foong, T. J. A. Glass, V. Chau, H. M. Branson, J. G. Sled, H. E. Whyte, E. N. Kelly, and S. P. Miller, "White matter injury predicts disrupted functional connectivity and microstructure in very preterm born neonates," *NeuroImage Clin.*, vol. 21, p. 101596, Jan. 2019, doi: 10.1016/j.nicl.2018.11.006.

[50] C. D. Smyser, M. D. Wheelock, D. D. Limbrick, and J. J. Neil, "Neonatal brain injury and aberrant connectivity," *Neuroimage*, vol. 185, pp. 609–623, Jan. 2019, doi: 10.1016/J.NEUROIMAGE.2018.07.057.

[51] V. Y. Toronov, X. Zhang, and A. G. Webb, "A spatial and temporal comparison of hemodynamic signals measured using optical and functional magnetic resonance imaging during activation in the human primary visual cortex," *Neuroimage*, vol. 34, no. 3, p. 1136, Feb. 2007, doi: 10.1016/J.NEUROIMAGE.2006.08.048.

[52] M. F. . Ali, "Transcranial Doppler ultrasonography (uses, limitations, and potentials): a review article," *Egypt. J. Neurosurg.*, vol. 36, no. 1, Dec. 2021, doi: 10.1186/s41984-021-00114-0.

[53] F. F. Jöbsis, “Noninvasive, infrared monitoring of cerebral and myocardial oxygen sufficiency and circulatory parameters,” *Science (80-.).*, vol. 198, no. 4323, pp. 1264–1266, Dec. 1977, doi: 10.1126/science.929199.

[54] D. T. Delpy and M. Cope, “Quantification in tissue near-infrared spectroscopy,” *Philos. Trans. R. Soc. B Biol. Sci.*, vol. 352, no. 1354, pp. 649–659, 1997, doi: 10.1098/rstb.1997.0046.

[55] D. T. Delpy, M. Cope, P. Van Der Zee, S. Arridge, S. Wray, and J. Wyatt, “Estimation of optical pathlength through tissue from direct time of flight measurement,” *Phys. Med. Biol.*, vol. 33, no. 12, pp. 1433–1442, 1988, doi: 10.1088/0031-9155/33/12/008.

[56] F. Lange and I. Tachtsidis, “Clinical brain monitoring with time domain NIRS: A review and future perspectives,” *Applied Sciences (Switzerland)*, vol. 9, no. 8. MDPI AG, Apr. 01, 2019. doi: 10.3390/app9081612.

[57] H. Obrig and A. Villringer, “Beyond the visible - Imaging the human brain with light,” *Journal of Cerebral Blood Flow and Metabolism*, vol. 23, no. 1. Lippincott Williams and Wilkins, pp. 1–18, Jan. 01, 2003. doi: 10.1097/01.WCB.0000043472.45775.29.

[58] L. Kocsis, P. Herman, and A. Eke, “The modified Beer-Lambert law revisited,” *Phys. Med. Biol.*, vol. 51, no. 5, pp. N91–N98, 2006, doi: 10.1088/0031-9155/51/5/N02.

[59] S. Feng, F.-A. Zeng, and B. Chance, “Photon migration in the presence of a single defect: a perturbation analysis,” *Appl. Opt.*, vol. 34, no. 19, p. 3826, Jul. 1995, doi: 10.1364/AO.34.003826.

[60] A. Sassaroli, B. de B. Frederick, Y. Tong, P. F. Renshaw, and S. Fantini, “Spatially weighted BOLD signal for comparison of functional magnetic resonance imaging and near-infrared imaging of the brain,” *Neuroimage*, vol. 33, no. 2, pp. 505–514, Nov. 2006, doi: 10.1016/j.neuroimage.2006.07.006.

[61] J. Gemignani and J. Gervain, “Comparing different pre-processing routines for infant fNIRS data,” *Dev. Cogn. Neurosci.*, vol. 48, p. 100943, Apr. 2021, doi: 10.1016/J.DCN.2021.100943.

[62] L. M. Hocke, I. K. Oni, C. C. Duszynski, A. V. Corrigan, B. de B. Frederick, and J. F. Dunn, “Automated processing of fNIRS data-A visual guide to the pitfalls and consequences,” *Algorithms*, vol. 11, no. 5. 2018. doi: 10.3390/a11050067.

[63] L. Pollonini, H. Bortfeld, and J. S. Oghalai, “PHOEBE: a method for real time mapping of optodes-scalp coupling in functional near-infrared spectroscopy,” *Biomed. Opt. Express*, vol. 7, no. 12, p. 5104, 2016, doi: 10.1364/boe.7.005104.

[64] P. Pinti, I. Tachtsidis, A. Hamilton, J. Hirsch, C. Aichelburg, S. Gilbert, and P. W. Burgess, “The present and future use of functional near-infrared spectroscopy (Fnirs) for cognitive neuroscience,” *Ann. N. Y. Acad. Sci.*, vol. 1464, no. 1, pp. 5–29, 2020, doi: 10.1111/nyas.13948.

[65] F. Scholkmann, S. Spichtig, T. Muehlemann, and M. Wolf, “How to detect and

reduce movement artifacts in near-infrared imaging using moving standard deviation and spline interpolation," *Physiol. Meas.*, vol. 31, no. 5, pp. 649–662, 2010, doi: 10.1088/0967-3334/31/5/004.

[66] S. Jahani, S. K. Setarehdan, D. A. Boas, and M. A. Yücel, "Motion artifact detection and correction in functional near-infrared spectroscopy: a new hybrid method based on spline interpolation method and Savitzky-Golay filtering," *Neurophotonics*, vol. 5, no. 1, p. 1, Feb. 2018, doi: 10.1117/1.NPH.5.1.015003.

[67] A. M. Chiarelli, E. L. Maclin, M. Fabiani, and G. Gratton, "A kurtosis-based wavelet algorithm for motion artifact correction of fNIRS data," *Neuroimage*, vol. 112, pp. 128–137, May 2015, doi: 10.1016/j.neuroimage.2015.02.057.

[68] B. Molavi and G. A. Dumont, "Wavelet-based motion artifact removal for functional near-infrared spectroscopy," *Physiol. Meas.*, vol. 33, no. 2, pp. 259–270, 2012, doi: 10.1088/0967-3334/33/2/259.

[69] R. Di Lorenzo, L. Pirazzoli, A. Blasi, C. Bulgarelli, Y. Hakuno, Y. Minagawa, and S. Brigadoi, "Recommendations for motion correction of infant fNIRS data applicable to multiple data sets and acquisition systems," *Neuroimage*, vol. 200, pp. 511–527, Oct. 2019, doi: 10.1016/J.NEUROIMAGE.2019.06.056.

[70] M. Izzetoglu, P. Chitrapu, S. Bunce, and B. Onaral, "Motion artifact cancellation in NIR spectroscopy using discrete Kalman filtering," *Biomed. Eng. Online*, vol. 9, no. 1, pp. 1–10, Mar. 2010, doi: 10.1186/1475-925X-9-16.

[71] H. Santosa, M. Jiyoun Hong, S. P. Kim, and K. S. Hong, "Noise reduction in functional near-infrared spectroscopy signals by independent component analysis," *Rev. Sci. Instrum.*, vol. 84, no. 7, Jul. 2013, doi: 10.1063/1.4812785.

[72] P. Pinti, F. Scholkmann, A. Hamilton, P. Burgess, and I. Tachtsidis, "Current Status and Issues Regarding Pre-processing of fNIRS Neuroimaging Data: An Investigation of Diverse Signal Filtering Methods Within a General Linear Model Framework," *Front. Hum. Neurosci.*, vol. 12, p. 505, Jan. 2019, doi: 10.3389/FNHUM.2018.00505/BIBTEX.

[73] I. Tachtsidis and F. Scholkmann, "False positives and false negatives in functional near-infrared spectroscopy: issues, challenges, and the way forward," *Neurophotonics*, vol. 3, no. 3, p. 031405, 2016, doi: 10.1117/1.nph.3.3.031405.

[74] B. Biswal, F. Zerrin Yetkin, V. M. Haughton, and J. S. Hyde, "Functional connectivity in the motor cortex of resting human brain using echo-planar mri," *Magn. Reson. Med.*, vol. 34, no. 4, pp. 537–541, Oct. 1995, doi: 10.1002/mrm.1910340409.

[75] S. Brigadoi and R. J. Cooper, "How short is short? Optimum source–detector distance for short-separation channels in functional near-infrared spectroscopy," *Neurophotonics*, vol. 2, no. 2, p. 025005, May 2015, doi: 10.1117/1.nph.2.2.025005.

[76] M. D. Pfeifer, F. Scholkmann, and R. Labruyère, "Signal processing in functional near-infrared spectroscopy (fNIRS): Methodological differences lead to different statistical results," *Front. Hum. Neurosci.*, vol. 11, no. January, pp. 1–12, 2018, doi: 10.3389/fnhum.2017.00641.

[77] D. Wyser, M. Mattille, M. Wolf, O. Lambercy, F. Scholkmann, and R. Gassert, “Short-channel regression in functional near-infrared spectroscopy is more effective when considering heterogeneous scalp hemodynamics,” *Neurophotonics*, vol. 7, no. 03, Sep. 2020, doi: 10.1117/1.nph.7.3.035011.

[78] B. Blanco, M. Molnar, C. Caballero-Gaudes, and C. Caballero, “Effect of prewhitening in resting-state functional near-infrared spectroscopy data,” vol. 5, no. 4, p. 40401, 2018, doi: 10.1117/1.NPh.5.4.040401.

[79] A. A. Phillips, F. H. Chan, M. M. Z. Zheng, A. V. Krassioukov, and P. N. Ainslie, “Neurovascular coupling in humans: Physiology, methodological advances and clinical implications,” *J. Cereb. Blood Flow Metab.*, vol. 36, no. 4, pp. 647–664, 2015, doi: 10.1177/0271678X15617954.

[80] J. H. Meek, M. Firbank, C. E. Elwell, J. Atkinson, O. Braddick, and J. S. Wyatt, “Regional Hemodynamic Responses to Visual Stimulation in Awake Infants,” *Pediatr. Res. 1998 436*, vol. 43, no. 6, pp. 840–843, 1998, doi: 10.1203/00006450-199806000-00019.

[81] D. B. Plewes and W. Kucharczyk, “Physics of MRI: A primer,” *Journal of Magnetic Resonance Imaging*, vol. 35, no. 5. pp. 1038–1054, May 2012. doi: 10.1002/jmri.23642.

[82] E. L. Hahn, “Spin Echoes,” *Phys. Rev.*, vol. 80, no. 4, p. 580, Nov. 1950, doi: 10.1103/PhysRev.80.580.

[83] E. G. Duerden, M. J. Taylor, and S. P. Miller, “Brain development in infants born preterm: Looking beyond injury,” *Semin. Pediatr. Neurol.*, vol. 20, no. 2, pp. 65–74, 2013, doi: 10.1016/j.spen.2013.06.007.

[84] M. A. Rutherford, V. Supramaniam, A. Ederies, A. Chew, L. Bassi, M. Groppo, M. Anjari, S. Counsell, and L. A. Ramenghi, “Magnetic resonance imaging of white matter diseases of prematurity,” *Neuroradiology*, vol. 52, no. 6. Springer Verlag, pp. 505–521, 2010. doi: 10.1007/s00234-010-0700-y.

[85] E. Van Reeth, I. W. K. Tham, C. Heng Tan, and C. Loo Poh, “Super-Resolution in Magnetic Resonance Imaging: A Review,” 2012, doi: 10.1002/cmra.21249.

[86] G. H. Glover, “Overview of functional magnetic resonance imaging,” *Neurosurgery Clinics of North America*, vol. 22, no. 2. pp. 133–139, Apr. 2011. doi: 10.1016/j.nec.2010.11.001.

[87] H. Jahanian, S. Holdsworth, T. Christen, H. Wu, K. Zhu, A. B. Kerr, M. J. Middione, R. F. Dougherty, M. Moseley, and G. Zaharchuk, “Advantages of short repetition time resting-state functional MRI enabled by simultaneous multi-slice imaging,” *J. Neurosci. Methods*, vol. 311, pp. 122–132, Jan. 2019, doi: 10.1016/j.jneumeth.2018.09.033.

[88] M. Jenkinson, C. F. Beckmann, T. E. J. Behrens, M. W. Woolrich, and S. M. Smith, “FSL,” *Neuroimage*, vol. 62, no. 2, pp. 782–790, Aug. 2012, doi: 10.1016/J.NEUROIMAGE.2011.09.015.

[89] R. W. Cox, “AFNI: Software for analysis and visualization of functional magnetic

resonance neuroimages," *Comput. Biomed. Res.*, vol. 29, no. 3, pp. 162–173, 1996, doi: 10.1006/cbmr.1996.0014.

[90] L. A. Grajauskas, T. Frizzell, X. Song, and R. C. N. D'Arcy, "White Matter fMRI Activation Cannot Be Treated as a Nuisance Regressor: Overcoming a Historical Blind Spot," *Front. Neurosci.*, vol. 13, Oct. 2019, doi: 10.3389/fnins.2019.01024.

[91] M. P. van den Heuvel and H. E. Hulshoff Pol, "Exploring the brain network: A review on resting-state fMRI functional connectivity," *Eur. Neuropsychopharmacol.*, vol. 20, no. 8, pp. 519–534, 2010, doi: 10.1016/j.euroneuro.2010.03.008.

[92] K. A. Smitha, K. Akhil Raja, K. M. Arun, P. G. Rajesh, B. Thomas, T. R. Kapilamoorthy, and C. Kesavadas, "Resting state fMRI: A review on methods in resting state connectivity analysis and resting state networks," *Neuroradiology Journal*, vol. 30, no. 4. SAGE Publications Inc., pp. 305–317, Aug. 01, 2017. doi: 10.1177/1971400917697342.

[93] S. M. Smith, D. Vidaurre, C. F. Beckmann, M. F. Glasser, M. Jenkinson, K. L. Miller, T. E. Nichols, E. C. Robinson, G. Salimi-Khorshidi, M. W. Woolrich, D. M. Barch, K. Uğurbil, and D. C. Van Essen, "Functional connectomics from resting-state fMRI," *Trends in Cognitive Sciences*, vol. 17, no. 12. pp. 666–682, Dec. 2013. doi: 10.1016/j.tics.2013.09.016.

[94] B. A. Seitzman, A. Z. Snyder, E. C. Leuthardt, and J. S. Shimony, "The State of Resting State Networks," *Topics in Magnetic Resonance Imaging*, vol. 28, no. 4. Lippincott Williams and Wilkins, pp. 189–196, Aug. 01, 2019. doi: 10.1097/RMR.0000000000000214.

[95] C. Rosazza and L. Minati, "Resting-state brain networks: Literature review and clinical applications," *Neurol. Sci.*, vol. 32, no. 5, pp. 773–785, Oct. 2011, doi: 10.1007/s10072-011-0636-y.

[96] M. D. Greicius, B. Krasnow, A. L. Reiss, V. Menon, and M. E. Raichle, "Functional connectivity in the resting brain: A network analysis of the default mode hypothesis." [Online]. Available: www.pnas.org.

[97] J. R. Andrews-Hanna, "The brain's default network and its adaptive role in internal mentation," *Neuroscientist*, vol. 18, no. 3. pp. 251–270, Jun. 2012. doi: 10.1177/1073858411403316.

[98] J. D. Power, A. L. Cohen, S. M. Nelson, G. S. Wig, K. A. Barnes, J. A. Church, A. C. Vogel, T. O. Laumann, F. M. Miezin, B. L. Schlaggar, and S. E. Petersen, "Functional Network Organization of the Human Brain," *Neuron*, vol. 72, no. 4, pp. 665–678, Nov. 2011, doi: 10.1016/J.NEURON.2011.09.006.

[99] M. E. Raichle and M. A. Mintun, "Brain work and brain imaging," *Annu. Rev. Neurosci.*, vol. 29, no. Volume 29, 2006, pp. 449–476, Jul. 2006, doi: 10.1146/ANNUREV.NEURO.29.051605.112819/CITE/REFWORKS.

[100] A. H. Andersen, D. M. Gash, and M. J. Avison, "Principal component analysis of the dynamic response measured by fMRI: A generalized linear systems framework," *Magn. Reson. Imaging*, vol. 17, no. 6, pp. 795–815, 1999, doi: 10.1016/S0730-

725X(99)00028-4.

[101] M. J. McKeown, L. K. Hansen, and T. J. Sejnowsk, “Independent component analysis of functional MRI: What is signal and what is noise?,” *Current Opinion in Neurobiology*, vol. 13, no. 5. Howard Hughes Medical Institute, pp. 620–629, 2003. doi: 10.1016/j.conb.2003.09.012.

[102] Y. Wang, J. Kang, P. B. Kemmer, and Y. Guo, “An efficient and reliable statistical method for estimating functional connectivity in large scale brain networks using partial correlation,” *Front. Neurosci.*, vol. 10, p. 123, Mar. 2016, doi: 10.3389/fnins.2016.00123.

[103] J. Peng, P. Wang, N. Zhou, and J. Zhu, “Partial correlation estimation by joint sparse regression models,” *J. Am. Stat. Assoc.*, vol. 104, no. 486, pp. 735–746, Jun. 2009, doi: 10.1198/jasa.2009.0126.

[104] S. L. Bressler and A. K. Seth, “Wiener-Granger Causality: A well established methodology,” *NeuroImage*, vol. 58, no. 2. pp. 323–329, Sep. 15, 2011. doi: 10.1016/j.neuroimage.2010.02.059.

[105] K. J. Friston, L. Harrison, and W. Penny, “Dynamic causal modelling,” *Neuroimage*, vol. 19, no. 4, pp. 1273–1302, Aug. 2003, doi: 10.1016/S1053-8119(03)00202-7.

[106] S. Sasai, F. Homae, H. Watanabe, A. T. Sasaki, H. C. Tanabe, N. Sadato, and G. Taga, “A NIRS-fMRI study of resting state network,” *Neuroimage*, vol. 63, no. 1, pp. 179–193, Oct. 2012, doi: 10.1016/j.neuroimage.2012.06.011.

[107] L. Duan, Y. J. Zhang, and C. Z. Zhu, “Quantitative comparison of resting-state functional connectivity derived from fNIRS and fMRI: A simultaneous recording study,” *Neuroimage*, vol. 60, no. 4, pp. 2008–2018, May 2012, doi: 10.1016/j.neuroimage.2012.02.014.

[108] C. Bulgarelli, A. Blasi, S. Arridge, S. Powell, C. C. J. M. de Klerk, V. Southgate, S. Brigadoi, W. Penny, S. Tak, and A. Hamilton, “Dynamic causal modelling on infant fNIRS data: A validation study on a simultaneously recorded fNIRS-fMRI dataset,” *Neuroimage*, vol. 175, pp. 413–424, Jul. 2018, doi: 10.1016/j.neuroimage.2018.04.022.

[109] M. G. Kozberg, Y. Ma, M. A. Shaik, S. H. Kim, and E. M. C. Hillman, “Rapid postnatal expansion of neural networks occurs in an environment of altered neurovascular and neurometabolic coupling,” *J. Neurosci.*, vol. 36, no. 25, pp. 6704–6717, Jun. 2016, doi: 10.1523/JNEUROSCI.2363-15.2016.

[110] G. Chen, G. Chen, C. Xie, and S. J. Li, “Negative Functional Connectivity and Its Dependence on the Shortest Path Length of Positive Network in the Resting-State Human Brain,” *Brain Connect.*, vol. 1, no. 3, pp. 195–206, Sep. 2011, doi: 10.1089/brain.2011.0025.

[111] J. D. Power, D. A. Fair, B. L. Schlaggar, and S. E. Petersen, “The Development of Human Functional Brain Networks,” *Neuron*, vol. 67, no. 5. pp. 735–748, Sep. 2010. doi: 10.1016/j.neuron.2010.08.017.

[112] M. Rubinov and O. Sporns, “Complex network measures of brain connectivity: Uses

and interpretations," *Neuroimage*, vol. 52, no. 3, pp. 1059–1069, Sep. 2010, doi: 10.1016/j.neuroimage.2009.10.003.

[113] E. W. Dijkstra, "A note on two problems in connexion with graphs," *Numer. Math.*, vol. 1, no. 1, pp. 269–271, Dec. 1959, doi: 10.1007/BF01386390/METRICS.

[114] D. S. Bassett and E. Bullmore, "Small-world brain networks," *Neuroscientist*, vol. 12, no. 6, pp. 512–523, Dec. 2006, doi: 10.1177/1073858406293182.

[115] M. P. van den Heuvel and O. Sporns, "Network hubs in the human brain," *Trends Cogn. Sci.*, vol. 17, no. 12, pp. 683–696, Dec. 2013, doi: 10.1016/j.tics.2013.09.012.

[116] N. Masuda, M. Sakaki, T. Ezaki, and T. Watanabe, "Clustering coefficients for correlation networks," *Front. Neuroinform.*, vol. 12, Mar. 2018, doi: 10.3389/fninf.2018.00007.

[117] V. D. Blondel, J. L. Guillaume, R. Lambiotte, and E. Lefebvre, "Fast unfolding of communities in large networks," *J. Stat. Mech. Theory Exp.*, vol. 2008, no. 10, Oct. 2008, doi: 10.1088/1742-5468/2008/10/P10008.

[118] L. Tang, S. Mostafa, B. Liao, and F. X. Wu, "A network clustering based feature selection strategy for classifying autism spectrum disorder," *BMC Med. Genomics*, vol. 12, Dec. 2019, doi: 10.1186/s12920-019-0598-0.

[119] P. Erdös and A. Rényi, "On random graphs I," *Publ. Math.*, vol. 6, pp. 290–297, 1959.

[120] V. Latora and M. Marchiori, "Efficient behavior of small-world networks," *Phys. Rev. Lett.*, vol. 87, no. 19, pp. 198701-1-198701–4, Nov. 2001, doi: 10.1103/PhysRevLett.87.198701.

[121] V. Doria, C. F. Beckmann, T. Arichi, N. Merchant, M. Groppo, F. E. Turkheimer, S. J. Counsell, M. Murgasova, P. Aljabar, R. G. Nunes, D. J. Larkman, G. Rees, and A. D. Edwards, "Emergence of resting state networks in the preterm human brain," *Proc. Natl. Acad. Sci. U. S. A.*, vol. 107, no. 46, pp. 20015–20020, Nov. 2010, doi: 10.1073/pnas.1007921107.

[122] C. D. Smyser, T. E. Inder, J. S. Shimony, J. E. Hill, A. J. Degnan, A. Z. Snyder, and J. J. Neil, "Longitudinal Analysis of Neural Network Development in Preterm Infants," *Cereb. Cortex*, vol. 20, no. 12, pp. 2852–2862, Dec. 2010, doi: 10.1093/CERCOR/BHQ035.

[123] C. D. Smyser, A. Z. Snyder, J. S. Shimony, A. Mitra, T. E. Inder, and J. J. Neil, "Resting-State Network Complexity and Magnitude Are Reduced in Prematurely Born Infants," *Cereb. Cortex*, vol. 26, no. 1, pp. 322–333, Jan. 2016, doi: 10.1093/cercor/bhu251.

[124] G. Ball, P. Aljabar, T. Arichi, N. Tusor, D. Cox, N. Merchant, P. Nongena, J. V. Hajnal, A. D. Edwards, and S. J. Counsell, "Machine-learning to characterise neonatal functional connectivity in the preterm brain," *Neuroimage*, vol. 124, pp. 267–275, Jan. 2016, doi: 10.1016/j.neuroimage.2015.08.055.

[125] B. R. White, S. M. Liao, S. L. Ferradal, T. E. Inder, and J. P. Culver, "Bedside optical imaging of occipital resting-state functional connectivity in neonates,"

Neuroimage, vol. 59, no. 3, pp. 2529–2538, Feb. 2012, doi: 10.1016/j.neuroimage.2011.08.094.

[126] Y. Fuchino, N. Naoi, M. Shibata, F. Niwa, M. Kawai, Y. Konishi, K. Okanoya, and M. Myowa-Yamakoshi, "Effects of Preterm Birth on Intrinsic Fluctuations in Neonatal Cerebral Activity Examined Using Optical Imaging," *PLoS One*, vol. 8, no. 6, p. e67432, Jun. 2013, doi: 10.1371/JOURNAL.PONE.0067432.

[127] M. Cao, Y. He, Z. Dai, X. Liao, T. Jeon, M. Ouyang, L. Chalak, Y. Bi, N. Rollins, Q. Dong, and H. Huang, "Early development of functional network segregation revealed by connectomic analysis of the preterm human brain," *Cereb. Cortex*, vol. 27, no. 3, pp. 1949–1963, Mar. 2017, doi: 10.1093/cercor/bhw038.

[128] C. D. Smyser, A. Z. Snyder, J. S. Shimony, T. M. Blazey, T. E. Inder, and J. J. Neil, "Effects of White Matter Injury on Resting State fMRI Measures in Prematurely Born Infants," *PLoS One*, vol. 8, no. 7, p. e68098, Jul. 2013, doi: 10.1371/journal.pone.0068098.

[129] D. Lee, C. Pae, J. D. Lee, E. S. Park, S. R. Cho, M. H. Um, S. K. Lee, M. K. Oh, and H. J. Park, "Analysis of structure–function network decoupling in the brain systems of spastic diplegic cerebral palsy," *Hum. Brain Mapp.*, vol. 38, no. 10, pp. 5292–5306, Oct. 2017, doi: 10.1002/hbm.23738.

[130] N. Tusor, "Diffusion tensor imaging and resting state functional connectivity as advanced imaging biomarkers of outcome in infants with hypoxic-ischaemic encephalopathy treated with hypothermia," Imperial College London.

[131] L. Jiang, D. El-Metwally, C. Sours Rhodes, J. Zhuo, R. Almardawi, A. E. Medina, L. Wang, R. P. Gullapalli, and P. Raghavan, "Alterations in motor functional connectivity in Neonatal Hypoxic Ischemic Encephalopathy," *Brain Inj.*, vol. 36, no. 2, pp. 287–294, Jan. 2022, doi: 10.1080/02699052.2022.2034041.

[132] S. Zhang, C. Peng, Y. Yang, D. Wang, X. Hou, and D. Li, "Resting-state brain networks in neonatal hypoxic-ischemic brain damage: a functional near-infrared spectroscopy study," *Neurophotonics*, vol. 8, no. 2, p. 025007, May 2021, doi: 10.1117/1.NPH.8.2.025007.

[133] M. Cao, H. Huang, and Y. He, "Developmental Connectomics from Infancy through Early Childhood," *Trends in Neurosciences*, vol. 40, no. 8. Elsevier Ltd, pp. 494–506, Aug. 01, 2017. doi: 10.1016/j.tins.2017.06.003.

[134] Y. Zhang and C. Zhu, "Assessing Brain Networks by Resting-State Dynamic Functional Connectivity: An fNIRS-EEG Study," *Front. Neurosci.*, vol. 13, p. 497285, Jan. 2020, doi: 10.3389/FNINS.2019.01430/BIBTEX.

[135] L. Jiang, D. El-Metwally, C. Sours Rhodes, J. Zhuo, R. Almardawi, A. E. Medina, L. Wang, R. P. Gullapalli, and P. Raghavan, "Alterations in motor functional connectivity in Neonatal Hypoxic Ischemic Encephalopathy," *Brain Inj.*, vol. 36, no. 2, pp. 287–294, 2022, doi: 10.1080/02699052.2022.2034041.

[136] J. R. Koza, F. H. Bennett, D. Andre, and M. A. Keane, "Automated Design of Both the Topology and Sizing of Analog Electrical Circuits Using Genetic Programming," in *Artificial Intelligence in Design '96*, Springer, Dordrecht, 1996,

pp. 151–170. doi: 10.1007/978-94-009-0279-4_9.

[137] L. Adlung, Y. Cohen, U. Mor, and E. Elinav, “Machine learning in clinical decision making,” *Med*, vol. 2, no. 6. Cell Press, pp. 642–665, Jun. 11, 2021. doi: 10.1016/j.medj.2021.04.006.

[138] S. Sharma, S. Sharma, and A. Athaiya, “Activation functions in neural networks,” *Int. J. Eng. Appl. Sci. Technol.*, vol. 04, no. 12, pp. 310–316, 2020, doi: 10.33564/ijeast.2020.v04i12.054.

[139] M. Kuhn and K. Johnson, *Applied predictive modeling*. 2013. doi: 10.1007/978-1-4614-6849-3.

[140] Y. Xu and R. Goodacre, “On Splitting Training and Validation Set: A Comparative Study of Cross-Validation, Bootstrap and Systematic Sampling for Estimating the Generalization Performance of Supervised Learning,” *J. Anal. Test.*, vol. 2, no. 3, pp. 249–262, Jul. 2018, doi: 10.1007/s41664-018-0068-2.

[141] C. Davatzikos, “Machine learning in neuroimaging: Progress and challenges,” *NeuroImage*, vol. 197. Academic Press Inc., pp. 652–656, Aug. 15, 2019. doi: 10.1016/j.neuroimage.2018.10.003.

[142] J. M. Mateos-Pérez, M. Dadar, M. Lacalle-Aurioles, Y. Iturria-Medina, Y. Zeighami, and A. C. Evans, “Structural neuroimaging as clinical predictor: A review of machine learning applications,” *NeuroImage: Clinical*, vol. 20. Elsevier Inc., pp. 506–522, Jan. 01, 2018. doi: 10.1016/j.nicl.2018.08.019.

[143] S. Rathore, M. Habes, M. A. Iftikhar, A. Shacklett, and C. Davatzikos, “A review on neuroimaging-based classification studies and associated feature extraction methods for Alzheimer’s disease and its prodromal stages,” *NeuroImage*, vol. 155. Academic Press Inc., pp. 530–548, Jul. 15, 2017. doi: 10.1016/j.neuroimage.2017.03.057.

[144] K. H. Nenning and G. Langs, “Machine learning in neuroimaging: from research to clinical practice,” *Radiologie*, vol. 62. Springer Medizin, pp. 1–10, Dec. 01, 2022. doi: 10.1007/s00117-022-01051-1.

[145] J. D. Raad, R. B. Chinnam, S. Arslanturk, S. Tan, J. W. Jeong, and S. Mody, “Unsupervised abnormality detection in neonatal MRI brain scans using deep learning,” *Sci. Rep.*, vol. 13, no. 1, Dec. 2023, doi: 10.1038/s41598-023-38430-0.

[146] A. M. Pavel, J. M. O’Toole, J. Proietti, V. Livingstone, S. Mitra, W. P. Marnane, M. Finder, E. M. Dempsey, D. M. Murray, G. B. Boylan, E. Pavlidis, L. Kharoshankaya, S. R. Mathieson, G. Lightbody, J. O’Leary, M. Murray, J. Conway, D. Dwyer, A. Temko, T. Kiely, A. C. Ryan, J. M. Rennie, L. S. de Vries, L. C. Weeke, M. C. Toet, J. C. Harteman, M. Blennow, I. Edqvist, A. Foran, R. M. Pinnamaneni, J. Colby-Milley, D. K. Shah, N. Openshaw-Lawrence, R. M. Pressler, O. Kapellou, and A. C. van Huffelen, “Machine learning for the early prediction of infants with electrographic seizures in neonatal hypoxic-ischemic encephalopathy,” *Epilepsia*, vol. 64, no. 2, pp. 456–468, Feb. 2023, doi: 10.1111/epi.17468.

[147] C. D. Smyser, N. U. F. Dosenbach, T. A. Smyser, A. Z. Snyder, C. E. Rogers, T. E. Inder, B. L. Schlaggar, and J. J. Neil, “Prediction of brain maturity in infants using

machine-learning algorithms," *Neuroimage*, vol. 136, pp. 1–9, Aug. 2016, doi: 10.1016/j.neuroimage.2016.05.029.

[148] M. Ashoori, J. M. O'Toole, K. D. O'Halloran, G. Naulaers, L. Thewissen, J. Miletin, P. Y. Cheung, A. EL-Khuffash, D. Van Laere, Z. Straňák, E. M. Dempsey, and F. B. McDonald, "Machine Learning Detects Intraventricular Haemorrhage in Extremely Preterm Infants †," *Children*, vol. 10, no. 6, Jun. 2023, doi: 10.3390/children10060917.

[149] D. Bili, F. Lange, K. Harvey Jones, V. Parfentyeva, T. Durduran, N. Robertson, S. Mitra, and I. Tachtsidis, "Classification of brain injury severity using a hybrid broadband NIRS and DCS instrument with a machine learning approach," SPIE-Intl Soc Optical Eng, Aug. 2023, p. 12. doi: 10.1117/12.2670657.

[150] J. P. McAllister, M. M. Guerra, L. C. Ruiz, A. J. Jimenez, D. Dominguez-Pinos, D. Sival, W. den Dunnen, D. M. Morales, R. E. Schmidt, E. M. Rodriguez, and D. D. Limbrick, "Ventricular zone disruption in human neonates with intraventricular hemorrhage," *J. Neuropathol. Exp. Neurol.*, vol. 76, no. 5, pp. 358–375, May 2017, doi: 10.1093/jnen/nlx017.

[151] B. R. Vohr, "Neurodevelopmental outcomes of premature infants with intraventricular hemorrhage across a lifespan," *Semin. Perinatol.*, vol. 46, no. 5, p. 151594, Aug. 2022, doi: 10.1016/j.semperi.2022.151594.

[152] Q. Wang, G. P. Zhu, L. Yi, X. X. Cui, H. Wang, R. Y. Wei, and B. L. Hu, "A Review of Functional Near-Infrared Spectroscopy Studies of Motor and Cognitive Function in Preterm Infants," *Neurosci. Bull.*, vol. 36, no. 3, pp. 321–329, Mar. 2020, doi: 10.1007/S12264-019-00441-1/TABLES/1.

[153] R. L. Triplett and C. D. Smyser, "Neuroimaging of structural and functional connectivity in preterm infants with intraventricular hemorrhage," *Semin. Perinatol.*, vol. 46, no. 5, p. 151593, Aug. 2022, doi: 10.1016/j.semperi.2022.151593.

[154] A. C. Linke, C. Wild, L. Zubiaurre-Elorza, C. Herzmann, H. Duffy, V. K. Han, D. S. C. Lee, and R. Cusack, "Disruption to functional networks in neonates with perinatal brain injury predicts motor skills at 8 months," *Neuroimage (Amst).*, vol. 18, p. 399, 2018, doi: 10.1016/J.NICL.2018.02.002.

[155] V. Scarapicchia, C. Brown, C. Mayo, and J. R. Gawryluk, "Functional magnetic resonance imaging and functional near-infrared spectroscopy: Insights from combined recording studies," *Front. Hum. Neurosci.*, vol. 11, no. August, pp. 1–12, 2017, doi: 10.3389/fnhum.2017.00419.

[156] M. I. Argyropoulou, V. G. Xydis, A. Drougia, A. S. Giantsouli, V. Giapros, and L. G. Astrakas, "Structural and functional brain connectivity in moderate–late preterm infants with low-grade intraventricular hemorrhage," *Neuroradiology*, vol. 64, no. 1, pp. 197–204, Jan. 2022, doi: 10.1007/S00234-021-02770-3/FIGURES/2.

[157] J. H. Cha, Y. H. Choi, J. M. Lee, J. Y. Lee, H. K. Park, J. Kim, I. K. Kim, and H. J. Lee, "Altered structural brain networks at term-equivalent age in preterm infants with grade 1 intraventricular hemorrhage," *Ital. J. Pediatr.*, vol. 46, no. 1, p. 43, Apr.

2020, doi: 10.1186/s13052-020-0796-6.

[158] L. M. N. Kebaya, K. Stubbs, M. Lo, S. Al-Saoud, B. Karat, K. St Lawrence, S. de Ribaupierre, and E. G. Duerden, "Three-dimensional cranial ultrasound and functional near-infrared spectroscopy for bedside monitoring of intraventricular hemorrhage in preterm neonates," *Sci. Rep.*, vol. 13, no. 1, pp. 1–13, Mar. 2023, doi: 10.1038/s41598-023-30743-4.

[159] A. Makropoulos, E. C. Robinson, A. Schuh, R. Wright, S. Fitzgibbon, J. Bozek, S. J. Counsell, J. Steinweg, K. Vecchiato, J. Passerat-Palmbach, G. Lenz, F. Mortari, T. Tenev, E. P. Duff, M. Bastiani, L. Cordero-Grande, E. Hughes, N. Tusor, J.-D. Tournier, J. Hutter, A. N. Price, R. A. Pedro G Teixeira, M. Murgasova, S. Victor, C. Kelly, M. A. Rutherford, S. M. Smith, A. David Edwards, J. V Hajnal, M. Jenkinson, and D. Rueckert, "The Developing Human Connectome Project: a Minimal Processing Pipeline for Neonatal Cortical Surface Reconstruction Europe PMC Funders Group," *Neuroimage*, vol. 173, pp. 88–112, 2018, doi: 10.1101/125526.

[160] M. Tantardini, F. Ieva, L. Tajoli, and C. Piccardi, "Comparing methods for comparing networks," *Sci. Rep.*, vol. 9, no. 1, pp. 1–19, Nov. 2019, doi: 10.1038/s41598-019-53708-y.

[161] M. P. van den Heuvel, S. C. de Lange, A. Zalesky, C. Seguin, B. T. T. Yeo, and R. Schmidt, "Proportional thresholding in resting-state fMRI functional connectivity networks and consequences for patient-control connectome studies: Issues and recommendations," *Neuroimage*, vol. 152, pp. 437–449, May 2017, doi: 10.1016/j.neuroimage.2017.02.005.

[162] H. Ahmadi, E. Fatemizadeh, and A. M. Nasrabadi, "A comparative study of the effect of weighted or binary functional brain networks in fMRI data analysis," *Front. Biomed. Technol.*, vol. 7, no. 3, pp. 160–169, Sep. 2020, doi: 10.18502/fbt.v7i3.4618.

[163] K. A. Garrison, D. Scheinost, E. S. Finn, X. Shen, and R. T. Constable, "The (in)stability of functional brain network measures across thresholds," *Neuroimage*, vol. 118, pp. 651–661, Sep. 2015, doi: 10.1016/j.neuroimage.2015.05.046.

[164] A. Gallagher, F. Wallois, and H. Obrig, "Functional near-infrared spectroscopy in pediatric clinical research: Different pathophysiologies and promising clinical applications," *Neurophotonics*, vol. 10, no. 02, p. 023517, Mar. 2023, doi: 10.1117/1.nph.10.2.023517.

[165] R. B. Buxton, "The physics of functional magnetic resonance imaging (fMRI)," *Reports Prog. Phys.*, vol. 76, no. 9, Sep. 2013, doi: 10.1088/0034-4885/76/9/096601.

[166] V. Toronov, S. Walker, R. Gupta, J. H. Choi, E. Gratton, D. Hueber, and A. Webb, "The roles of changes in deoxyhemoglobin concentration and regional cerebral blood volume in the fMRI BOLD signal," *Neuroimage*, vol. 19, no. 4, pp. 1521–1531, Aug. 2003, doi: 10.1016/S1053-8119(03)00152-6.

[167] Y. Tong and B. de B. Frederick, "Concurrent fNIRS and fMRI processing allows

independent visualization of the propagation of pressure waves and bulk blood flow in the cerebral vasculature," *Neuroimage*, vol. 61, no. 4, pp. 1419–1427, Jul. 2012, doi: 10.1016/j.neuroimage.2012.03.009.

[168] G. Xu, C. Huo, J. Yin, Y. Zhong, G. Sun, Y. Fan, D. Wang, and Z. Li, "Test-retest reliability of fNIRS in resting-state cortical activity and brain network assessment in stroke patients," *Biomed. Opt. Express*, vol. 14, no. 8, p. 4217, Aug. 2023, doi: 10.1364/boe.491610.

[169] A. Abdalmalak, S. L. Novi, K. Kazazian, L. Norton, T. Benaglia, M. Slessarev, D. B. Debicki, K. S. Lawrence, R. C. Mesquita, and A. M. Owen, "Effects of Systemic Physiology on Mapping Resting-State Networks Using Functional Near-Infrared Spectroscopy," *Front. Neurosci.*, vol. 16, Mar. 2022, doi: 10.3389/fnins.2022.803297.

[170] S. Sasai, F. Homae, H. Watanabe, and G. Taga, "Frequency-specific functional connectivity in the brain during resting state revealed by NIRS," *Neuroimage*, vol. 56, no. 1, pp. 252–257, 2011, doi: 10.1016/j.neuroimage.2010.12.075.

[171] T. Nguyen, O. Babawale, T. Kim, H. J. Jo, H. Liu, and J. G. Kim, "Exploring brain functional connectivity in rest and sleep states: a fNIRS study," *Sci. Reports 2018 81*, vol. 8, no. 1, pp. 1–10, Nov. 2018, doi: 10.1038/s41598-018-33439-2.

[172] Z. Einalou, K. Maghooli, S. K. Setarehdan, and A. Akin, "Graph theoretical approach to functional connectivity in prefrontal cortex via fNIRS," *Neurophotonics*, vol. 4, no. 04, p. 041407, Aug. 2017, doi: 10.1117/1.nph.4.4.041407.

[173] M. Y. Wang, F. M. Lu, Z. Hu, J. Zhang, and Z. Yuan, "Optical mapping of prefrontal brain connectivity and activation during emotion anticipation," *Behav. Brain Res.*, vol. 350, pp. 122–128, Sep. 2018, doi: 10.1016/J.BBR.2018.04.051.

[174] Y. L. Chan, W. C. Ung, L. G. Lim, C. K. Lu, M. Kiguchi, and T. B. Tang, "Automated Thresholding Method for fNIRS-Based Functional Connectivity Analysis: Validation with a Case Study on Alzheimer's Disease," *IEEE Trans. Neural Syst. Rehabil. Eng.*, vol. 28, no. 8, pp. 1691–1701, Aug. 2020, doi: 10.1109/TNSRE.2020.3007589.

[175] S. I. Dimitriadis, C. Salis, I. Tarnanas, and D. E. Linden, "Topological filtering of dynamic functional brain networks unfolds informative chronnectomics: A novel data-driven thresholding scheme based on orthogonal minimal spanning trees (OMSTs)," *Front. Neuroinform.*, vol. 11, p. 238952, Apr. 2017, doi: 10.3389/FNINF.2017.00028/BIBTEX.

[176] T. Arichi, S. J. Counsell, A. G. Allievi, A. T. Chew, M. Martinez-Biarge, V. Mondi, N. Tusor, N. Merchant, E. Burdet, F. M. Cowan, and A. D. Edwards, "The effects of hemorrhagic parenchymal infarction on the establishment of sensori-motor structural and functional connectivity in early infancy," *Neuroradiology*, vol. 56, no. 11, pp. 985–994, Nov. 2014, doi: 10.1007/S00234-014-1412-5/FIGURES/5.

[177] C. Herzmann, L. Zubiaurre-Elorza, C. J. Wild, A. C. Linke, V. K. Han, D. S. C. Lee, and R. Cusack, "Using Functional Magnetic Resonance Imaging to Detect Preserved

Function in a Preterm Infant with Brain Injury," *J. Pediatr.*, vol. 189, pp. 213-217.e1, Oct. 2017, doi: 10.1016/J.JPEDS.2017.06.063.

[178] P. Fransson, B. Skiöld, M. Engström, B. Hallberg, M. Mosskin, U. Åden, H. Lagercrantz, and M. Blennow, "Spontaneous brain activity in the newborn brain during natural sleep-an fMRI study in infants born at full term," *Pediatr. Res.*, vol. 66, no. 3, pp. 301–305, Sep. 2009, doi: 10.1203/PDR.0b013e3181b1bd84.

[179] M. Eyre, S. P. Fitzgibbon, J. Ciarrusta, L. Cordero-Grande, A. N. Price, T. Poppe, A. Schuh, E. Hughes, C. O'Keeffe, J. Brandon, D. Cromb, K. Vecchiato, J. Andersson, E. P. Duff, S. J. Counsell, S. M. Smith, D. Rueckert, J. V Hajnal, T. Arichi, J. O'Muircheartaigh, D. Batalle, and A. D. Edwards, "The Developing Human Connectome Project: Typical and disrupted perinatal functional connectivity," *Brain*, vol. 144, no. 7, pp. 2199–2213, 2021, doi: 10.1093/brain/awab118.

[180] A. Guzzetta, S. Fiori, D. Scelfo, E. Conti, and A. Bancale, "Reorganization of visual fields after periventricular haemorrhagic infarction: Potentials and limitations," *Dev. Med. Child Neurol.*, vol. 55, no. SUPPL.4, pp. 23–26, Nov. 2013, doi: 10.1111/dmcn.12302.

[181] M. Mahmoudzadeh, G. Dehaene-Lambertz, G. Kongolo, M. Fournier, S. Goudjil, and F. Wallois, "Consequence of intraventricular hemorrhage on neurovascular coupling evoked by speech syllables in preterm neonates," *Dev. Cogn. Neurosci.*, vol. 30, pp. 60–69, Apr. 2018, doi: 10.1016/j.dcn.2018.01.001.

[182] S. Hayasaka and P. J. Laurienti, "Comparison of characteristics between region-and voxel-based network analyses in resting-state fMRI data," *Neuroimage*, vol. 50, no. 2, pp. 499–508, 2010, doi: 10.1016/j.neuroimage.2009.12.051.

[183] O. Korhonen, H. Saarimäki, E. Glerean, M. Sams, and J. Saramäki, "Consistency of Regions of Interest as nodes of fMRI functional brain networks," *Netw. Neurosci.*, vol. 1, no. 3, pp. 254–274, Oct. 2017, doi: 10.1162/netn_a_00013.

[184] M. E. Barnes-Davis, S. L. Merhar, S. K. Holland, N. A. Parikh, and D. S. Kadis, "Extremely preterm children demonstrate hyperconnectivity during verb generation: A multimodal approach," *NeuroImage Clin.*, vol. 30, Jan. 2021, doi: 10.1016/j.nicl.2021.102589.

[185] M. E. Barnes-Davis, B. J. Williamson, J. E. Kline, B. M. Kline-Fath, J. Tkach, L. He, W. Yuan, and N. A. Parikh, "Structural connectivity at term equivalent age and language in preterm children at 2 years corrected," *Brain Commun.*, vol. 6, no. 2, 2024, doi: 10.1093/braincomms/fcae126.

[186] A. Parodi, P. Govaert, S. Horsch, M. C. Bravo, L. A. Ramenghi, T. Agut, A. Alarcon, R. Arena, M. Bartocci, M. Bravo, F. Cabañas, N. Carreras, O. Claris, J. Dudink, M. Fumagalli, P. Govaert, S. Horsch, A. Parodi, A. Pellicer, L. A. Ramenghi, C. C. Roehr, S. Steggerda, and E. Valverde, "Cranial ultrasound findings in preterm germinal matrix haemorrhage, sequelae and outcome," *Pediatric Research*, vol. 87. Springer Nature, pp. 13–24, Mar. 01, 2020. doi: 10.1038/s41390-020-0780-2.

[187] S. E. Jacobs, M. Berg, R. Hunt, W. O. Tarnow-Mordi, T. E. Inder, and P. G. Davis, “Cooling for newborns with hypoxic ischaemic encephalopathy,” *Cochrane Database Syst. Rev.*, vol. 2013, no. 1, Jan. 2013, doi: 10.1002/14651858.CD003311.PUB3.

[188] S. Mitra, G. Bale, J. Meek, I. Tachtsidis, and N. J. Robertson, “Cerebral near infrared spectroscopy monitoring in term infants with hypoxic ischemic encephalopathy—a systematic review,” *Front. Neurol.*, vol. 11, pp. 1–17, Jan. 2020, doi: 10.3389/FNEUR.2020.00393/BIBTEX.

[189] S. Peng, E. Boudes, X. Tan, C. Saint-Martin, M. Shevell, and P. Wintermark, “Does Near-Infrared Spectroscopy Identify Asphyxiated Newborns at Risk of Developing Brain Injury during Hypothermia Treatment?,” *Am. J. Perinatol.*, vol. 32, no. 6, pp. 555–563, May 2015, doi: 10.1055/S-0034-1396692/ID/JR140192-35.

[190] S. V. Jain, L. Pagano, M. Gillam-Krakauer, J. C. Slaughter, S. Pruthi, and B. Engelhardt, “Cerebral regional oxygen saturation trends in infants with hypoxic-ischemic encephalopathy,” *Early Hum. Dev.*, vol. 113, pp. 55–61, Oct. 2017, doi: 10.1016/j.earlhumdev.2017.07.008.

[191] C. D. Smyser, A. Z. Snyder, and J. J. Neil, “Functional Connectivity MRI in Infants: Exploration of the Functional Organization of the Developing Brain,” *Neuroimage*, vol. 56, no. 3, p. 1437, Jun. 2011, doi: 10.1016/J.NEUROIMAGE.2011.02.073.

[192] J. Uchitel, B. Blanco, L. Collins-Jones, E. Porter, A. Edwards, K. Pammenter, R. J. Cooper, and T. Austin, “Imaging Functional Brain Connectivity in the Newborn Infant using High Density Diffuse Optical Tomography,” in *Optics InfoBase Conference Papers*, Apr. 2022, p. BM2C.6. Accessed: Jan. 07, 2024. [Online]. Available: https://opg.optica.org/abstract.cfm?uri=BRAIN-2022-BM2C.6

[193] A. M. Chiarelli, C. Sestieri, R. Navarra, R. G. Wise, and M. Caulo, “Distinct effects of prematurity on MRI metrics of brain functional connectivity, activity, and structure: Univariate and multivariate analyses,” *Hum. Brain Mapp.*, vol. 42, no. 11, p. 3593, Aug. 2021, doi: 10.1002/HBM.25456.

[194] J. D. Lee, H.-J. Park, E. S. Park, M.-K. Oh, B. Park, D.-W. Rha, S.-R. Cho, E. Y. Kim, J. Y. Park, C. H. Kim, D. G. Kim, and C. Il Park, “Motor pathway injury in patients with periventricular leucomalacia and spastic diplegia,” *Brain.*, vol. 134, pp. 1199–1210, 2011, doi: 10.1093/brain/awr021.

[195] M. Ferrari and V. Quaresima, “A brief review on the history of human functional near-infrared spectroscopy (fNIRS) development and fields of application,” *Neuroimage*, vol. 63, no. 2, pp. 921–935, Nov. 2012, doi: 10.1016/j.neuroimage.2012.03.049.

[196] A. E. Lyall, F. Shi, X. Geng, S. Woolson, G. Li, L. Wang, R. M. Hamer, D. Shen, and J. H. Gilmore, “Dynamic Development of Regional Cortical Thickness and Surface Area in Early Childhood,” *Cereb. Cortex*, vol. 25, no. 8, pp. 2204–2212, Aug. 2015, doi: 10.1093/CERCOR/BHU027.

[197] V. Quaresima, S. Bisconti, and M. Ferrari, “A brief review on the use of functional near-infrared spectroscopy (fNIRS) for language imaging studies in human

newborns and adults," *Brain Lang.*, vol. 121, no. 2, pp. 79–89, May 2012, doi: 10.1016/j.bandl.2011.03.009.

[198] M. Imai, H. Watanabe, K. Yasui, Y. Kimura, Y. Shitara, S. Tsuchida, N. Takahashi, and G. Taga, "Functional connectivity of the cortex of term and preterm infants and infants with Down's syndrome," *Neuroimage*, vol. 85, pp. 272–278, Jan. 2014, doi: 10.1016/J.NEUROIMAGE.2013.04.080.

[199] L. Zöllei, J. E. Iglesias, Y. Ou, P. E. Grant, and B. Fischl, "Infant FreeSurfer: An automated segmentation and surface extraction pipeline for T1-weighted neuroimaging data of infants 0–2 years," *Neuroimage*, vol. 218, Sep. 2020, doi: 10.1016/j.neuroimage.2020.116946.

[200] K. De Macedo Rodrigues, E. Ben-Avi, D. D. Sliva, M. S. Choe, M. Drottar, R. Wang, B. Fischl, P. E. Grant, and L. Zöllei, "A freesurfer-compliant consistent manual segmentation of infant brains spanning the 0–2 year age range," *Front. Hum. Neurosci.*, vol. 9, no. FEB, Feb. 2015, doi: 10.3389/fnhum.2015.00021.

[201] J. E. Iglesias and M. R. Sabuncu, "Multi-atlas segmentation of biomedical images: A survey," *Med. Image Anal.*, vol. 24, no. 1, pp. 205–219, Aug. 2015, doi: 10.1016/j.media.2015.06.012.

[202] L. S. De Vries, P. Eken, and L. M. S. Dubowitz, "The spectrum of leukomalacia using cranial ultrasound," *Behav Brain Res.*, vol. 49, no. 1, pp. 1–6, 1992.

[203] T. J. Huppert, S. G. Diamond, M. A. Franceschini, and D. A. Boas, "HomER: A review of time-series analysis methods for near-infrared spectroscopy of the brain," *Appl. Opt.*, vol. 48, no. 10, 2009, doi: 10.1364/AO.48.00D280.

[204] L. Danon, A. Díaz-Guilera, J. Duch, and A. Arenas, "Comparing community structure identification," *J. Stat. Mech. Theory Exp.*, vol. 2005, no. 09, p. P09008, Sep. 2005, doi: 10.1088/1742-5468/2005/09/P09008.

[205] A. R. Anwar, M. Muthalib, S. Perrey, A. Galka, O. Granert, S. Wolff, U. Heute, G. Deuschl, J. Raethjen, and M. Muthuraman, "Effective Connectivity of Cortical Sensorimotor Networks During Finger Movement Tasks: A Simultaneous fNIRS, fMRI, EEG Study," *Brain Topogr.*, vol. 29, no. 5, pp. 645–660, Jul. 2016, doi: 10.1007/S10548-016-0507-1.

[206] W. Lin, Q. Zhu, W. Gao, Y. Chen, C. H. Toh, M. Styner, G. Gerig, J. K. Smith, B. Biswal, and J. H. Gilmore, "Functional connectivity MR imaging reveals cortical functional connectivity in the developing brain," *Am. J. Neuroradiol.*, vol. 29, no. 10, pp. 1883–1889, Nov. 2008, doi: 10.3174/ajnr.A1256.

[207] W. Lee, B. R. Morgan, M. M. Shroff, J. G. Sled, and M. J. Taylor, "The development of regional functional connectivity in preterm infants into early childhood," *Neuroradiology*, vol. 55, no. SUPPL. 2, pp. 105–111, Jul. 2013, doi: 10.1007/S00234-013-1232-Z/FIGURES/3.

[208] W. Majeed, M. Magnuson, W. Hasenkamp, H. Schwarb, E. H. Schumacher, L. Barsalou, and S. D. Keilholz, "Spatiotemporal dynamics of low frequency BOLD fluctuations in rats and humans," *Neuroimage*, vol. 54, no. 2, pp. 1140–1150, Jan. 2011, doi: 10.1016/J.NEUROIMAGE.2010.08.030.

[209] J. Kang, L. Wang, C. Yan, J. Wang, X. Liang, and Y. He, “Characterizing dynamic functional connectivity in the resting brain using variable parameter regression and Kalman filtering approaches,” *Neuroimage*, vol. 56, no. 3, pp. 1222–1234, Jun. 2011, doi: 10.1016/J.NEUROIMAGE.2011.03.033.

[210] O. Sporns, D. R. Chialvo, M. Kaiser, and C. C. Hilgetag, “Organization, development and function of complex brain networks,” *Trends in Cognitive Sciences*, vol. 8, no. 9. pp. 418–425, Sep. 2004. doi: 10.1016/j.tics.2004.07.008.

[211] E. Gozdas, N. A. Parikh, S. L. Merhar, J. A. Tkach, L. He, and S. K. Holland, “Altered Functional Network Connectivity in Preterm Infants: Antecedents of Cognitive and Motor Impairments?,” *Brain Struct. Funct.*, vol. 223, no. 8, p. 3665, Nov. 2018, doi: 10.1007/S00429-018-1707-0.

[212] P. J. Brittain, S. Froudist Walsh, K. W. Nam, V. Giampietro, V. Karolis, R. M. Murray, S. Bhattacharyya, A. Kalpakidou, and C. Nosarti, “Neural compensation in adulthood following very preterm birth demonstrated during a visual paired associates learning task,” *NeuroImage Clin.*, vol. 6, pp. 54–63, 2014, doi: 10.1016/j.nicl.2014.08.009.

[213] Q. Behfar, S. K. Behfar, B. von Reutern, N. Richter, J. Dronse, R. Fassbender, G. R. Fink, and O. A. Onur, “Graph theory analysis reveals resting-state compensatory mechanisms in healthy aging and prodromal Alzheimer’s disease,” *Front. Aging Neurosci.*, vol. 12, pp. 1–13, Oct. 2020, doi: 10.3389/FNAGI.2020.576627/BIBTEX.

[214] C. M. Kelsey, K. Farris, and T. Grossmann, “Variability in Infants’ Functional Brain Network Connectivity Is Associated With Differences in Affect and Behavior,” *Front. Psychiatry*, vol. 12, Jun. 2021, doi: 10.3389/fpsyt.2021.685754.

[215] E. Piccirilli, A. M. Chiarelli, C. Sestieri, D. Mascali, D. Calvo Garcia, A. Primavera, R. Salomone, R. G. Wise, A. Ferretti, and M. Caulo, “Cerebral blood flow patterns in preterm and term neonates assessed with pseudo-continuous arterial spin labeling perfusion MRI,” *Hum. Brain Mapp.*, vol. 44, no. 9, pp. 3833–3844, Jun. 2023, doi: 10.1002/hbm.26315.

[216] A. N. Massaro, R. B. Govindan, G. Vezina, T. Chang, N. N. Andescavage, Y. Wang, T. Al-Shargabi, M. Metzler, K. Harris, and A. J. du Plessis, “Impaired cerebral autoregulation and brain injury in newborns with hypoxic-ischemic encephalopathy treated with hypothermia,” *J. Neurophysiol.*, vol. 114, no. 2, pp. 818–824, Aug. 2015, doi: 10.1152/JN.00353.2015/ASSET/IMAGES/LARGE/Z9K0131532000002.JPEG.

[217] S. E. Jacobs, C. J. Morley, T. E. Inder, M. J. Stewart, K. R. Smith, P. J. McNamara, I. M. R. Wright, H. M. Kirpalani, B. A. Darlow, and L. W. Doyle, “Whole-Body Hypothermia for Term and Near-Term Newborns With Hypoxic-Ischemic Encephalopathy: A Randomized Controlled Trial,” *Arch. Pediatr. Adolesc. Med.*, vol. 165, no. 8, pp. 692–700, Aug. 2011, doi: 10.1001/ARCHPEDIATRICS.2011.43.

[218] D. V. Azzopardi, B. Strohm, A. D. Edwards, L. Dyet, H. L. Halliday, E. Juszczak, O. Kapellou, M. Levene, N. Marlow, E. Porter, M. Thoresen, A. Whitelaw, and P.

Brocklehurst, “Moderate Hypothermia to Treat Perinatal Asphyxial Encephalopathy,” *N. Engl. J. Med.*, vol. 361, no. 14, pp. 1349–1358, Oct. 2009, doi: 10.1056/NEJMOA0900854/SUPPL_FILE/NEJM_AZZOPARDI_1349SA1.PDF.

[219] S. Fourdain, S. Provost, J. Tremblay, P. Vannasing, A. Doussau, L. Caron-Desrochers, I. Gaudet, K. Roger, A. Hüsser, M. Dehaes, E. Martinez-Montes, N. Poirier, and A. Gallagher, “Functional brain connectivity after corrective cardiac surgery for critical congenital heart disease: a preliminary near-infrared spectroscopy (NIRS) report,” *Child Neuropsychol.*, vol. 29, no. 7, pp. 1088–1108, Oct. 2023, doi: 10.1080/09297049.2023.2170340.

[220] A. Kassab, D. Hinnoutondji Toffa, M. Robert, F. Lesage, K. Peng, and D. Khoa Nguyen, “Hemodynamic changes associated with common EEG patterns in critically ill patients: Pilot results from continuous EEG-fNIRS study,” *Neuroimage (Amst).*, vol. 32, p. 102880, Jan. 2021, doi: 10.1016/J.NICL.2021.102880.

[221] S. Sherman and R. Guillery, *Exploring the thalamus*. 2001. Accessed: Nov. 28, 2021. [Online]. Available: https://books.google.ca/books?hl=en&lr=&id=L7WAeCvWJ04C&oi=fnd&pg=PP1&dq=Sherman,+S.+Murray%3B+Guillery,+R.+W.+(2000).+Exploring+the+Thalamus.+Academic&ots=TfGdM4TU_n&sig=4ct3kdKlJJaS1HeckxrpGT9GXR8

[222] M. A. Sommer, “The role of the thalamus in motor control,” *Current Opinion in Neurobiology*, vol. 13, no. 6. Elsevier Ltd, pp. 663–670, 2003. doi: 10.1016/j.conb.2003.10.014.

[223] S. I. Cunningham, D. Tomasi, and N. D. Volkow, “Structural and functional connectivity of the precuneus and thalamus to the default mode network,” *Hum. Brain Mapp.*, vol. 38, no. 2, pp. 938–956, Feb. 2017, doi: 10.1002/hbm.23429.

[224] E. G. Duerden, R. E. Grunau, V. Chau, F. Groenendaal, T. Guo, M. M. Chakravarty, M. Benders, N. Wagenaar, R. Eijsermans, C. Koopman, A. Synnes, L. De Vries, and S. P. Miller, “Association of early skin breaks and neonatal thalamic maturation: A modifiable risk?,” *Neurology*, vol. 95, no. 24, pp. E3420–E3427, Dec. 2020, doi: 10.1212/WNL.0000000000010953.

[225] E. G. Duerden, R. E. Grunau, T. Guo, J. Foong, A. Pearson, S. Au-Young, R. Lavoie, M. M. Chakravarty, V. Chau, A. Synnes, and S. P. Miller, “Early Procedural Pain Is Associated with Regionally-Specific Alterations in Thalamic Development in Preterm Neonates,” *J. Neurosci.*, vol. 38, no. 4, pp. 878–886, Jan. 2018, doi: 10.1523/JNEUROSCI.0867-17.2017.

[226] D. M. Little, M. F. Kraus, J. Joseph, E. K. Geary, T. Susmaras, X. J. Zhou, N. Pliskin, and P. B. Gorelick, “Thalamic integrity underlies executive dysfunction in traumatic brain injury,” *Neurology*, vol. 74, no. 7, pp. 558–564, Feb. 2010, doi: 10.1212/WNL.0B013E3181CFF5D5/ASSET/3B813B7A-254B-4777-B7E5-46D64D514EC1/ASSETS/GRAPHIC/PAP.JPEG.

[227] T. J. A. Glass, V. Chau, R. E. Grunau, A. Synnes, T. Guo, E. G. Duerden, J. Foong, K. J. Poskitt, and S. P. Miller, “Multiple Postnatal Infections in Newborns Born Preterm Predict Delayed Maturation of Motor Pathways at Term-Equivalent Age with Poorer Motor Outcomes at 3 Years,” *J. Pediatr.*, vol. 196, pp. 91-97.e1, May

2018, doi: 10.1016/j.jpeds.2017.12.041.

[228] N. Liu, X. Cui, D. M. Bryant, G. H. Glover, and A. L. Reiss, “Inferring deep-brain activity from cortical activity using functional near-infrared spectroscopy,” *Biomed. Opt. Express*, vol. 6, no. 3, p. 1074, 2015, doi: 10.1364/boe.6.001074.

[229] T. N. Kipf and M. Welling, “Semi-supervised classification with graph convolutional networks,” in *5th International Conference on Learning Representations*, Sep. 2017. Accessed: Dec. 08, 2023. [Online]. Available: https://arxiv.org/abs/1609.02907v4

[230] K. Zhao, B. Duka, H. Xie, D. J. Oathes, V. Calhoun, and Y. Zhang, “A dynamic graph convolutional neural network framework reveals new insights into connectome dysfunctions in ADHD,” *Neuroimage*, vol. 246, p. 118774, Feb. 2022, doi: 10.1016/J.NEUROIMAGE.2021.118774.

[231] Y. Li, X. Zhang, J. Nie, G. Zhang, R. Fang, X. Xu, Z. Wu, D. Hu, L. Wang, H. Zhang, W. Lin, and G. Li, “Brain Connectivity Based Graph Convolutional Networks and Its Application to Infant Age Prediction,” *IEEE Trans. Med. Imaging*, vol. 41, no. 10, pp. 2764–2776, Oct. 2022, doi: 10.1109/TMI.2022.3171778.

[232] H. Zhang, L. Xu, J. Yu, J. Li, and J. Wang, “Identification of autism spectrum disorder based on functional near-infrared spectroscopy using adaptive spatiotemporal graph convolution network,” *Front. Neurosci.*, vol. 17, p. 1132231, Mar. 2023, doi: 10.3389/FNINS.2023.1132231/BIBTEX.

[233] R. C. Knickmeyer, S. Gouttard, C. Kang, D. Evans, K. Wilber, J. K. Smith, R. M. Hamer, W. Lin, G. Gerig, and J. H. Gilmore, “A structural MRI study of human brain development from birth to 2 years,” *J. Neurosci.*, vol. 28, no. 47, pp. 12176–12182, Nov. 2008, doi: 10.1523/JNEUROSCI.3479-08.2008.

[234] P. Fransson, B. Skiöld, S. Horsch, A. Nordell, M. Blennow, H. Lagercrantz, and U. Åden, “Resting-state networks in the infant brain,” *PNAS*, vol. 104, no. 39, pp. 15531–15536, 2007, doi: 10.1073/pnas.0704380104.

[235] F. Homae, H. Watanabe, T. Otobe, T. Nakano, T. Go, Y. Konishi, and G. Taga, “Development of Global Cortical Networks in Early Infancy,” *J. Neurosci.*, vol. 30, no. 14, pp. 4877–4882, Apr. 2010, doi: 10.1523/JNEUROSCI.5618-09.2010.

[236] K. P. Wylie, D. C. Rojas, R. G. Ross, S. K. Hunter, K. Maharajh, M. A. Cornier, and J. R. Tregellas, “Reduced brain resting-state network specificity in infants compared with adults,” *Neuropsychiatr. Dis. Treat.*, vol. 10, pp. 1349–1359, Jul. 2014, doi: 10.2147/NDT.S63773.

[237] P. Fransson, U. Åden, M. Blennow, and H. Lagercrantz, “The functional architecture of the infant brain as revealed by resting-state fMRI,” *Cereb. Cortex*, vol. 21, no. 1, pp. 145–154, Jan. 2011, doi: 10.1093/cercor/bhq071.

[238] M. Seeck, L. Koessler, T. Bast, F. Leijten, C. Michel, C. Baumgartner, B. He, and S. Beniczky, “The standardized EEG electrode array of the IFCN,” *Clinical Neurophysiology*, vol. 128, no. 10. Elsevier Ireland Ltd, pp. 2070–2077, Oct. 01, 2017. doi: 10.1016/j.clinph.2017.06.254.

[239] J. A. Frazier, S. Chiu, J. L. Breeze, N. Makris, N. Lange, D. N. Kennedy, M. R. Herbert, E. K. Bent, V. K. Koneru, M. E. Dieterich, S. M. Hodge, S. L. Rauch, P. E. Grant, B. M. Cohen, L. J. Seidman, V. S. Caviness, and J. Biederman, "Structural brain magnetic resonance imaging of limbic and thalamic volumes in pediatric bipolar disorder," *Am. J. Psychiatry*, vol. 162, no. 7, pp. 1256–1265, 2005, doi: 10.1176/appi.ajp.162.7.1256.

[240] V. Jurcak, D. Tsuzuki, and I. Dan, "10/20, 10/10, and 10/5 systems revisited: Their validity as relative head-surface-based positioning systems," *Neuroimage*, vol. 34, no. 4, pp. 1600–1611, 2007, doi: 10.1016/j.neuroimage.2006.09.024.

[241] F. Wang, X. Lei, B. Liao, and F. X. Wu, "Predicting drug–drug interactions by graph convolutional network with multi-kernel," *Brief. Bioinform.*, vol. 23, no. 1, 2022, doi: 10.1093/bib/bbab511.

[242] E. W. Lang, A. M. Tomé, I. R. Keck, J. M. Górriz-Sáez, and C. G. Puntonet, "Brain connectivity analysis: A short survey," *Computational Intelligence and Neuroscience*, vol. 2012. 2012. doi: 10.1155/2012/412512.

[243] L. D. Lord, P. Expert, J. F. Huckins, and F. E. Turkheimer, "Cerebral energy metabolism and the brain's functional network architecture: An integrative review," *J. Cereb. Blood Flow Metab.*, vol. 33, no. 9, pp. 1347–1354, Sep. 2013, doi: 10.1038/jcbfm.2013.94.

[244] K. T. Kinder, H. L. R. Heim, J. Parker, K. Lowery, A. McCraw, R. N. Eddings, J. Defenderfer, J. Sullivan, and A. T. Buss, "Systematic review of fNIRS studies reveals inconsistent chromophore data reporting practices," *Neurophotonics*, vol. 9, no. 04, Dec. 2022, doi: 10.1117/1.nph.9.4.040601.

[245] I. de Roever, G. Bale, S. Mitra, J. Meek, N. J. Robertson, and I. Tachtsidis, "Investigation of the pattern of the hemodynamic response as measured by functional near-infrared spectroscopy (fNIRS) studies in newborns, less than a month old: A systematic review," *Front. Hum. Neurosci.*, vol. 12, 2018, doi: 10.3389/fnhum.2018.00371.

[246] R. M. Birn, E. K. Molloy, R. Patriat, T. Parker, T. B. Meier, G. R. Kirk, V. A. Nair, M. E. Meyerand, and V. Prabhakaran, "The effect of scan length on the reliability of resting-state fMRI connectivity estimates," *Neuroimage*, vol. 83, pp. 550–558, Dec. 2013, doi: 10.1016/j.neuroimage.2013.05.099.

[247] B. Basiri, M. K. Sabzehei, M. Shokouhi Solgi, E. Khanlarzadeh, and M. Mosheiri, "The frequency of intraventricular hemorrhage and its risk factors in premature neonates in a hospital's nicu," *Iran. J. Child Neurol.*, vol. 15, no. 3, pp. 109–118, 2021, doi: 10.22037/ijcn.v15i3.21592.

[248] F. Irani, S. M. Platek, S. Bunce, A. C. Ruocco, and D. Chute, "Functional Near Infrared Spectroscopy (fNIRS): An Emerging Neuroimaging Technology with Important Applications for the Study of Brain Disorders," *Clin. Neuropsychol.*, vol. 21, no. 1, pp. 9–37, Jan. 2007, doi: 10.1080/13854040600910018.

[249] V. Y. Chock, S. H. Kwon, N. Ambalavanan, B. Batton, L. D. Nelin, L. F. Chalak, L. Tian, and K. P. Van Meurs, "Cerebral Oxygenation and Autoregulation in

Preterm Infants (Early NIRS Study)," *J. Pediatr.*, vol. 227, pp. 94-100.e1, Dec. 2020, doi: 10.1016/j.jpeds.2020.08.036.

[250] M. Lajtos, L. A. Barradas-Chacón, and S. C. Wriessnegger, "Effects of handedness on brain oscillatory activity during imagery and execution of upper limb movements," *Front. Psychol.*, vol. 14, 2023, doi: 10.3389/fpsyg.2023.1161613.

[251] R. M. Hutchison, T. Womelsdorf, E. A. Allen, P. A. Bandettini, V. D. Calhoun, M. Corbetta, S. Della Penna, J. H. Duyn, G. H. Glover, J. Gonzalez-Castillo, D. A. Handwerker, S. Keilholz, V. Kiviniemi, D. A. Leopold, F. de Pasquale, O. Sporns, M. Walter, and C. Chang, "Dynamic functional connectivity: Promise, issues, and interpretations," *Neuroimage*, vol. 80, pp. 360–378, Oct. 2013, doi: 10.1016/j.neuroimage.2013.05.079.

[252] L. G. S. França, J. Ciarrusta, O. Gale-Grant, S. Fenn-Moltu, S. Fitzgibbon, A. Chew, S. Falconer, R. Dimitrova, L. Cordero-Grande, A. N. Price, E. Hughes, J. O'Muircheartaigh, E. Duff, J. J. Tuulari, G. Deco, S. J. Counsell, J. V. Hajnal, C. Nosarti, T. Arichi, A. D. Edwards, G. McAlonan, and D. Batalle, "Neonatal brain dynamic functional connectivity in term and preterm infants and its association with early childhood neurodevelopment," *Nat. Commun.*, vol. 15, no. 1, p. 16, Feb. 2024, doi: 10.1038/s41467-023-44050-z.

[253] X. Wen, R. Wang, W. Yin, W. Lin, H. Zhang, and D. Shen, "Development of Dynamic Functional Architecture during Early Infancy," *Cereb. Cortex*, vol. 30, no. 11, pp. 5626–5638, Nov. 2020, doi: 10.1093/cercor/bhaa128.

[254] Z. Li, H. Liu, X. Liao, J. Xu, W. Liu, F. Tian, Y. He, and H. Niu, "Dynamic functional connectivity revealed by resting-state functional near-infrared spectroscopy," *Biomed. Opt. Express*, vol. 6, no. 7, p. 2337, Jul. 2015, doi: 10.1364/boe.6.002337.

[255] A. Vaswani, G. Brain, N. Shazeer, N. Parmar, J. Uszkoreit, L. Jones, A. N. Gomez, Ł. Kaiser, and I. Polosukhin, "Attention is All you Need," *Adv. Neural Inf. Process. Syst.*, vol. 30, 2017.

[256] C. Huang, W. Chen, B. Liu, R. Yu, X. Chen, F. Tang, J. Liu, and W. Lu, "Transformer-Based Deep-Learning Algorithm for Discriminating Demyelinating Diseases of the Central Nervous System With Neuroimaging," *Front. Immunol.*, vol. 13, p. 897959, Jun. 2022, doi: 10.3389/FIMMU.2022.897959/BIBTEX.

[257] U. Mahmood, Z. Fu, V. Calhoun, and S. Plis, "Glacier: Glass-Box Transformer for Interpretable Dynamic Neuroimaging," in *ICASSP, IEEE International Conference on Acoustics, Speech and Signal Processing - Proceedings*, Institute of Electrical and Electronics Engineers Inc., 2023. doi: 10.1109/ICASSP49357.2023.10097126.

[258] A. W. Thomas, C. Ré, and R. A. Poldrack, "Self-Supervised Learning of Brain Dynamics from Broad Neuroimaging Data," *Adv. Neural Inf. Process. Syst.*, vol. 35, pp. 21255–21269, Dec. 2022.

[259] D. Karimi and A. Gholipour, "Diffusion tensor estimation with transformer neural networks," *Artif. Intell. Med.*, vol. 130, Aug. 2022, doi: 10.1016/j.artmed.2022.102330.

[260] S. Yun, M. Jeong, R. Kim, J. Kang, and H. J. Kim, “Graph Transformer Networks,” *Adv. Neural Inf. Process. Syst.*, vol. 32, 2019.

Curriculum Vitae

Name: Lingkai Tang

Post-secondary Education and Degrees:

Northwestern Polytechnical University
Xi'an, Shaanxi, China
2011-2015 B.Eng.

University of Saskatchewan
Saskatoon, Saskatchewan, Canada
2015-2019 M.Sc.

Western University
London, Ontario, Canada
2019-current Ph.D.

Honours and Awards:

Saskatchewan innovation and opportunity scholarship
2016-2017

Related Work Experience

Teaching Assistant
University of Saskatchewan
2015-2018

Teaching Assistant
Western University
2020-2022

Publications:

Wu, L., **Tang, L.**, Li, M., Wang, J., & Wu, F. X. (2016, December). The MSS of complex networks with centrality based preference and its application to biomolecular networks. In *2016 IEEE International Conference on Bioinformatics and Biomedicine (BIBM)* (pp. 229-234). IEEE.

Wu, L., **Tang, L.**, Li, M., Wang, J., & Wu, F. X. (2017). Biomolecular network controllability with drug binding information. *IEEE transactions on nanobioscience*, *16*(5), 326-332.

Tang, L. (2019). Diagnosis of autism spectrum disorder based on brain network clustering (Master dissertation, University of Saskatchewan).

Mostafa, S., **Tang, L.**, & Wu, F. X. (2019). Diagnosis of autism spectrum disorder based on eigenvalues of brain networks. Ieee Access, 7, 128474-128486.

Zhang, J., **Tang, L.**, Liao, B., Zhu, X., & Wu, F. X. (2019). Finding community modules of brain networks based on PSO with uniform design. *BioMed Research International*, *2019*.

Tang, L., Mostafa, S., Liao, B., & Wu, F. X. (2019). A network clustering based feature selection strategy for classifying autism spectrum disorder. *BMC medical genomics*, *12*, 1-10.

Ali, S., Altamimi, T., Annink, K., Bartmann, P., Beato, N., Belker, K., ... & Yapicioglu-Yildizdas, H. (2023). Proceedings of the 14th International Newborn Brain Conference: Other forms of brain monitoring, such as NIRS, fMRI, biochemical, etc. *Journal of neonatal-perinatal medicine*, *16*(s1), S63-S73.

Kebaya, L. M., **Tang, L.**, Altamimi, T., Kowalczyk, A., Musabi, M., Roychaudhuri, S., ... & Duerden, E. G. (2024). Functional connectivity in preterm infants with intraventricular hemorrhage using fNIRS. *medRxiv*, 2024-02.

Tang, L., Kebaya, L., Vahidi, H., Meyerink, P., de Ribaupierre, S., Bhattacharya, S., ... & Duerden, E. (2024). Predicting cortical-thalamic connectivity using functional near-infrared spectroscopy and graph convolutional networks.

Tang, L., Kebaya, L. M., Altamimi, T., Kowalczyk, A., Musabi, M., Roychaudhuri, S., ... & Duerden, E. G. (2024). Altered resting-state functional connectivity in newborns with hypoxic ischemic encephalopathy assessed using high-density functional near-infrared spectroscopy. *Scientific Reports*, *14*(1), 3176.

Conference Presentations:

Posters

Artificial Neural Networks to Predict Cortical-subcortical Connectivity from Cortical fNIRS Recordings. SfNIRS, 2021.

Altered resting state functional connectivity in newborns with hypoxic ischemic encephalopathy assessed using high-density functional near-infrared spectroscopy. Pediatric Academic Societies, 2022.

Altered resting state functional connectivity in newborns with hypoxic ischemic encephalopathy assessed using high-density functional near-infrared spectroscopy. SfNIRS, 2022.

Altered functional connectivity in term newborns with neonatal abstinence syndrome revealed by resting-state functional near-infrared spectroscopy. SfNIRS, 2022.

Resting-state functional near-infrared spectroscopy reveals altered functional connectivity of neonates with hypoxic ischemic encephalopathy post cooling. International Newborn Brain Conference, 2023.

Altered resting-state functional connectivity in neonates with intraventricular hemorrhage. Society for Neuroscience, 2023.

Functional near-infrared spectroscopy reveals altered resting-state connectivity in preterm newborns with intraventricular hemorrhage. Pediatric Academic Societies, 2024.

Oral Presentation

Resting-state functional near-infrared spectroscopy reveals altered functional connectivity of neonates with hypoxic ischemic encephalopathy post cooling. Child Health Research Day Conference, 2023